APPLICATION OF LUMINESCENT MATERIALS TO OPTICAL SENSING

A Dissertation

by

SARAH CHRISTINE RITTER

Submitted to the Office of Graduate and Professional Studies of
Texas A&M University
in partial fulfillment of the requirements for the degree of

DOCTOR OF PHILOSOPHY

Chair of Committee,	Kenith E. Meissner
Committee Members,	Javier A. Jo
	Gerard L. Coté
	Cristine L. Heaps
Head of Department,	Gerard L. Coté

December 2014

Major Subject: Biomedical Engineering

ABSTRACT

Development of sensors for detection of various chemical and biological species is an important and ever-growing field. In particular, optical-based sensors enable a remote, rapid method for continuous or on-demand monitoring. Monitoring humidity is important across many applications, such as humidity control within moisture-sensitive environments and in medical, semiconductor, and food science fields. Following a study of photobleaching, defect-related emission of zinc oxide nanoparticles was monitored as a function of relative humidity. An important next step is its application to monitoring toxic gases, as air pollution has been identified as a major health concern. Of importance for the biomedical field is monitoring key blood analytes for human health. Monitoring blood pH is critical for specific patient groups, such as those suffering from diabetic ketoacidosis and congenital lactic acidosis. A pH-sensitive fluorophore was loaded within red blood cells for use as a continuous blood analyte monitor. Future work will focus on glucose, as current estimates show that one out of every three children born in 2000 will develop diabetes in his or her lifetime – thus, the global impact of this disease is immense.

Results from ZnO studies indicate that photobleaching is related to the surface area to volume ratio. ZnO nanoparticles display a linear response to humidity with a sensitivity of 0.008417 RH^{-1} and 0.01898 RH^{-1} for nitrogen and air environments, respectively. Owing to reversibility and high sensitivity, ZnO nanoparticles have great potential as optical-based environmental sensors.

Results from dye-loaded ghost studies indicate that fluorescence intensity of intracellular dyes report on extracellular pH. Resealed ghosts loaded with a fluorescein isothiocyanate-glycylglycine conjugate reversibly track pH with a resolution down to 0.014 pH unit. For use *in vivo*, the development of an NIR pH-sensitive dye was paramount. Unfortunately, all NIR dyes tested exhibited poor pH sensitivity while displaying sensitivity to external factors (*e.g.*, temperature, concentration, proteins). However, circulation kinetics of resealed ghosts were easily monitored once injected *in vivo* with an optical fiber-based system. Although the cells were rapidly removed from circulation, the loaded ghosts resulted in higher signal than would be expected for free dye alone. Once optimized, the resealed ghosts could serve as a long-term, continuous, circulating biosensor for the management of diseases.

DEDICATION

I dedicate this work to my husband, Dustin, for his unfailing love and support throughout this entire process – I could not have done it without him at my side. It is an incredible blessing to have someone who understands exactly what I am going through and who knows what to say to make things clearer. Graduate school has given us opportunities we may never have had any other way. I am so happy that we were able to spend two months experiencing Rwanda – spending time with our host families, hiking a volcano (or for me, being dragged at least some of the way), working with our new BMET friends in the hospitals, soaking in the beauty of the savannah and rainforest, and spending many hours at the local coffee shops just enjoying the moment. We made memories we'll always look back fondly on and never forget – I hope someday we make it back. Spending a week catching trains with you across Germany, Belgium, and the Netherlands was incredible – who knew we'd see so much of the world. And there is more yet to see.

TABLE OF CONTENTS

LIST OF FIGURES

LIST OF TABLES

1. INTRODUCTION

1.1 Photoluminescence

Photoluminescence is broadly defined as the emission of light following absorption of a photon and can be further categorized based on the mechanism of action.

1.1.1 Fluorescence and Phosphorescence

Fluorescence is characterized by the preservation of spin multiplicity, whereby the electron in an excited singlet state is paired to an electron with the opposite spin in the ground singlet state. Return to the ground state is therefore allowed, leading to rapid photon emission from the excited singlet state with rates typically on the order of 10^8 s^{-1}. Phosphorescence, on the other hand, is characterized by emission from an excited triplet state following intersystem crossing from an excited singlet state. Furthermore, the electrons in the excited triplet and ground singlet state possess the same spin. As a result, transitions are considered forbidden, leading to considerably slower emission rates (10^3 to 10^0 s^{-1}) [1].

Photoluminescence processes, including absorption and emission, are typically portrayed on a Jablonski diagram (named for Alexander Jablonski, the father of fluorescence spectroscopy). An example of a Jablonski diagram is shown in Figure 1. According to the Franck-Condon principle, absorption occurs instantaneously, or at least at a time scale too short for nuclear displacement, and is therefore represented by a vertical line on the diagram. The molecule is typically excited to a higher vibrational level within an excited state, S_1 or S_2, and relaxation to the lowest vibrational level

occurs through a process known as vibrational relaxation (within the same excited state) or internal conversion (relaxation to a lower excited state). Emission of a photon, then, occurs upon relaxation from the lowest vibrational level of the excited state – the thermally-equilibrated state – to the ground state. As a result, the emission spectrum of a fluorophore is not dependent upon the excitation wavelength, a principle known as Kasha's rule. Similar to absorption, emission occurs to a higher vibrational state within the ground state, S_0, which then rapidly relaxes to the lowest vibrational level. Consequently, the absorption and emission spectra of a fluorophore are typically mirror images of each other. A molecule in an excited singlet state can also go through intersystem crossing, *i.e.*, spin conversion to the excited triplet state, T_1. Emission from the excited triplet state, a forbidden process, is phosphorescence. Both fluorescence and phosphorescence emission typically occur at a longer wavelength, or lower energy, than absorption, which is observed as a displacement of the spectrum known as the Stokes shift. This shift is a result of energy loss due to vibrational relaxation in both the excited and ground states, as well as a number of other effects such as energy transfer and solvent effects [1].
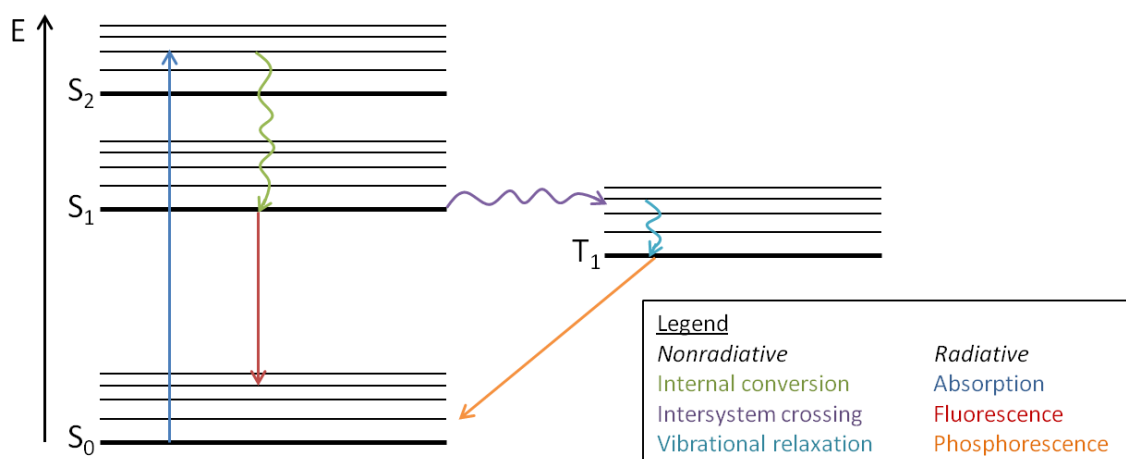
Figure 1. Example Jablonski diagram displaying various photoluminescence processes with energy on the y-axis. Bold horizontal lines represent the ground vibrational states of the ground (S_0) and excited singlet (S_1 and S_2) and triplet (T_1) electronic energy states. The thinner horizontal lines are representative of vibronic energy levels corresponding to each electronic energy level. Radiative and nonradiative processes are designated with straight and wavy lines, respectively.

1.1.2 Semiconductor Luminescence

For direct band gap semiconductors, absorption of a photon with energy higher than its band gap results in the transition of an electron from the valence to conduction band, creating an electron-hole pair. Upon recombination of an electron and hole, a photon is emitted with energy similar to that of the semiconductor's band gap energy [2]. Emission due radiative recombination, termed exciton emission, occurs in the UV region of the spectrum [3]. Defects (*e.g.*, vacancies) within the semiconductor material can efficiently trap electrons and/or holes, resulting in changes in the optical properties. Recombination of the electron and hole results in a second emission band at a lower energy, or higher wavelength, than that of the exciton emission band [4].

3

1.2 Photoluminescence-Based Sensing

Sensing is a broad field that aims to transform information from one form to another, measurable form. The International Union of Pure and Applied Chemistry (IUPAC) provides the following definition for chemical sensing [5]:

"A chemical sensor is a device that transforms chemical information, ranging from the concentration of a specific sample component to total composition analysis, into an analytically useful signal."

They further classify chemical sensors according to the operating principle, for example, an optical-based sensor, which is then subdivided into the applied optical properties (*e.g.*, fluorescence) [5]:

"Optical devices transform changes of optical phenomena, which are the result of an interaction of the analyte with the receptor part."

In the presence of the analyte, the observable change in the spectral properties (*e.g.*, intensity change or spectral shift) can be measured, allowing for optical-based analyte monitoring. Fluorescence-based sensing offers many advantages over other sensing methods including very high sensitivity to the analyte of interest as well as speed, which is typically limited by factors other than the fluorescence response. An advantage that is particularly useful in the biomedical field is that the propagation of light allows the opportunity for noninvasive, remote sensing. Fluorescence sensing can be applied to a wide range of analytes – gases, pH, proteins, *etc.* – in an endless number of environments – air, solution phase, living cells, *etc.* [6].

Sensors are typically described by a number of characteristics that together determine how well a sensor responds to a given analyte of interest. The limit of detection is the lowest measurable analyte concentration and is a function of the measurement instrumentation and sources of noise (*e.g.*, instrument noise, background fluorescence, scattering, *etc.*). The sensitivity is the slope of the calibration curve that describes the measured signal as a function of the analyte. The dynamic range describes the concentration range of the analyte that can be measured [6].

1.2.1 Wavelength-Ratiometric Measurements for Luminescence Sensing

For some analyte-sensitive dyes, the entire fluorescence band shifts as a function of analyte concentration. The shift stems from a change in the electronic transitions due to intermolecular interactions that affect the energies of the ground and excited states. In the case of a dye displaying this property, the result is an increase in intensity at one edge of the band with a concomitant decrease in the other edge. A two-channel ratiometric measurement of the intensity levels at these two points may serve as a method for monitoring analyte levels. There are a number of advantages to ratiometric sensing over traditional intensity-based sensing. First, the ratio would be dependent upon analyte concentration only, rather than on the concentration of the analyte-sensitive dye. Furthermore, photobleaching should affect the entire emission spectrum, thereby leaving the ratio unchanged and able to reliably relay the analyte concentration [6].

1.3 Unintended Sensitivity of Fluorophores to their Environment

Analyte-sensitive fluorescent dyes may also be sensitive to other, unintended aspects of their environment, such as the temperature (thermal quenching) or polarity of

the solvent (solvatochromism). Static quenching decreases with increased temperature due to disruption of the complexes responsible for quenching; conversely, dynamic quenching increases with increased temperature due to increased rate of diffusion of the quencher [6]. Dyes may exhibit either bathochromic (red) or hypsochromic (blue) shifts with increasing solvent polarity. Solvatochromism is attributed to a differential solvation between the ground and first excited states. If the molecule in the ground state is better stabilized by solvation as polarity increases than in the excited state, then the molecule will undergo negative solvatochromism (*i.e.*, hypsochromic shift). Conversely, if the molecule is better stabilized in the excited state, it will undergo positive solvatochromism (*i.e.*, bathochromic shift). In addition to shifts in the spectra of solvatochromic dyes, solvent polarity can affect the intensity of the bands [7, 8]. Some dyes are known to show sensitivity to proteins, as shown by a substantial increase in fluorescence and spectral shift upon addition of protein. This signal increase is thought to result from the dye binding within a hydrophobic pocket of the protein [1].

1.4 Outline of Dissertation

The photobleaching studies of various zinc oxide (ZnO) structures as well as the application of ZnO nanoparticles to monitoring of humidity levels in air and nitrogen are discussed in *Section 2*. *Sections 3* and *4* are devoted to the development of a red blood cell (RBC)-based sensing platform. Specifically, monitoring of extracellular pH levels *via* changes in fluorescence of an intracellular glycylglycine-fluorescein isothiocyanate (FITC) conjugate is discussed in *Section 3*. *Section 4* focuses on the development of a near-infrared (NIR) sensing system towards the application of these sensors for *in vivo*

monitoring. Finally, *Section 5* provides conclusions on the present work and an outlook

on future work that would build upon the results presented here.

2. APPLICATION OF ZINC OXIDE NANO- AND MICROSTRUCTURES TO OPTICAL HUMIDITY SENSING

2.1 Background

2.1.1 Zinc Oxide

ZnO is a II-VI semiconductor possessing a number of valuable properties such as a direct band gap of 3.37 eV at room temperature and a large exciton-binding energy of 60 meV that leads to photoluminescence at room temperature; simple and inexpensive production of nano/microstructures that lends itself to incorporation into low-cost devices; and biocompatibility that is relevant for biomedical applications [9, 10]. Combined, these characteristics make ZnO a promising material for various sensing schemes.

2.1.2 Electrical-Based Sensing with ZnO

Traditionally, sensing with metal oxides has been performed by measuring changes in electrical conductivity, resulting from an interaction between an adsorbed molecule and the metal oxide surface. ZnO has been used to monitor changes in a number of gases, including nitrogen dioxide (NO_2) [11-17], ethanol [12, 18-21], ozone [22, 23], acetone [12], and carbon monoxide (CO) [11, 24, 25], as well as for monitoring changes in the local humidity level [26]. Although there have been many promising results, conductometric-type sensors still suffer a number of disadvantages, including the requirement for electrode contacts and the need for elevated working temperatures in nearly all cases. Thus, the advantages of an optical-based scheme, such as the ability for

remote, contactless sensing at room temperature, have led to investigation into environmental sensing based on changes in ZnO luminescence.

2.1.3 ZnO Luminescence and Optical-Based Sensing

When excited in the UV, ZnO exhibits two emission bands, one in the UV – near-band edge emission stemming from excitonic emission – and a second, much broader peak in the visible region – stemming from deep-level defects within the crystal structure [9, 10]. Although the exact mechanism behind the visible emission is still under investigation, oxygen vacancies are commonly cited defects [3, 27-30]. Luminescence emission, similar to the conductivity, is sensitive to changes in the local environment of the sample. Optical-based sensing techniques have been used to study primarily NO_2 [22, 31-37], ethanol [34, 37, 38], and humidity [34, 37, 39, 40].

A more detailed discussion of the studies involving humidity is appropriate given the scope of the work presented here. Using a vapor transport technique, Baratto *et al.* prepared ZnO nanowires with widths of 300 nm and lengths of several microns and applied this material to NO_2, ethanol, and humidity sensing [37]. A quenching of 2.3% of the luminescence was observed upon exposure to 0.1 ppm NO_2 and increased to an 8% quenching in 2 ppm NO_2. Luminescence enhancements of 2.8%, 3.9%, and 4.6% were observed in response to 20%, 50%, and 70% relative humidity (RH) while enhancement of 1.5% was observed for 1000 ppm ethanol. Comini *et al.* prepared ZnO nanowires with widths ranging from 72 to 78 nm and lengths spanning several microns using a vapor transport process [34]. The nanowires exhibited a reduction in luminescence of 27% when exposed to 16 ppm NO_2. The authors also investigated the

9

effects of ethanol and humidity on the signal, observing a 4% signal reduction in response to 30% humidity and a 7% signal increase due to 900 ppm ethanol. Aneesh *et al.* employed evanescent wave absorption spectroscopy to monitor humidity levels using a decladded optical fiber that had been uniformly coated with a ZnO nanoparticle-doped film [39]. Utilizing changes in optical intensity due to absorption of the film at 632.8 nm, the sensor exhibited a linear response across a range of 4% and 96% RH with a sensitivity of 0.0012 RH^{-1}. Liu *et al.* grew ZnO nanorods with diameters ranging from 200–300 nm and a maximum length of 2.5 µm on the surface of a thinned silica fiber [40]. Optical transmission at 644 nm decreased as humidity increased over the range of 10-95% RH with a maximum sensitivity of 0.014 RH^{-1} using a nanorod-coated, 5 µm diameter optical fiber. The authors indicated that the increased sensitivity compared with larger diameter optical fibers is likely due to an increased proportion of light interacting with the external medium (*e.g.*, humidity). For luminescence-based humidity sensing, the mechanism employed in this paper, larger nanostructures have generally been the focus of the literature, but there has not been a consensus regarding humidity effects on luminescence. As a result, the effects of ZnO structure size on optical sensing properties are not well understood. Thus, there is a need to investigate optical properties across multiple size regimes to determine which ZnO structure possesses the best qualities, specifically sensitivity and range, for environmental sensing.

2.1.4 Clinical Relevance of ZnO for Monitoring NO$_2$ and CO

The proof-of-concept work presented here for ZnO nanoparticle-based monitors for local humidity levels can be extended to other environmental gases. Of particular

relevance is the application of ZnO towards NO_2 and CO monitoring. The World Health Organization has identified indoor and outdoor air pollution as a major health problem for both developed and developing countries. However, the greatest burden falls on those people living in low- and middle-income countries. NO_2, which results from combustion processes (*e.g.*, heating, engines, *etc.*), is a known contributor to outdoor air pollution. Epidemiological studies have revealed a correlation between long-term NO_2 exposure and symptoms of bronchitis in asthmatic children as well as reduced lung function growth [41]. CO, which results from inefficient burning of organic fuel, is the leading cause of poisoning in the United States [42]. In developing countries in particular, CO is a major concern as it is released upon burning wood or charcoal, common fuel sources supplying between 50% and 95% of domestic energy needs. Poor ventilation and low combustion efficiency increase the harmful health effects in these countries [43]. CO irreversibly binds to hemoglobin (Hb), which blocks the binding and transport of oxygen and can lead to death [42]. Thus, proper monitoring and control of NO_2 and CO levels, in particular with a sensing system based on ZnO owing to its low cost, are important for global health.

2.2 Materials and Methods

2.2.1 Sample Preparation

ZnO nanoparticles were prepared using a method originally reported by Haase *et al.* [44]. Briefly, hydrolysis was initialized by addition of 65 mL of 30 mM NaOH to 125 mL of 10 mM zinc acetate solution ($Zn(CH_3COO)_2 \cdot 2H_2O$, >98%, Sigma-Aldrich) in methanol with rapid stirring. The mixture was refluxed for two hours at 60 °C on a hot

plate. The prepared ZnO nanoparticles were used as seed material for subsequent generation of nanopods, which was accomplished by mixing 100 µL of ZnO nanoparticles (2.9 µM) with 2 mL of a growth solution consisting of an equimolar mixture of zinc nitrate hexahydrate ($Zn(NO_3)_2 \cdot 6H_2O$, 99%, Sigma-Aldrich) and hexamethylenetetramine (HMT, C6H12N4, 99%, Sigma-Aldrich) at 25 mM [45]. This mixture was then heated to 170 °C under 100-150 psi of pressure in a single-mode microwave (Discover® system, CEM). After being held at 170 °C for 20 min, compressed air was flowed into the microwave to cool the reaction mixture. Microrods were prepared by placing a 2 mL volume of an equimolar ratio of $Zn(NO_3)_2$ and HMT at 25 mM in a glass vessel within the single-mode microwave, as described previously [46]. Similar to the nanopods, the solution was heated to 170 °C and held for 20 min, followed by rapid cooling by flow of compressed air. All ZnO samples were cleaned with methanol and subsequently stored in methanol at 4 °C until application. For optical experiments, a small volume of ZnO solution was placed inside of a 1 cm path length quartz cuvette and placed under a steady stream of nitrogen to evaporate the methanol, leaving a film of ZnO nano/microstructures.

2.2.2 Optical System

A custom optical system was used to collect all ZnO luminescence data. A mode-locked Ti:sapphire laser (Mira 900, Coherent) at 700 nm was frequency doubled via a Type 1 BBO crystal prior to the sample stage to produce 350 nm excitation. Luminescence was collected at 90° with a CCD-coupled spectrometer (Acton SpectraPro 2300i, Princeton Instruments). Residual 700 nm laser line and 350 nm excitation were

removed by a short-pass filter (650 nm cut-off, OD 4, Edmund Optics) and long-pass

filter (395 nm cut-off, Edmund Optics), respectively. For time-course measurements, the

signal was integrated from 450 nm to 690 nm – the visible, defect-related band. Periodic

excitation schemes were accomplished by employing a software-controlled, mechanical

shutter (SH05, Thorlabs) in the beam path. Humidity levels were prepared by mixing dry

and wet gas at predetermined flow rates for the desired humidity. Humidity

measurements were performed with a modified commercial humidity monitor (20-90%

RH range; 1% RH resolution; VWR). Sensitivity (% signal change / % RH) was defined

as the slope of the regression line of the calibration curve for luminescence as a function

of RH. For comparison with other methodologies, normalized sensitivity (RH^{-1}) was

defined as the slope of the calibration curve normalized to the highest luminescence

value.

2.3 Results and Discussion

2.3.1 ZnO Characterization

The optical characteristics of three ZnO nano/microstructures, with widely

varying surface area to volume ratios, were investigated via luminescence spectroscopy.

The ZnO structures analyzed in this work consisted of (1) ZnO nanopods – multiple-

legged structures; (2) ZnO microrods – single hexagonal structures; and (3) ZnO

nanoparticles. The physical dimensions of the ZnO nanoparticles were characterized

using transmission electron microscopy (TEM) and corroborated with an effective mass

model based on the onset of UV-visible absorption. Scanning emission microscopy

(SEM) and TEM, coupled with an x-ray diffractogram, were used for characterization of

nanopods [45]. Similarly, the dimensions of the ZnO microrods were characterized using

SEM [46]. The physical dimensions of these samples are summarized in Table 1. The

samples were excited at 350 nm (1 mW, 75 mm focal length lens), and emission from

the various samples was collected at 90° with a CCD-coupled spectrometer. Sample

luminescence spectra of ZnO nanoparticles (dark blue) and microrods (light blue) are

shown in Figure 2; the 450-690 nm band integrated for time-course measurements

reflects the defect-related luminescence from the samples.

Table 1. Physical dimensions (average, $\bar{x}$, and standard deviation, σ) of ZnO samples.

Sample	Length, $\bar{x}$ (nm)	Length, σ (nm)	Dia., $\bar{x}$ (nm)	Dia., σ (nm)
Nanoparticles	-	-	4.1	0.8
Nanopods	275	25	15.44	1.89
Microrods	1450	100	380	60
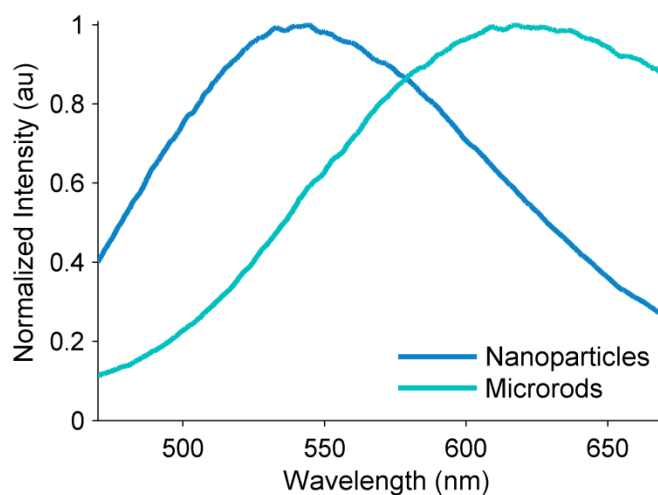
Figure 2. Luminescence spectra of ZnO nanoparticles (dark blue) and microrods (light blue). Time-course luminescence data were integrated from 450 nm to 690 nm, the defect-related band.

2.3.2 Photobleaching Studies

Upon excitation, all ZnO nano/microstructures exhibited reversible photobleaching that recovered over time in the absence of excitation. The rate and extent of recovery depended on exposure dynamics (*e.g.*, exposure and recovery times). As shown in Figure 3, ZnO nanoparticles exposed to a 1 sec excitation every 10 sec exhibited signal recovery following a 20 min period of recovery time. After 5.5 min of excitation, the signal dropped to 31.4% of the original signal but recovered to 75.61% of the original signal following a 20 min recovery period. Following a second excitation period, the signal dropped to 28.22% of the original signal, recovering to 73.18% following a second 20 min recovery period.
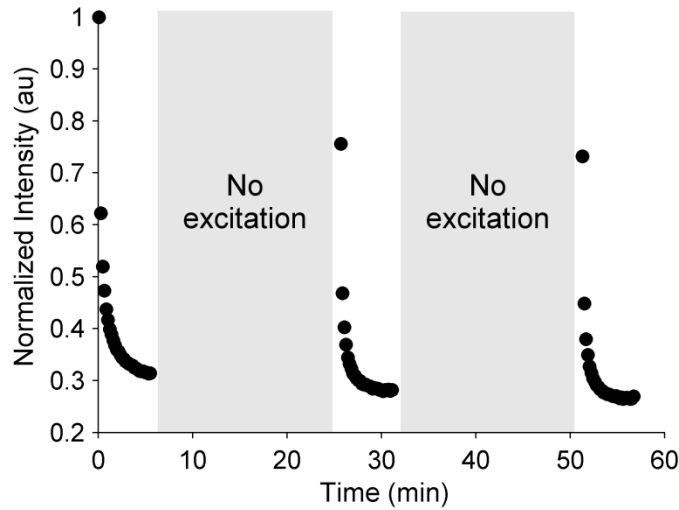
Figure 3. Recovery of ZnO nanoparticle luminescence following 20 min recovery period (blocked excitation).

To further explore the reversible photobleaching phenomenon, the photobleaching rates of the three samples were analyzed using various excitation schemes (*i.e.*, continuous or periodic excitation) under constant flow of dry nitrogen. Following 30 sec of continuous excitation (350 nm, 1 mW, 75 mm focal length lens, 1 sec integration), nanoparticles, nanopods, and microrods exhibited 60.99% ± 8.88% (n=24), 22.82% ± 5.76% (n=20), and 8.99% ± 2.34% (n=23) photobleaching, respectively (Figure 4a). For the nanoparticle sample in particular, high variability between measurements may preclude the use of these materials for optical sensing. By modifying the excitation scheme, however, it was possible to reduce the variability among photobleaching measurements.

Employing periodic excitation – 1 sec exposure followed by a specified recovery period without excitation, ranging from 5 to 20 sec – reduced the standard deviation

16

observed among measurements following 30 exposures for most cases. Furthermore, increasing the recovery time to 10 or 20 sec contributed to a statistically significant ($p<0.01$) reduction in measured photobleaching compared with the 5 sec scheme for the nanoparticle sample. However, increasing the recovery time from 10 to 20 sec did not yield further benefits in photobleaching or variability. With an exposure time of 1 sec and recovery times of 5, 10, and 20 sec, the nanoparticles exhibited 64.74% ± 2.58% (n=5), 55.57% ± 3.94% (n=5), and 53.30% ± 3.97% (n=5) photobleaching, respectively, after 30 exposures (*i.e.*, 30 sec total excitation). For the same periodic excitation schemes, the nanopods experienced 22.40% ± 3.53% (n=4), 27.34 ± 2.81% (n=3), and 27.38% ± 2.52% (n=4) photobleaching after 30 exposures. Likewise, the microrods experienced 12.52% ± 4.18% (n=3), 13.01% ± 2.81% (n=3), and 10.33% ± 2.83% (n=3) photobleaching after 30 exposures. These results are displayed graphically in Figure 4b.
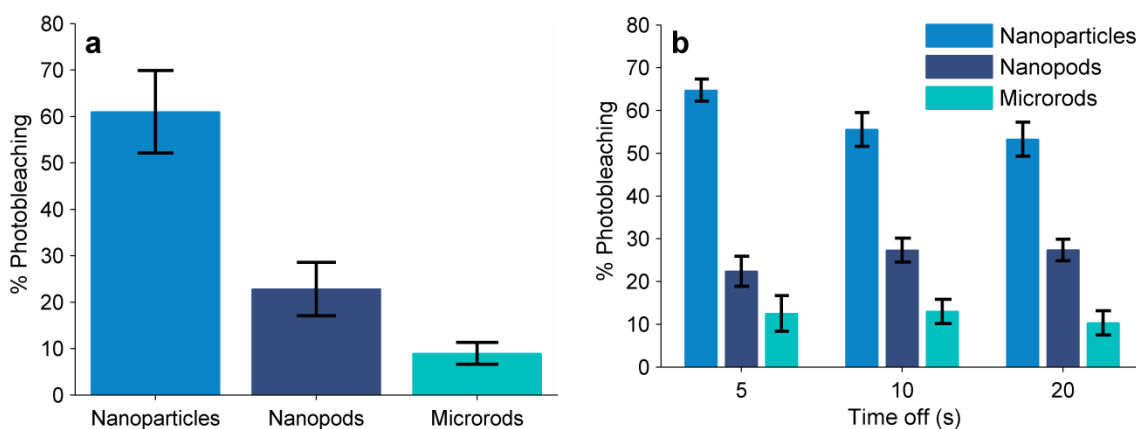
Figure 4. (a) Percent photobleaching of ZnO samples following 30 sec of continuous excitation (1 mW, 350 nm). (b) Percent photobleaching of ZnO samples after 30 exposures of periodic excitation. Each 1 sec excitation is followed by either 5, 10, or 20 sec of recovery time during which the laser beam is blocked.

Using the size dimensions summarized in Table 1, the surface area to volume ratios of the three ZnO nano/microstructures were calculated and compared with their associated photobleaching characteristics. The percentage of photobleaching increased with increasing surface area to volume ratio for both continuous (Figure 5a) and periodic (Figure 5b) photobleaching schemes, indicating an increasing reactivity with surface area to volume ratio. This reactivity is related to surface states, which have a higher contribution to the luminescence emission in smaller structures possessing higher surface area to volume ratios. These results agree with findings in the literature. Ghosh *et al*. showed that the sensitivity of the sample to the environment is size-dependent, with sensitivity increasing as particle size decreases [47]. Similarly, Eriksson *et al*. showed that ZnO nanoparticles have higher sensitivity than films, owing to the higher surface area to volume ratio [48].
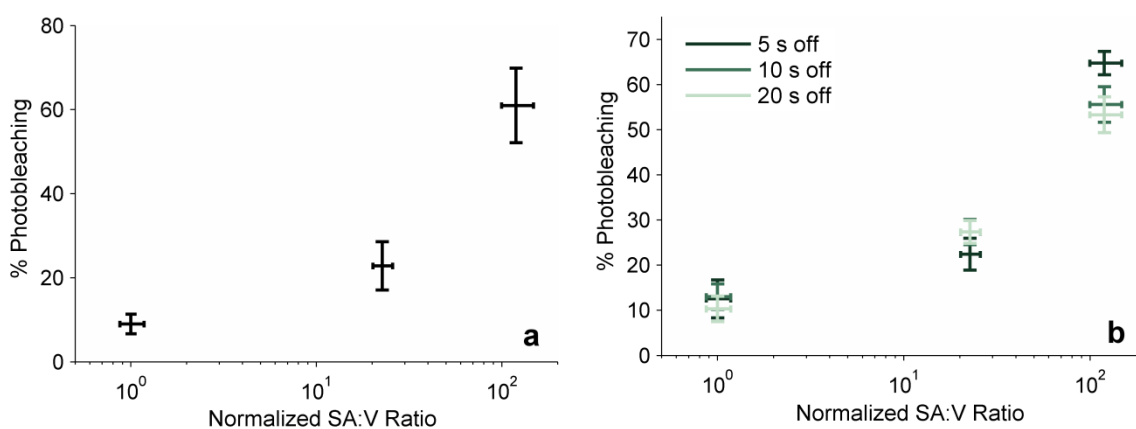
Figure 5. Percent of photobleaching following 30 sec of total excitation as a function of surface area to volume ratio due to 1 mW of (a) continuous excitation at 350 nm and (b) periodic excitation at 350 nm using exposure schemes of 1 sec excitation followed by recovery times of 5, 10 or 20 sec.

18

2.3.3 Environmental Effects on ZnO Luminescence

Prior to applying the samples as humidity sensors, the effect of the type of carrier gas on luminescence was first analyzed. The signal change for each ZnO sample in dry nitrogen was previously determined during the continuous photobleaching experiments. As such, the sample chamber was equilibrated to a dry air environment, and the change in signal for each ZnO sample was observed. The data for both carrier gases are summarized in Table 2. For both microrods and nanopods, continuous photoexcitation caused a decrease in the signal level for both environments. However, the nanoparticles exhibited a drastic difference between the two carrier gas environments, as the luminescence increased upon exposure to light in a dry air environment. This finding is indicative of an interaction between gas components within air (*i.e.*, other than nitrogen) and ZnO nanoparticles in the presence of continuous excitation. Furthermore, this is consistent with findings by Ghosh *et al.* that introduction of oxygen into an evacuated chamber with ZnO nanoparticles results in an increase in luminescence over ZnO nanoparticles in air [47].

Table 2. Change in signal in response to exposure to continuous excitation for 30 sec in different gas environments.

	Dry Air	*Dry Nitrogen*
Nanoparticles	**+32.68%**	-60.99%
Nanopods	-18.60%	-22.82%
Microrods	-9.84%	-8.99%

The reactivity of the nanoparticle sample was further investigated by adjusting the excitation scheme during data collection under a constant flow of dry nitrogen (Figure 6a). Similar with the results in Table 2, the signal initially decreased upon exposure to UV excitation in a dry nitrogen environment. Periodic blocking of the excitation beam resulted in an increase in signal for the nitrogen environment, where each decrease in the length of recovery time resulted in increasingly smaller changes in signal when switching between continuous and periodic excitation. For example, the absolute differences between maximum quenching during continuous excitation and maximum signal recovery during 1 sec excitation followed by either 20, 10, or 5 sec recovery periods (calculated on either side of the recovery period) were $31.80 \pm 3.24\%$, $22.47 \pm 0.06\%$, and $15.14 \pm 0.06\%$, respectively. In contrast, nanoparticles in a dry air environment exhibited the opposite reaction when changing between continuous and periodic excitation schemes. Consistent with the results of Table 2, nanoparticles exhibited an increase in signal upon exposure to continuous excitation in a dry air environment, as shown in Figure 6b. However, when exposed to periodic excitation, luminescence decreased following a biexponential curve. This pattern continued upon cycling between continuous and periodic excitation schemes.
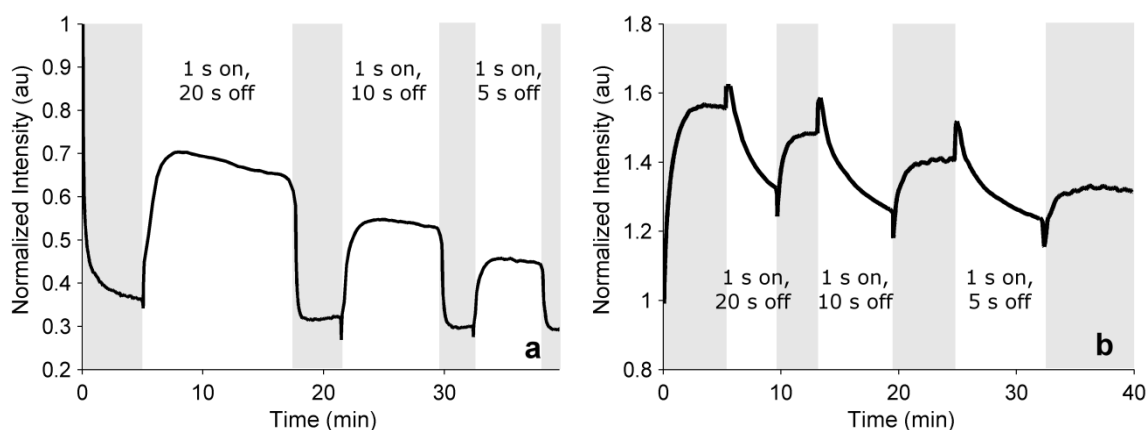
Figure 6. Luminescence response to changes in excitation scheme in (a) dry nitrogen and (b) dry air. Grey areas represent segments of time during which the sample received continuous excitation. As indicated, the other regions are time periods of periodic excitation (left: 1 sec excitation followed by 20 sec recovery time, middle: 1 sec excitation followed by 10 sec recovery time, and right: 1 sec excitation followed by 5 sec recovery time).

Comparison of the photobleaching results among the three size regimes coupled with the environmental results indicates that the nano/microstructure surface is key to the interesting optical properties observed with ZnO. It is hypothesized that the ZnO nanoparticles, with heightened reactivity to photoexcitation and changes in environment, have the greatest potential for serving as environmental sensors with high sensitivity.

2.3.4 Humidity Sensing

As shown above, ZnO nanoparticles exhibit sensitivity to their environment, as demonstrated by their reaction to various excitation schemes in the presence or absence of oxygen. This is further verified in Figure 7, which demonstrates the effect of dry nitrogen, humid nitrogen, and ambient air exposure on ZnO nanoparticle luminescence. Following signal stabilization in dry nitrogen, ZnO luminescence increased upon

exposure to ambient air, presumably due to the increased percentage of oxygen present.

Conversely, introduction of humid nitrogen has the effect of decreasing luminescence

below the level of dry nitrogen.
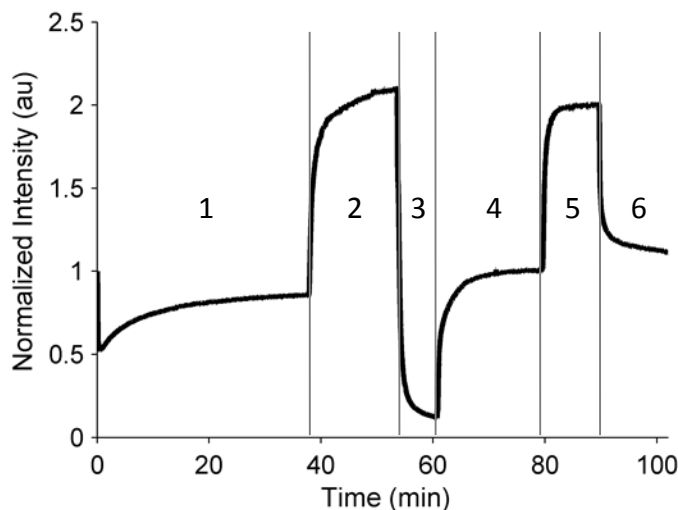
Figure 7. Luminescence of ZnO nanoparticles in different environments: (1) dry
nitrogen; (2) ambient air; (3) humid nitrogen; (4) dry nitrogen; (5) ambient air; and (6)
dry nitrogen. Ambient air, likely due to the presence of oxygen, results in an increase in
luminescence.

To rule out effects of interferents that may cause an undesired signal change, a

single carrier gas was used for humidity sensing experiments (*i.e.*, nitrogen or air). To

control the humidity level in the sample chamber, flow rates of dry gas and humid gas

exiting a custom-built humidifier were varied at pre-determined values to obtain the

desired humidity level over the range of the humidity analyzer (*i.e.*, 20-90% RH). Prior

to photoexcitation for each humidity level tested, the sample chamber was equilibrated

with dry gas. The sample was then photobleached until the signal reached and

maintained a steady-state level; thus, changes in signal would not be due to photobleaching of the sample.

Using results from the photobleaching experiments, the optimal excitation scheme to employ for humidity sensing experiments was determined to be periodic excitation with a 1 sec excitation followed by a recovery time of 10 sec. This periodic timing scheme results in variability among measurements similar to or better than continuous excitation. For nanoparticles – the focus of the humidity sensing presented in this paper – 1 sec excitation with a 10 sec recovery period results in a statistically significant reduction in photobleaching compared with 1 sec excitation with 5 sec recovery; further reductions in measured photobleaching or standard deviation are not realized when moving to a longer recovery period of 20 sec.

2.3.4.1 Humidity sensing with nanopods and microrods: Preliminary work highlighted the humidity sensing capabilities of ZnO nanopods as a proof of concept for using ZnO nanostructures as optical environmental sensors [45]. The nanopods displayed a sensitivity to humidity of 0.0032 RH^{-1} across a linear range of 22–70% RH.

Upon changing the environment from dry nitrogen to humid nitrogen, the ZnO microrods exhibited a 10.69 ± 2.74% decrease in signal, regardless of the humidity level between 31% and 90% RH. Representative curves displaying the humidity response of ZnO microrods in 41% and 71% humidity are shown in Figure 8a and b, respectively. Thus, rather than displaying a trend with humidity, the rods display an on-off signal change when exposed to humidity, making them poor candidates for humidity sensing.
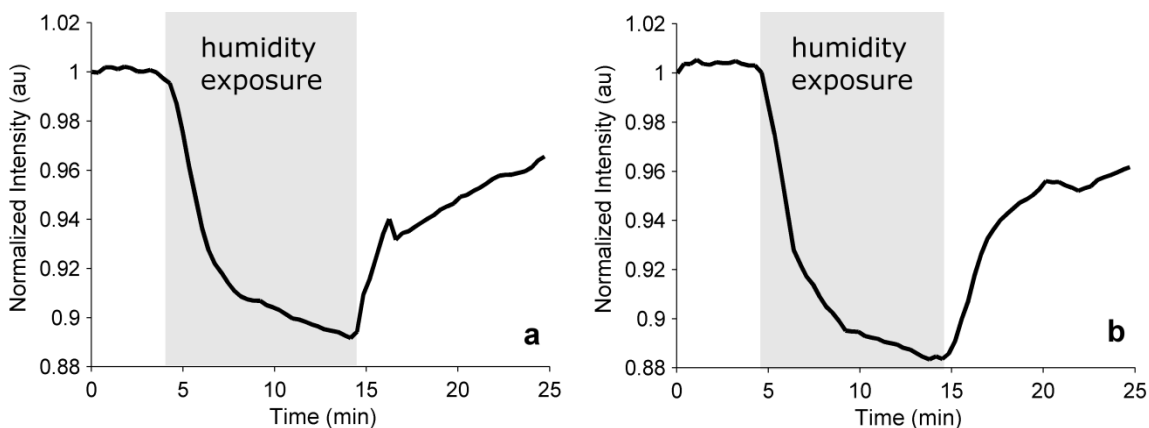
Figure 8. Representative response of ZnO microrods to changes between 0% RH and humidity levels of (a) 41% and (b) 71% RH in nitrogen.

2.3.4.2 Humidity sensing with nanoparticles in nitrogen: In a nitrogen environment, ZnO nanoparticles exhibited a large decrease in luminescence in response to an increase in local humidity. A typical humidity curve is shown in Figure 9a. Following a 10 min purge with dry nitrogen, a mixture of dry and humid nitrogen at the desired humidity level was introduced into the system, causing a momentary increase and subsequent decrease in signal intensity below the dry nitrogen level. Upon return to dry nitrogen, the signal recovered to its initial level prior to humidity exposure. A calibration curve for humidity sensing was developed using % change$= \frac{I_{dry}\text{-}I_{humid}}{I_{dry}} \times 100$, where I_{dry} is the average signal in a dry gas environment prior to humidity exposure and I_{humid} is the average signal at the end of the humidity exposure. As shown in Figure 9b, the *% change* in luminescence increased with humidity, following a linear trend with $R^2 \approx 0.98$. It should be noted that, for all humidity levels other than 24% RH, the luminescence recovered to within 5% of the original dry nitrogen signal level within

24

approximately 30 min. The nanoparticles displayed a measurement range from

approximately 23% to greater than 90% (*i.e.*, the maximum range of the humidity

sensor) with a sensitivity of 0.65% change in optical signal per % RH or a normalized

sensitivity of 0.008417 RH^{-1}. By cycling between 0% RH nitrogen and 90% RH

nitrogen, the reversibility of the ZnO nanoparticle sensor was shown (Figure 10).
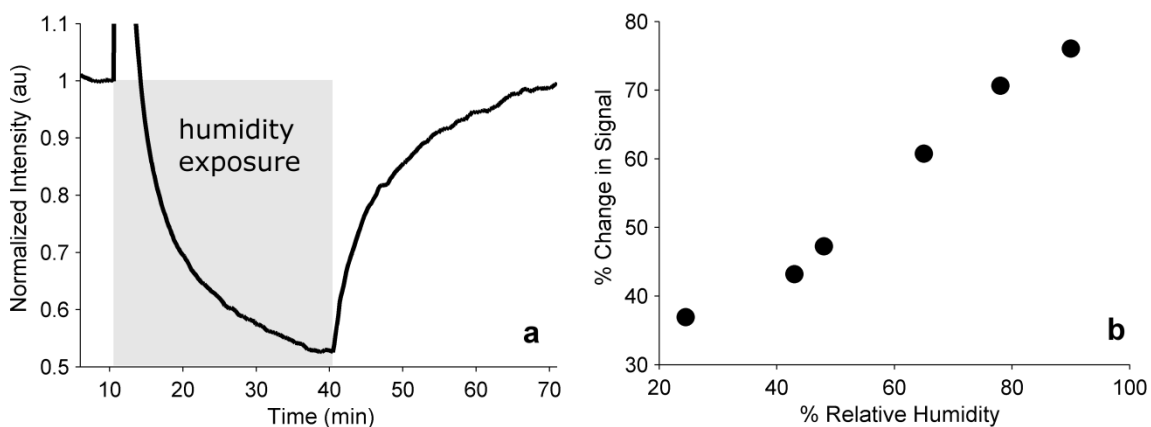
Figure 9. (a) Typical luminescence response of ZnO nanoparticles in response to a 10 min dry nitrogen purge followed by a 20 min exposure to nitrogen with an increased humidity level and a 30 min purge with dry nitrogen. (b) Optical response of ZnO nanoparticles to various % RH levels. The curve follows a linear trend, with % change in optical signal increasing with increasing % RH.
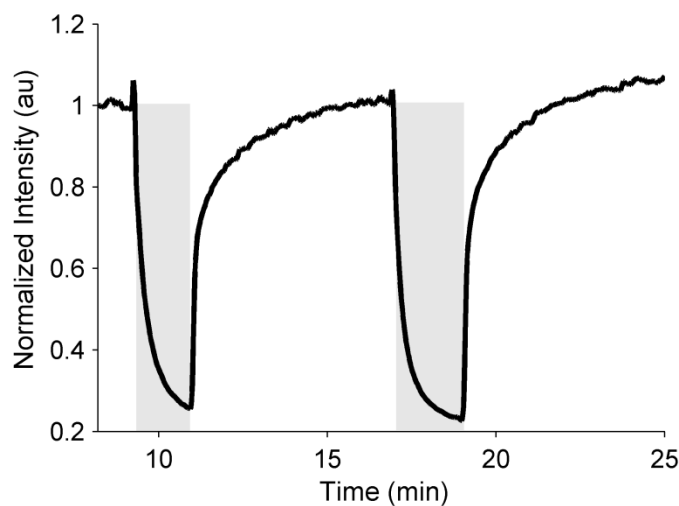
Figure 10. Reversibility of the ZnO nanoparticle sensor was demonstrated by cycling between 0% RH nitrogen and greater than 90% RH nitrogen (grey regions).

2.3.4.3 Humidity sensing with nanoparticles in air: Upon changing the carrier gas from nitrogen to air, the ZnO nanoparticles displayed more rapid, yet muted responses to changes in local humidity. Figure 11a displays sample response curves of ZnO nanoparticles to 54% (dark blue) and 66% (light blue) humidity in air. The muted response is likely a result of competing reactions between air and humidity. As shown in Table 2, ZnO nanoparticles exhibited an increase in luminescence upon excitation in air, while the opposite was seen in a nitrogen environment. Given that humidity has the effect of reducing luminescence, it follows that a reduced effect of humidity would be observed in an air environment.
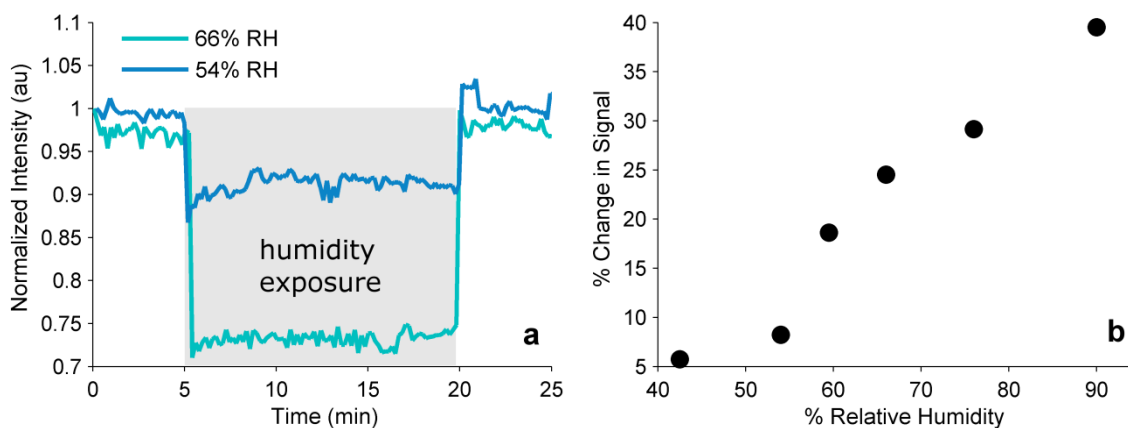
Figure 11. (a) Response of ZnO nanoparticles to changes from 0% RH to 54% RH (dark blue) and 66% RH (light blue) in air. (b) Response of ZnO nanoparticles to changes in humidity within an air environment.

As shown in Figure 11b, the *% change* in luminescence increased with humidity, following a linear trend with $R^2>0.95$. Although the percent signal change is less in an air environment, the nanoparticles exhibited increased sensitivity in the range of 40–90% RH compared with the response in nitrogen. The nanoparticles displayed a measurement range from 43% to greater than 90% with a sensitivity of 0.75% change in signal per %RH or a normalized sensitivity of 0.01898 RH^{-1}. Below 43% RH, our system could not discern changes in signal in response to changes in humidity.

The normalized sensitivity for ZnO nanoparticles to changes in humidity in nitrogen and air are 0.008417 RH^{-1} and 0.01898 RH^{-1}, respectively. In air, the ZnO nanoparticles presented in this paper show an increased sensitivity to humidity when compared with published normalized sensitivity values of (1) 0.00784 RH^{-1} for luminescence-based sensing with nanowires having widths of 300 nm [37], (2) 0.014 RH^{-1} for optical transmission-based sensing with a ZnO nanorod-coated optical fiber

[40], and 0.0012 RH^{-1} for optical transmission-based sensing using an optical fiber coated with a nanoparticle-doped film [39].

2.4 Conclusions

The photobleaching dynamics of three ZnO nano/microstructures were investigated using continuous and periodic UV excitation. Based on these findings, a periodic excitation scheme was employed for optical humidity sensing with 4 nm ZnO nanoparticles. The defect-related photoluminescence band was integrated from 450 nm to 690 nm and analyzed in response to variations in the local humidity level. The nanoparticles displayed a linear response with sensitivities of 0.65% change in signal per % RH (normalized sensitivity of 0.008417 RH^{-1}) and 0.75% change in signal per % RH (normalized sensitivity of 0.01898 RH^{-1}) in nitrogen and air, respectively. Given these results, this platform technology has great potential to be applied to other environmental gases.

3. ENCAPSULATION OF FITC TO MONITOR EXTRACELLULAR PH: A STEP TOWARDS THE DEVELOPMENT OF RED BLOOD CELLS AS CIRCULATING BLOOD ANALYTE BIOSENSORS[*]

3.1 Background

Analysis of various blood parameters provides insight into critical aspects of a patient's physiological or biochemical state, thus providing information about organ function and disease status. Examples of important blood parameters include pH, catecholamines, and glucose, which at elevated levels is linked to diabetes [49].

3.1.1 Clinical Relevance of Blood pH

Blood pH is tightly regulated in the body between pH 7.35 and 7.45, the narrow range over which cellular metabolism and organ function are optimized. Carbonic acid and bicarbonate serve as the buffer pair in blood that is primarily responsible for maintaining the narrow physiological pH range. The pathophysiologic disturbances, either metabolic or respiratory, that increase or decrease hydrogen ion concentration (H^+), measured as pH and responsible for the acid-base level of the blood, are termed acidosis (*i.e.*, increase H^+ ion concentration/decrease pH) and alkalosis (*i.e.*, decrease H^+ ion concentration/increase pH). Compensatory mechanisms (*e.g.*, hyper/hypoventilation) typically respond to changes in blood pH to return the pH to normal before acidosis or

---

[*] Parts of this chapter are reprinted with permission from "Encapsulation of FITC to monitor extracellular pH: a step towards the development of red blood cells as circulating blood analyte biosensors" by S. C. Ritter, M. A. Milanick, and K. E. Meissner, 2011. Biomedical Optics Express, **2**(7), 2012-2021, Copyright 2011 by OSA. The paper can be found at the following URL on the OSA website: http://dx.doi.org/10.1364/BOE.2.002012. Systematic or multiple reproduction or distribution to multiple locations via electronic or other means is prohibited and is subject to penalties under law.

alkalosis progresses to the more severe states of acidemia (pH less than 7.35) or alkalemia (pH greater than 7.45). If blood pH reaches levels outside of the pH range of 7.2–7.6, rapid intervention must take place to avoid adverse effects on the cardiovascular and central nervous systems [50].

Changes in blood pH accompany a variety of diseases, such as congenital lactic acidosis and diabetic ketoacidosis (DKA) [51, 52]. DKA is a life-threatening complication of diabetes resulting from the ineffective use or lack of insulin that leads to an increase in counter-regulatory hormones. The disease is characterized by hyperglycemia, acidosis, and increased levels of ketones [53, 54]. As such, treating patients with DKA requires management of multiple blood analytes, including blood glucose and the acid-base status (*i.e.*, pH), to ensure successful outcomes. Currently, the gold standard measurement for blood pH is sampling of arterial blood, which is both inconvenient and difficult, especially with infants and pediatric patients. A secondary method for estimating blood pH is measurement of transcutaneous pCO_2 or end tidal CO_2 levels [51, 55-57]. Although hourly samples are valuable, patients may experience rapid changes in blood pH and require immediate treatment. Thus, a long-term, continuous solution (*e.g.*, a biosensor) is requisite for more complicated and serious conditions.

3.1.2 Diabetes and Clinical Relevance of Blood Glucose

Diabetes mellitus is a set of metabolic disorders accompanied by hyperglycemia. These disorders may lead to a host of complications, including cardiovascular disease, retinopathy, nephropathy, and peripheral neuropathy. Diabetes was ranked as the 7th

leading cause of death in 2010 [58]. Type 2 diabetes is responsible for 90% of diabetic cases and is characterized by dysfunctional β-cells and insulin resistance. Although insulin resistance is compensated for by increased blood insulin levels at early stages of the disease, insulin production decreases over time, leading to hyperglycemia. Type 2 diabetes is becoming more common in all countries, regardless of development, and among younger individuals [59].

The International Diabetes Federation estimates that 382 million people worldwide (or 8.3% of the population aged 20-79) were living with diabetes in 2013; that number is expected to rise to 592 million (or over 10% of the population) by 2035. The prevalence of diabetes is highest among individuals living in low- and middle-income countries, which accounts for 80% of the total cases of diabetes but only 20% of total healthcare expenditures [60]. The effect of diabetes in the United States is of particular importance due to the increasing prevalence observed over the last few decades, which is expected to continue. Between 1980 and 2006, the percentage of the U.S. population with diabetes increased from 2.5% to 5.8%. Looking forward, models indicate that 1 out of every 3 children born in the U.S. in 2000 will develop diabetes in his or her lifetime [61]. The burden of diabetes and its complications – in terms of monetary expenditures, quality of life, *etc*. – is vast and highlights the need for a successful prevention and management strategy for diabetes. Thus, a glucose monitoring system that provides long-term, near-continuous or on-demand blood glucose measurements is greatly needed.

3.1.2.1 Electrochemical glucose monitoring: Due to the physiological importance and broad-reaching benefits of proper glucose control for individuals with diabetes (*e.g.*, delay or prevention of diabetes-related complications), glucose monitoring devices have been the subject of fervent research for over four decades [62-64]. The first enzyme-based sensor for blood glucose measurements was developed by Clark and Lyons in 1962 [65]; since that time, research into the development of reliable glucose biosensors has grown, now accounting for 85% of the biosensor market [66]. Traditionally, blood glucose measurements have been based on an electrochemical reaction between an enzyme, primarily glucose oxidase, and glucose within the blood sample, which has been retrieved *via* a finger-prick.

The development of glucose biosensors over the last several decades has been reviewed in depth in a number of reports [66-69]. Initial enzymatic biosensors detected glucose *via* a glucose oxidase-catalyzed reaction between glucose and oxygen that produced hydrogen peroxide and gluconic acid . Measurement of the increase in hydrogen peroxide or decrease in oxygen enabled quantification of glucose concentration [70]. One disadvantage of first generation biosensors was a dependence on oxygen concentration. A number of mechanisms have been developed to alleviate the associated errors, including the implementation of films to control transport of glucose and oxygen. Second generation biosensors implemented a nonphysiological electron acceptor (*i.e.*, mediator) that reacted rapidly with the reduced enzyme and mitigated the issue of oxygen dependence. Third generation biosensors aim to eliminate the mediator altogether, relying on direct electron transfer between enzyme and electrode [66-68].

32

Although enzyme implementation within these biosensors affords high sensitivity and selectivity for glucose, the sensors suffer from inadequate long-term stability as a result of the nature of the enzyme [68, 69, 71].

Nonenzymatic glucose sensors, which function through the direct electrochemical oxidation of glucose, aim to address the major pitfall of enzymatic glucose biosensors – long-term stability. Glucose oxidase suffers from thermal and chemical instability, and reproducibility among sensor batches is limited by the requirement for immobilization of the enzyme. Aside from reproducibility, an enzyme-less biosensor would afford a number of other important advantages, namely stability, simplicity, and freedom from oxygen effects. Despite these advantages, major issues facing the realization of nonenzymatic biosensors include insufficient sensitivity and selectivity as well as the irreversible adsorption of chloride ions and oxidation intermediates that hinders the electrode activity [67-70].

3.1.2.2 Continuous glucose monitoring: Standard finger-prick style glucose meters suffer from the disadvantage of providing mere snapshots of the glucose concentration over time, rather than a continuous trend of glucose changes throughout the day. Furthermore, the invasiveness of this technique serves as an obstacle to proper control of blood glucose levels through self-monitoring [49, 72]. Continuous glucose monitoring (CGM) would provide for stricter control over blood glucose levels leading to improved patient outcomes. This type of system would also provide insight into rapid glucose fluctuations and allow for the proper therapeutic response to be administered [66].

Recent studies have evaluated the efficacy of CGM systems with respect to various patient outcomes. Gandhi *et al.* conducted a meta-analysis of 19 trials. CGM resulted in a reduction in mean HbA1c in patients with Type 1 and Type 2 diabetes. Although trial participants generally felt favorably towards the CGM systems, some users felt the systems were inconvenient and led to difficulties with sleeping and athletic activities [73]. Similarly, other studies have shown superior glucose control with CGM systems [74, 75].

Upon insertion in the body, CGM systems face a number of significant challenges to long-term implementation, towards which much research has been dedicated. Commercial CGM systems employ proprietary membranes to induce selectivity to glucose as well as reduce effects caused by fluctuations in oxygen concentration. To create an environment that favors reaction between the enzyme, glucose, and oxygen (*i.e.*, 1:1 stoichiometric reaction between oxygen and glucose), membranes are employed to reduce diffusion of glucose to create an excess of oxygen, as glucose is naturally present at a significantly higher concentration than oxygen. Calibration with the standard finger-prick test is required as the *in vivo* response of these sensors differs considerably from the *in vitro* response. As a time lag of 5 to 30 min exists between the levels of glucose in the blood and interstitial fluid, where the CGM system is placed, careful attention must be given to the time of calibration [76].

The most significant challenge for an implanted CGM system is the foreign body response, with an initial acute phase characterized by a decrease in sensitivity and stability as the body attempts to eliminate the foreign body and heal the wound. This

34

phase is distinguished by the adsorption of proteins, release of cytokines and reactive

oxygen species, and finally an arrival of inflammatory cells. Following the acute phase,

a fibrous capsule is formed around the implant, inhibiting diffusion of glucose and

oxygen into the sensor. Improving biocompatibility and increasing *in vivo* lifespan may

be accomplished through prevention of protein adhesion or mediation of inflammatory

response [76-78]. Yoshikawa *et al.* demonstrated that a nano-structured architecture of

concentrated polymer brushes deters protein adhesion [79]. Gifford *et al.* demonstrated a

reduction in the inflammatory response for glucose sensors that release nitric oxide [80].

Several CGM systems are currently commercially available for at-home use:

Abbott's Navigator 2 (not available in U.S.); Dexcom's G4 Platinum; and several

products from Medtronic, including the Guardian® REAL-Time CGM System [81-83].

Compared with earlier generations of these technologies, the latest CGM systems offer

improved sensor and software performance to address issues of nonselectivity, oxygen

dependence, and *in vivo* instability. These systems also aim to improve user experience

and safety. Nevertheless, measurement of quality of life with CGM is similar to

traditional glucose monitoring, likely due to the inconvenience of use (*e.g.*, insertion of

sensor). Furthermore, the sensors used in conjunction with these systems must be

replaced every 6-7 days [76, 81].

3.1.2.3 Nonelectrochemical glucose monitoring: The above glucose biosensors

all rely upon an electrochemical reaction that suffers from consumption of glucose and

the requirement that the sensor be in direct contact with the sample. Nonelectrochemical

biosensors aim to address these problems by employing other techniques, such as optical

measurements [84]. For example, Aslan *et al.* employed a plasmon-based approach for

glucose measurements. Dextran-coated gold colloids were aggregated through addition

of concanavalin A (ConA); in the presence of glucose, plasmon changes were observed

due to competitive binding between glucose and ConA, which disrupts the aggregates

[85]. Alexeev *et al.* employed a crystalline array of colloidal particles within a hydrogel

network with attached boronic acid recognition agents. Upon binding with glucose, these

recognition agents cause a blueshift in the diffraction pattern that is representative of the

glucose concentration. The change in color of the material, which will be incorporated

into an ocular insert or contact lens, can be observed visually [86]. Malik *et al.*

investigated the use of dual-wavelength polarimetry to measure glucose concentrations

in the aqueous humor of the eye. The implementation of a second wavelength allows the

authors to minimize noise in the system due to time-varying corneal birefringence [87].

Enejder *et al.* utilized Raman spectroscopy to transcutaneously measure blood glucose

levels in individuals with heightened glucose levels. Using this technique, the authors

obtained good calibration results, with a mean R^2 value of 0.83 for the 17 subjects [88].

Robinson *et al.* measured glucose levels of the fingertip using transmission-based NIR

spectroscopy. Viability of the technique was verified though a chemometric multivariate

calibration method [89]. The above optical techniques aim to address some of the

concerns of electrochemical methods by reducing the invasiveness of the measurement.

However, none of these techniques has become commercially-available. Thus, there

remains a need for a minimally-invasive, inexpensive, long-term blood analyte sensing

system that takes advantage of the sensitivity of optical methods.

3.1.3 Encapsulation within RBCs

As an alternative, we propose that the sensing chemistry may be entrapped within RBCs using a hypotonic dilution method, as depicted in Figure 12. The cartoon illustrates the envisioned concept in which a small portion (*e.g.*, 1 unit or less) of a patient's blood would be removed, loaded with the analyte-sensitive fluorescent tag(s), and transfused back into the blood stream. This reintroduction process would be analogous to platelet donation, in which whole blood is removed, processed by a cell separating machine to remove platelets, and remaining components returned to the donor [90]. The resealed ghosts would then circulate for the remainder of the 120 day lifespan, reporting on analyte levels upon excitation by an external light source (*e.g.*, laser diode). Rather than loading the entire distribution of RBC ages, it may be possible to preferentially load young RBCs, using one of many separation techniques based on cell density, cell size, surface charge, or osmotic fragility [91], and increase the circulation time of the sensors. While loaded, the fluorescent tag(s) would be shielded from the body, avoiding the immune response associated with many of the other long-term, *in vivo* sensors. Upon death of the loaded RBCs, it is expected that the fluorescent tag(s) would be filtered from the bloodstream. Although future work on the toxicity of the final fluorescent tag(s) must be completed, the FDA approval of indocyanine green for human use paves the way for *in vivo* application of other fluorescent dyes [92].

As proof-of-concept, the pH-sensitive, visible-wavelength dye, fluorescein isothiocyanate (FITC), was encapsulated within RBCs and used to monitor extracellular pH levels. This wavelength region is ideal for common fluorescence spectroscopy

equipment and microscopes, enabling straightforward data collection of fluorescence

levels and visualization of the dye distribution within the resealed RBCs. The long-term

goal, however, is encapsulation of an NIR, glucose-sensitive dye for the continuous

monitoring of glucose for diabetic patients – a goal with broad-reaching implications.
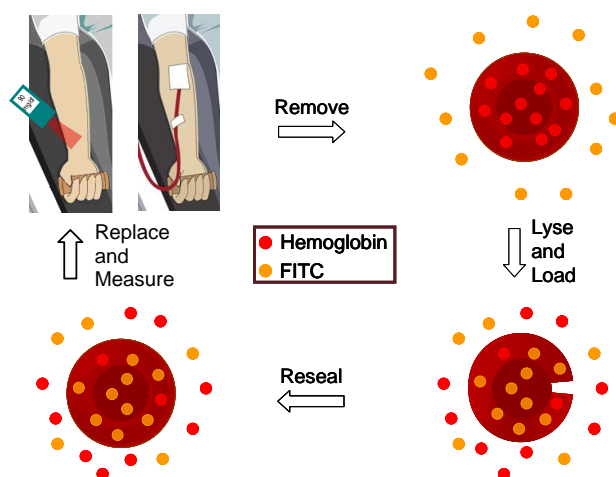
Figure 12. Cartoon illustrating the RBC sensing platform concept. A small portion of blood is removed from the patient; the blood is washed, loaded with the analyte-sensitive fluorescent dye, resealed, and then transfused back into the patient. An excitation light source is then directed at the wrist; the emission from the resealed red cell ghosts is collected and converted into an analyte concentration. Clip art used with permission from Microsoft.

Efforts to entrap chemicals within RBCs began in the early 1950s with the

successful encapsulation of ATP (as reviewed in [93]) and then, in 1959, various

molecular weight dextrans [94]. In 1973, RBCs were first used as delivery vehicles for

therapeutic agents by two independent groups [95, 96]. Since these early studies, the

advantages of RBCs (*e.g.*, biocompatibility, biodegradability, long life time) have

continued to drive the development of RBC carriers for delivery of biopharmaceuticals. Several excellent reviews on drug delivery using RBCs as biocompatible carriers are available [97-99].

There are a number of ways in which to encapsulate substances within RBCs, which have been reviewed previously [93, 100-103]. Briefly, osmosis-based techniques include the hypotonic dilution, dialysis, and preswelling methods. The dilution technique is rapid and requires no special equipment, but the resulting resealed cells have lost a large proportion of their intracellular components, resulting in short circulation times *in vivo*. The latter two methods maintain near-normal Hb levels within the RBCs and may result in resealed cells with near-normal lifespans. The preswelling technique is simpler than the dialysis technique and shows higher entrapment efficiency. Other loading techniques include the osmotic pulse method (*i.e.*, encapsulation of drug due to diffusion of DMSO), chemical perturbation (*i.e.*, exposure to chemicals leading to irreversible damage), and electroporation (*i.e.*, exposure of cells to an applied electric field to open pores and allow drug encapsulation). The electroporation method results in more uniform loading and long lifespans in circulation but requires specialized equipment. More recently, a novel means of encapsulation within RBCs delivered the load across the membrane using cell-penetrating peptides. Drugs were loaded into RBCs using carrier proteins to avoid the destructive characteristics, such as disruption of the membrane, of more traditional loading techniques [104, 105]. Using these methods, a multitude of drugs, including those based on amino acids, proteins, and enzymes, have been investigated for their use in RBC drug delivery systems. As an alternative

application, ICG-loaded RBCs were used to study the hemodynamics of the retinal capillaries and choriocapillaris [106]. However, prior to the work presented herein, resealed RBCs had not yet been explored, to the best of our knowledge, as a means of monitoring extracellular analyte levels within the blood.

3.1.4 RBCs

RBCs are primarily responsible for carrying oxygen from the lungs to other tissues throughout the body *via* the bloodstream. When mature, RBCs lack a nucleus as well as many other cellular organelles considered vital for normal cellular function. As a result, RBCs can neither divide nor perform self-repair, such as the regeneration of damaged proteins [107]. Normal human RBCs are biconcave disk-shaped cells with an average diameter and thickness of 8 µm and 1.7 µm, respectively [108]. The average lifespan of an RBC is 120 days, after which the senescent RBCs are removed from the bloodstream by the reticuloendothelial system (*i.e.*, spleen and liver), which sense damage to the RBC membrane and pit or remove the damaged areas [107].

A number of theories have been put forth to explain RBC senescence which have been summarized by Steinberg *et al*. [107]. The first theory relies on the loss of RBC membranes during the pitting process. Normal, biconcave RBCs have a volume of 90 fL and surface area of 140 μm^2, a considerably higher surface area than is needed for a spherical particle of the same volume. However, the biconcave shape allows the RBCs to traverse through capillaries that are only one-third to one-half the diameter of the cell. Thus, if aging RBCs lose membrane material and become more spherical and rigid, it follows that these cells would have more difficulty traveling through the blood stream,

leading to cell death. A second theory postulates that RBC death is due to loss of enzymes responsible for maintaining the redox status of the cells. As a result, RBC lipids and proteins would become oxidized, leading to critical changes to the membrane, ultimately resulting in cell removal. A final theory proposes that RBC death results from an immune response. Normal oxidative damage has been shown to result in clustering of band 3 molecules, which are recognized and bound by an isoantibody, leading to removal by the reticuloendothelial system.

Hb is a 64 kD protein responsible for carrying oxygen to bodily tissues and is the major intracellular protein of RBCs. The role of RBCs, then, is to protectively package this vital protein, which would otherwise be rapidly excreted by the body in its free form. Hb is composed of four globular protein subunits; each subunit contains a heme group – a heterocyclic ring with an iron atom at its center that can carry a single oxygen molecule. Cooperativity among the four subunits leads to a sigmoidal oxygen dissociation curve. Essentially, the presence of each bound oxygen positively influences oxygen binding to the other subunits [107, 109]. A RBC will pass through the circulatory system approximately 10^5 times during its 120 day life span to carry oxygen to the tissues. The high surface area of the cell allows for a large area over which oxygen can diffuse out of the RBC into the tissues. In the body, Hb can present itself as oxyhemoglobin or deoxyhemoglobin, depending on whether the protein is saturated or desaturated with oxygen, respectively [108].

The RBC membrane, composed of lipids and proteins in equivalent weights, performs a number of important functions for operation and transport in the body [110].

41

To perform its necessary tasks, the RBC membrane showcases a number of specialized characteristics, namely having elasticity and strength as well as a rapid response to fluid stresses. These abilities arise out of the membrane structure – a plasma membrane anchored to an elastic skeletal protein network [111]. The membrane is comprised of three layers: (1) the external layer, the glycocalyx, has a high concentration of carbohydrates; (2) the middle layer is a lipid bilayer with associated transmembrane proteins; and (3) the inner layer is a protein network known as the RBC membrane skeleton [112]. The lipid bilayer is composed, by weight, of equal parts cholesterol and phospholipids [111] and contributes to the permeability and fluidity of the membrane [110]. Proteins within the membrane skeleton, predominately spectrin, play a stabilizing and strengthening role in the membrane, providing a means for the membrane to deform through small capillaries and subsequently recover to a biconcave shape [112].

The hypotonic dilution method mentioned above takes advantage of the RBC membrane's ability to reversibly swell in response to the osmolarity of the extracellular environment [93, 113-115]. In this procedure, the RBCs are placed in a low osmolarity solution (*i.e.*, lysis solution) at 0 °C, which causes the membranes to swell and develop pores that are estimated to range from 10 to 500 nm [93, 115-117]. While the pores are open, Hb and other molecules within the cell and fluorescent probes as well as salts in the lysis solution equilibrate. Once physiological osmolarity and temperature are restored, the pores reseal, entrapping the fluorescent probe. These carriers exhibit biodegradability and, as autologous cells, biocompatibility, thereby avoiding the deleterious effects of the immune system response [93, 98, 99, 115, 117, 118].

Furthermore, resealed RBCs that have been returned to the body are able to circulate with a lifetime similar to normal RBCs [93, 113, 114, 119, 120]. Thus the sensors would have a lifetime of up to 120 days, depending upon the age of the RBCs at removal.

Furthermore, membrane proteins are responsible for important transport properties of the RBC membrane that lend themselves to biosensing. The existence of cell membrane transporters provide a route to report on extracellular analyte and ion levels by monitoring intracellular levels. Catecholamines – for example, dopamine, noradrenaline, and adrenaline – are a class of compounds transported across the membrane [121]. All mammalian RBC membranes contain the chloride-bicarbonate exchanger, one of several pathways for ion transport [122]. This transporter, which allows the intracellular pH to equilibrate to the extracellular level, is key to the proof-of-concept work shown in this dissertation (*i.e.*, the pH response of dye-loaded RBCs). RBC membranes of humans and other vitamin C-deficient mammals (*e.g.*, primates and guinea pigs) also contain the Glut1 protein, which is responsible for rapidly transporting (*i.e.*, seconds at body temperature [123]) and equilibrating glucose across the membrane [111, 124-127]. Future work targeting long-term glucose monitoring for diabetic patients relies upon this transport mechanism. Research on the effect of diabetes on the transport rates of Glut1 has not reached a consensus – some studies indicate an increased uptake [128] while others point to a decreased rate [129, 130]of glucose transport. Khera *et. al* demonstrated marked heterogeneity in the ratio of intra- to extracellular glucose levels among human RBCs [123] while Somogyi demonstrated no difference between the RBC to plasma glucose ratio of healthy and diabetic patients [131]. Although more research

would be needed for verification, these effects would likely not disrupt the ability of the proposed intracellular sensors to monitor extracellular blood glucose levels. Membrane transporters such as these allow for one to monitor intracellular analyte levels that are representative of extracellular levels – the characteristic exploited in the work presented in this dissertation.

3.2 Materials and Methods

3.2.1 Chemicals

Lysis solution components ($MgCl_2$, EDTA, urea, and phosphate buffer), KCl, fluorescein 5(6)-isothiocyanate (FITC), glycylglycine, NaCl, and phosphate buffered saline (PBS) were purchased from Sigma Aldrich (St. Louis, MO). Anti-fluorescein/Oregon Green, rabbit IgG was purchased from Invitrogen (Carlsbad, CA). Whole sheep blood in citrate was purchased from Hemostat Laboratories (Dixon, CA). FITC was reacted with 4.3-fold excess glycylglycine at pH 9 to form the glycylglycine-FITC conjugate. All solutions were prepared with deionized water, adjusted to pH 7.4 with HCl and NaOH, and stored at 4 °C.

3.2.2 Preparation of Dye-Loaded, Resealed Red Cell Ghosts

In this preparation, RBCs are diluted approximately 10 times with a dye-containing solution. The resulting RBCs are termed pink ghosts due to the low final concentration of entrapped Hb (*i.e.*, 10% of original). Low Hb ghosts were used in these initial experiments as Hb absorbance overlaps with the emission of the fluorescent probe. However, future work will involve the incorporation of NIR fluorescent probes within high Hb ghosts, providing complete functionality of the RBC sensors *in vivo*.

44

Whole sheep blood was washed three times with 165 mM NaCl through centrifugation (10,000 x g, 3 min) to remove plasma proteins and leukocytes; washed, packed RBCs were stored on ice until loading. The lysis solution (53 mL) consisted of 0.94 mM $MgCl_2$, 1.9 mM EDTA, 4.7 mM KH_2PO_4, 1 M urea, 0.947 mM glycylglycine, and 217 μM glycylglycine-FITC conjugate. This solution was stirred in a beaker surrounded by a salt water/ice mixture to maintain the temperature at 0 °C for the loading procedure. Once the loading solution cooled to approximately 0 °C, 5 mL of packed RBCs were added in a single injection. After 10 min, 5 mL of 1.65 M KCl were added to restore osmolarity. After another 10 min, the ghosts were transferred to a water bath at 37 °C for 25 min to complete the resealing process. Free glycylglycine-FITC conjugate, Hb, residual leukocytes and RBC debris were removed via aspiration following three centrifugation cycles (10,000 x g, 8 min for first wash, 6 min for successive washes). Resealed ghosts not immediately used were stored at 4 °C in 5 volumes of PBS.

3.2.3 Sensor Response and Spectral Data Acquisition

For pH experiments, 100 mM NaOH and HCl solutions were prepared in 165 mM NaCl to maintain the osmolarity of the local RBC environment. Resealed ghosts were added into room-temperature, isotonic NaCl until a sufficient fluorescence signal could be measured with the optical system. As approximately 90% of the Hb had been removed while making the resealed ghosts, 10 mM PBS was added to the resealed ghost solution to prevent large fluctuations in the extracellular pH.

3.2.3.1 Optical system for dynamic data: A frequency doubled Ti:sapphire laser (approximately 15 mW, Mira 900, Coherent, Santa Clara, CA) served as the excitation source ($\lambda \sim 440$ nm) for the resealed ghosts (λ_{ex},max = 492 nm). A short-pass filter was placed just after the doubling crystal to remove remaining excitation light (880 nm). Fluorescence emission (λ_{em},max = 518 nm) was collected at 90° with a spectrograph (Acton SpectraPro 2300i, Princeton Instruments, Trenton, NJ) attached to a CCD camera (PIXIS 100, Princeton Instruments, Trenton, NJ). For time-course measurements, the fluorescence signal was integrated over 500–570 nm. A pH probe (Orion 3 Star, Thermo Electron Corporation, Waltham, MA) was placed in the extracellular solution to simultaneously monitor extracellular pH throughout the entire experiment. All pH data was collected through HyperTerminal on the PC.

3.2.3.2 Optical system for static data: Fluorescence emission was collected with a fluorimeter (PTI, Birmingham, NJ) using an excitation wavelength of 488 nm. For time-course measurements, the fluorescence emission of a single wavelength (*i.e.*, 514 nm) was recorded for 20 to 30 sec. Extracellular pH of the experimental solution of resealed ghosts was continuously measured with the pH probe. Prior to data collection, anti-fluorescein antibody was added to the experimental solution to bind any free (*i.e.*, extracellular) glycylglycine-FITC conjugate, quenching its contribution to the fluorescence signal. The fluorescence emission of a 1 mL sample of the experimental solution was recorded; the corresponding pH was recorded and the sample returned to the experimental solution. The pH of the experimental solution was adjusted, solution thoroughly mixed, and the measurements were repeated for several pH steps.

For the emission spectra of free glycylglycine-FITC conjugate and resealed ghosts presented in this paper, the samples were excited using a 488 nm argon ion laser (model 163-M12, 25 mW, Spectra-Physics Lasers, Santa Clara, CA). Fluorescence intensity was collected using the spectrograph/CCD camera setup described in the dynamic data section.

3.2.3.3 In vivo data: All animal experiments received prior IACUC approval from the University of Missouri. Sprague-Dawley rats were administered isoflurane in conjunction with oxygen, which served as the anesthetic throughout the procedure. A catheter was placed in the femoral vein for injection of the dye-loaded ghosts or free dye. Hair in the vicinity of the optical probe location was shaved, and the optical probe was then secured in the proper location – in contact with the thigh tissue – for data collection throughout the experiment. In the first realization of the *in vivo* monitoring system, a white light source with a FITC excitation filter served as the excitation source for the loaded ghosts. Excitation was directed to the rat tissue through a standard bifurcated reflection probe (R400-7-UV-VIS, 6 illumination fibers around 1 collection fiber, Ocean Optics). Fluorescence emission was collected through the collection fiber, filtered with a FITC emission filter, and focused onto a spectrometer (USB-2000, Ocean Optics) operated with SpectraSuite software.

3.2.3.4 Testing of sensor integrity: To allow for comparison of intensity changes due to potential glycylglycine-FITC conjugate release, the fluorescence intensity value at 514 nm was collected for 30 sec. The fluorescence contribution of extracellular glycylglycine-FITC conjugate was quenched by addition of an anti-fluorescein antibody.

After the experimental time period of 30 min, the intensity value at 514 nm was collected for an additional 30 sec. A second aliquot of the anti-fluorescein antibody was added and thoroughly mixed with the resealed ghosts. A third fluorescence time-based scan was recorded for 30 sec for comparison.

3.3 Results and Discussion

Fluorescein has a pKa of 6.4, leading to pH-dependent fluorescence emission over the range of pH 5 to 9. For the experiments presented here, the fluorescein derivative, FITC, was conjugated to glycylglycine, rendering a cell impermeant compound—a requisite for stable encapsulation. The spectra of resealed ghosts and free glycylglycine-FITC conjugate (λex = 488 nm) are compared in Figure **13**. Encapsulation of the fluorescent dye within the RBCs does not alter its emission curve.
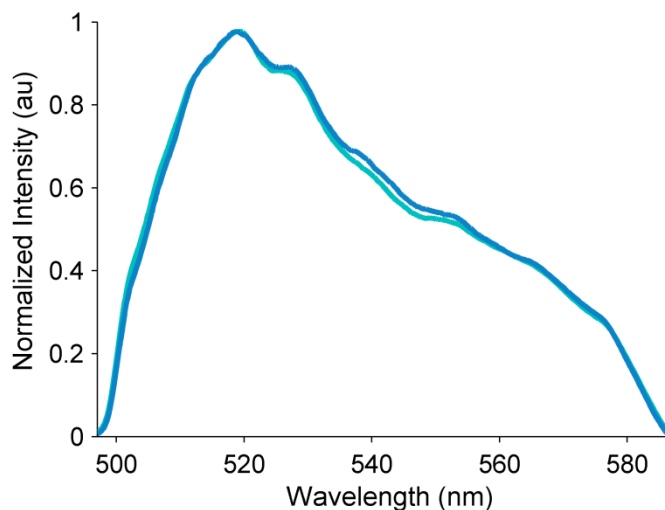
Figure 13. Comparison of fluorescence spectra of resealed ghosts (light blue) and free glycylglycine-FITC conjugate (dark blue) show that emission characteristics of the two solutions are nearly identical.

48

To investigate the fluorescence intensity response to pH, acid or base was added in 1 to 5 μl aliquots to vary the pH of the resealed ghost environment between pH 6.5 and 8.5. The resealed ghost solution was thoroughly mixed after each addition. For the dynamic data, the fluorescence intensity and pH signals were allowed to plateau prior to each acid/base addition to ensure that the resealed ghosts had sufficient time to equilibrate. The response time, defined as the length of time required for the signals to reach a steady state value, was typically less than one min. This response time most likely reflects the response time of the electronics and mixing time of the solution as the chloride-bicarbonate exchange system has a half time of less than 1 sec at 37 °C [132]. In the portion of the dynamic data shown in Figure 14, fluorescence intensity (integrated from 500 to 570 nm) tracks extracellular pH throughout the pH range of interest. The two curves exhibit similar characteristics in response to pH changes, including directionality, drift, and signal change for corresponding changes in pH values. The sensors demonstrate reversibility across the pH range throughout the 25 min of optical interrogation time (*e.g.*, two pH measurements of approximately 7, separated by 9 measurements over 16 min, had identical fluorescence intensity measurements within the experimental error of the system). This reversibility indicates that the optical system does not affect the membrane transporters or significantly photobleach the fluorescent probe. For the *in vivo* application of this sensor, the fluorescent probe would be subject to a significantly shorter excitation time (*i.e.*, approximately 1 min, or the response time of the sensor), and since the RBCs mix during circulation through the body, one would not expect that the same resealed ghosts would be found within the excitation volume for

49

consecutive measurements. Thus, it is easy to envision that similar reversibility would be

expected over the lifetime of the sensor.
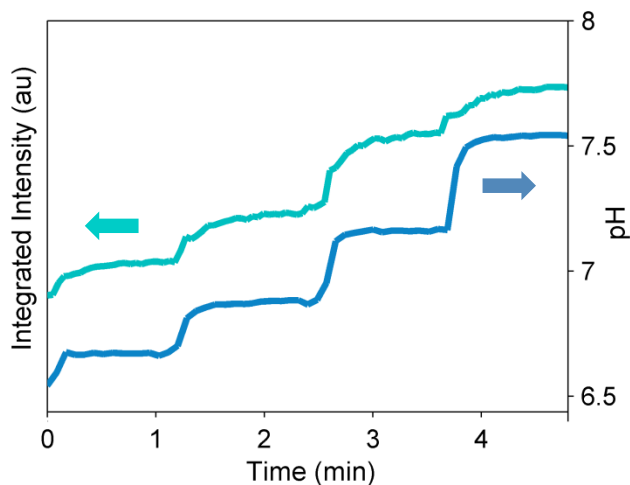
Figure 14. A representative portion of a pH trial performed on the dynamic system. Fluorescence intensity (light blue) of the intracellular pH-sensitive dye (FITC) tracks extracellular pH (dark blue).

The potential release of glycylglycine-FITC conjugate was investigated to

evaluate the integrity of resealed ghosts over the experimental time period (*i.e.*, 30 min).

In repeated testing, the extent of the subsequent decrease in the measured fluorescence

signal due to the first antibody addition varied between 9% and 46%. This variation in

the signal contribution is directly related to how well the resealed ghosts are washed at

the end of the preparation step (*i.e.*, removal of free glycylglycine-FITC conjugate);

more thorough washing will lead to a decrease in the measured contribution of free

glycylglycine-FITC conjugate. Measured fluorescence intensities before and after the

50

second addition of anti-fluorescein antibody (after 30 min) were the same value within experimental error, indicating no significant amount of extracellular glycylglycine-FITC conjugate. Thus we assume the RBC membranes did not release glycylglycine-FITC conjugate during the pH experiments.

A pH trial performed on the static optical system is shown in Figure 15. After quenching of the extracellular glycylglycine-FITC conjugate fluorescence contribution, extracellular pH was monitored with the fluorescence-based sensors. After each pH change, the fluorescence signal at 514 nm was monitored for 30 sec to provide sufficient data to develop an average fluorescence signal at each pH; the pH was recorded for each pH step. This system shows similar reversibility as the dynamic system, indicating that this system does not negatively affect the RBC membranes.
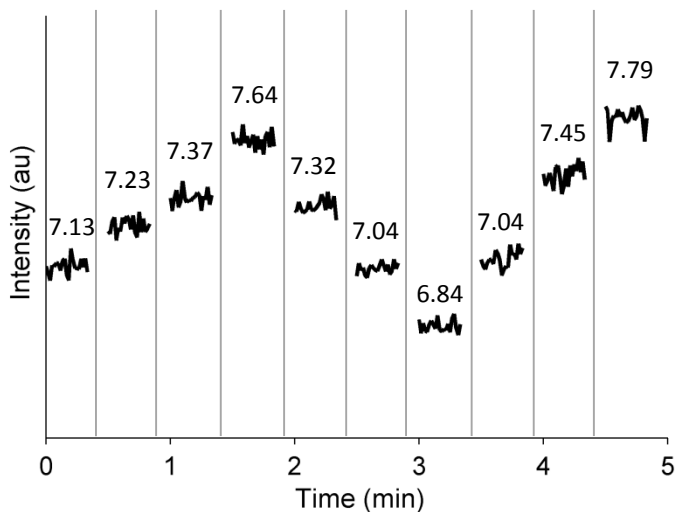
Figure 15. Fluorescence intensity responds to pH changes using the static system in which extracellular glycylglycine-FITC conjugate fluorescence is quenched by the anti-fluorescein antibody. Each segment is the middle 15 sec of a 30 sec fluorescence monitoring period. The grey lines indicate discontinuous data. The average pH is directly above each segment.

51

After data collection, fluorescence intensity and corresponding pH values were selected for each signal plateau of the two pH trials (Figure 14 and Figure 15) to evaluate the sensor's ability to monitor extracellular pH as a function of the measured fluorescence intensity (Figure 16). Both data sets were normalized at pH 7.4. The normalized sensitivity attained by the sensors was 0.44 per pH unit. For the dynamic system in Figure 14, the normalized standard deviation was 0.002, leading to a resolution, defined as the smallest change in pH discernible from the fluorescence intensity data, of 0.014 pH unit. For the static system in Figure 15, the normalized standard deviation was 0.0143, leading to a resolution of better than 0.1 pH unit. The decreased resolution of this system compared with the dynamic system is primarily attributed to electronic noise of the fluorimeter rather than to poor performance of the sensors since, for a sample of glycylglycine-FITC conjugate, the normalized standard deviation of the fluorimeter is 0.0149. The fluorescence intensity of the resealed ghosts shows a linear dependence between approximately pH 6.5 and 7.4. At higher pH values, the response becomes nonlinear, as expected for a dye with pK of approximately 6.4. From these data, the pKs for the two resealed ghost sets were determined to be 6.65 and 6.59. These values vary slightly from the experimental pK of glycylglycine-FITC conjugate (pK 6.37), indicating that slight effects of the resealed ghost's cytosolic environment may exist. However, the resealed ghosts clearly track changes in extracellular pH over the physiological range.
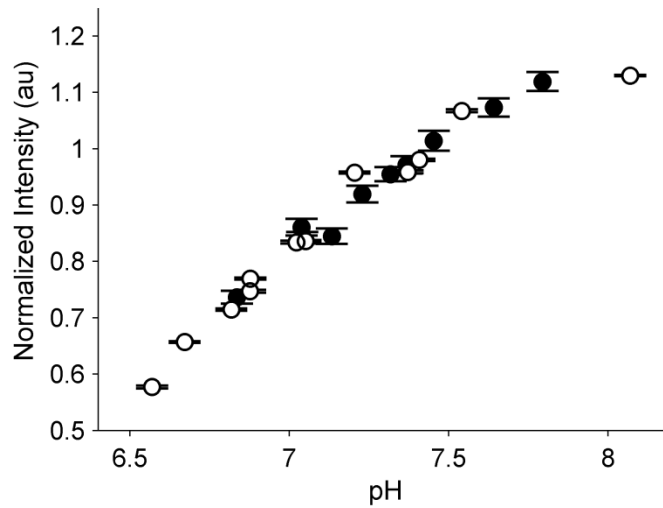
Figure 16. Normalized fluorescence intensity as a function of pH for the pH trials shown above in Figure 14 (○) and Figure 15 (●). The two trials agree well. Error bars represent one standard deviation.

The distribution of glycylglycine-FITC conjugate among the resealed ghosts was investigated through epifluorescence (λex = 488 nm, 60x objective) and bright-field phase microscopy (60x objective), as shown in Figure 17. Comparison of same field images of resealed ghosts taken with each of these techniques indicates that approximately 50% of the resealed ghosts contained the fluorescent dye (unloaded RBCs are not observable in the fluorescent micrograph). This observation matches well with observations of Bodemann *et al.* indicating that approximately 60% of ghosts made at 0 °C reseal upon warming to 37 °C [133]. Across batches, entrapment efficiency, defined as the ratio of loaded, resealed ghosts to total RBCs, ranged from 30 – 80%. Although complete loading is ideal, it is not necessary for success of the sensor because (1) the fluorescence signal is an integration of all resealed ghosts within the excitation volume and (2) unloaded RBCs do not contribute to the background signal. The final sensor

53

design will include a reference fluorophore to account for variations in loading between batches, as well as in excitation and detection efficiencies.

(a)   (b)
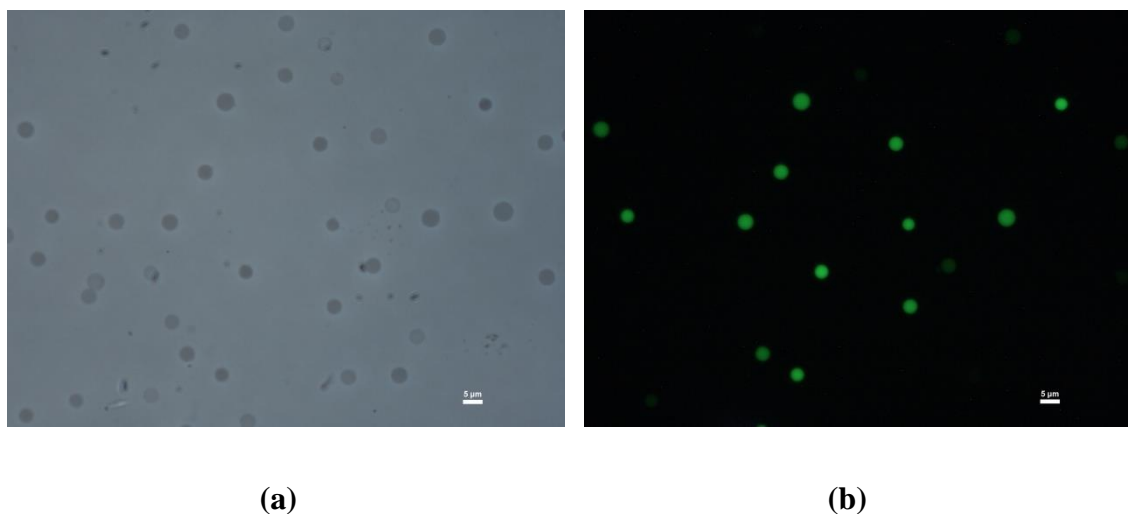
Figure 17. Representative (a) bright-field phase and (b) epifluorescence micrographs of resealed ghosts loaded with glycylglycine-FITC conjugate. (Scale bar represents 5 μm.)

Resealed ghosts loaded with glycylglycine-FITC conjugate were injected into a rat while monitoring the signal with a bifurcated reflectance probe. As shown in Figure 18, each injection (noted with an arrow) resulted in a measurable increase in signal. For the 500 μL and 900 μL bolus injections of loaded ghosts, the fluorescence increased by 0.72% and 1.03%, respectively. These measureable increases in signal were small, likely resulting from a host of reasons, the most significant of which are a suboptimal optical system as well as the considerable absorption and scattering of FITC fluorescence by tissue. Methods to circumvent these problems will be discussed in the next section.
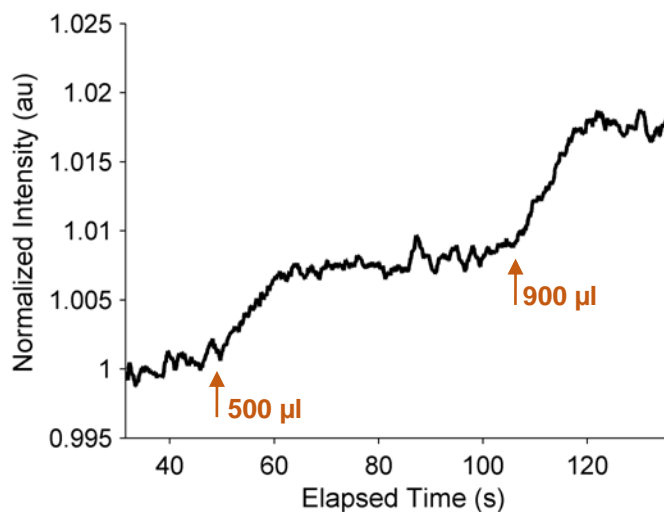
Figure 18. Change in integrated signal upon injection of resealed ghosts loaded with glycylglycine-FITC conjugate into rat. Injections of 500 µL and 900 µL result in signal increases of 0.72% and 1.03%, respectively.

3.4 Conclusions

RBCs offer a unique system for entrapping fluorescence-based sensing assays that protects the sensor from the damaging effects (*e.g.*, biofouling) of the immune system. Furthermore, since normal RBCs live for 120 days, the red cell sensors have the potential to function for multiple months, significantly improving on current monitoring systems. In this work, we have shown that dye-loaded, resealed ghosts track changes in extracellular pH. Fluorescence intensity changes in response to pH were reversible, and the resealed ghost membranes were stable over the experimental time period. While it was shown that not all RBCs load during the procedure, complete loading, although a long-term goal, is not a requisite for success of this sensing system.

This platform technology offers the potential for a long-term, minimally-invasive method for monitoring blood analytes. Although the current system focuses on

55

monitoring pH, the pH-sensitive dye could be replaced with a dye that is sensitive to a different analyte of interest, such as glucose. Since human RBCs rapidly transport glucose across the membrane, we expect that intracellular levels would track extracellular levels, similarly to the pH work shown here. As highlighted by the results of preliminary *in vivo* work, there remains a need to design and optimize a RBC-based sensing system that is suitable for *in vivo* application. Aside from the development of a more sensitive optical system, areas for improvement include: (1) preparation of ghosts with near-normal Hb levels, thereby providing complete functionality *in vivo*; (2) incorporation of NIR dyes, where scattering and absorption of tissue/Hb are less significant, thereby increasing the excitation signal to the dye and emission signal to the detector, and (3) optimization of loading parameters to maximize loading homogeneity and efficiency, thereby maximizing the signal from the loaded ghosts.

4. APPLICATION OF PH-SENSITIVE NIR DYES TOWARDS THE APPLICATION OF *IN VIVO* BLOOD ANALYTE SENSING

4.1 Background

4.1.1 Benefits of the NIR Region for In Vivo Systems – Biological Basis

Shifting to the NIR region of the electromagnetic spectrum offers a number of unique advantages for *in vivo* spectroscopy. Fluorescence of endogenous molecules within tissue is dominant in the UV and visible range. Examples of major intracellular fluorophores (with excitation / emission wavelengths) in tissue include NADH (340 nm / 460 nm), flavins (*e.g.*, FAD; 450 nm / 525 nm), and aromatic amino acids (deep UV) [134]. The two major fluorophores in the extracellular matrix are the structural proteins elastin (340-370 nm / 400-450 nm) and collagen (280-300 nm / 350-400 nm) [1, 135]. The so-called tissue optical window [136], where absorption of biological tissue is low, is bound on the lower end by hemoglobin (both oxy- and deoxyhemoglobin) absorption and on the higher end by water absorption. As such, the wavelength range between approximately 650 and 950 nm, where light is able to penetrate several centimeters into tissue, is ideal for *in vivo* spectroscopy [137]. Within this wavelength region, tissue scattering dominates over absorption, with cell organelles such as nuclei and mitochondria serving as the main contributors [138]. Mie scatterers within tissue result in a scattering coefficient exhibiting little dependence on wavelength (*i.e.*, $\lambda^{-0.22}$) between 600 and 2000 nm. However, the contribution of Rayleigh scattering resulting from collagen and elastin fibrils decreases as λ^{-4}, resulting in an overall reduction in the total

57

reduced scattering coefficient (*i.e.*, combined Rayleigh and Mie scattering) with increasing wavelength. The result of lower absorption and scattering in the NIR region is an increase in the optical penetration depth within the tissue [139].

4.1.2 Benefits of the NIR Region for In Vivo Systems – Optical System Components

Aside from the role of tissue optical properties in the selection of fluorophore(s) for *in vivo* applications, advances in NIR technology have led to inexpensive and easily-accessible optical equipment designed for use in the NIR, further easing the development of an optical system for interrogation of the NIR dye-loaded RBCs. Due to monetary constraints, a steady-state optical system was built to collect *in vivo* data for the NIR dye. Aside from relatively inexpensive optical components, other benefits of steady-state fluorescence include simplicity and small size of instrumentation leading to portability. However, in future iterations, it may be beneficial to move to a fluorescence lifetime-based approach, which has the significant advantage of allowing the user to efficiently separate the fluorescence from the background signal and providing an absolute measurement.

4.2 Materials and Methods

4.2.1 Preswelling Method for Loading Glycylglycine-FITC Conjugate into RBCs

RBCs were prepared for loading by washing whole bovine blood three times with 165 mM NaCl. The preswelling technique applied to loading glycylglycine-FITC conjugate is based on protocols of Tajerzadeh *et al.* and Pitt *et al.* [140, 141]. Eutonic K+-reversed Hank's balanced salt solution (HBSS) was prepared as follows: 136.55 mM KCl, 0.73 mM KH_2PO_4, 15.15 mM $NaHCO_3$, 5.41 mM NaCl, 0.56 mM Na_2HPO_4, and

11.10 mM glucose. To preswell the RBCs, 2 mL of 0.67x eutonic HBSS were added to

0.5 mL of cleaned RBCs; the sample was gently mixed and centrifuged at 2200 g for 3

min. The supernatant was discarded and 100 µL of hemolysate (equal volumes of RBCs

and DI water to lyse the cells and provide extra intracellular components) was layered on

top of the RBCs, followed by 100 µL volumes of glycylglycine-FITC conjugate. The

RBCs were gently mixed and centrifuged following each addition of dye. Dye solution

was added until the point of lysis, which is observed as a darkening of the supernatant

and a loss of the distinction of the pellet layer. Osmolarity is restored and ghosts resealed

by addition of 75-100 µL of 10x eutonic HBSS; resealed ghosts regain their bright red

color. The resealed, loaded ghosts were annealed in a water bath at 37 °C for 30 min. To

remove free glycylglycine-FITC conjugate, compromised membranes, and cytosolic

components (*e.g.*, hemoglobin), the resealed ghosts were washed 3-4 times with 165 mM

NaCl. Unused ghosts were stored in PBS at 4 °C until use.

For spectroscopic analysis, a 50 µL aliquot of the packed, loaded ghosts was

thoroughly mixed with 2 mL of PBS in a cuvette. The dye was excited by a frequency-

doubled Ti:sapphire laser (Mira 900, tunable from approximately 700 – 950 nm,

Coherent) at 440 nm. Fluorescence emission from the sample was collected at 90° with a

CCD camera-coupled spectrometer (Princeton Instruments, Acton 2300i) operated at a

fixed temperature of -75 °C to minimize dark noise.

4.2.2 NIR-Based Benchtop Spectroscopy System

For spectroscopic measurements, either a tunable Ti:sapphire laser (Mira 900,

tunable from approximately 700 – 950 nm, Coherent) or a laser diode (785 nm, 80 mW,

M5-785-0080; 670 nm, 15 mW, HL6756MG; Thorlabs) was used as an excitation

source for the NIR dyes in solution. Laser power was adjusted to 1 mW or less prior to

the sample. Fluorescence emission from the sample was collected in the same manner

described above. Scattered excitation light was removed through the use of a long-pass

filter (Semrock, FF01-800/LP-25, 800 nm BrightLine LWP Edge Filter, 25 mm), which

passed greater than 94% of light between 814 nm and 950 nm and less than 0.000014%

at the appropriate laser wavelengths.

4.2.3 NIR-Based Portable Optical System

To improve the accessibility of this optical system, a fiber optic probe-based

portable optical system (Figure 19) was designed and built in-house. The final iteration

consisted of a laser diode (785 nm, 80 mW, M5-785-0080; 670 nm, 15 mW, HL6756M;

Thorlabs), trifurcated fiber probe (FCR-19IR200-2-ME, 200 µm cores, 0.22 NA,

Avantes), and a pair of amplified silicon photodetectors (PDF10A, Thorlabs). These

detectors exhibit high responsivity across the wavelength range of the NIR signal (*i.e.*,

800 – 950 nm), with peak responsivity at 960 nm. The laser diode, mounted in a TE-

cooled mount (LDM21, Thorlabs), was coupled into the excitation end (*i.e.*, 17

excitation fibers around 2 collection fibers) of a trifurcated fiber probe through the use of

a mounted aspheric pair (C230260P-B, Thorlabs), which has a high NA (*i.e.*, 0.55) lens

to collect the highly divergent light from the laser diode coupled with a low NA (*i.e.*,

0.16) lens to couple the light into the fiber probe. Laser diode current and temperature

were regulated *via* a laser diode driver (Model 505, 0 – 200 mA range, Newport) and

benchtop temperature controller (TED200C, Thorlabs). Laser power at the output of the

fiber probe, measured with a digital optical power meter (PM100, console; S120UV, standard power sensor; Thorlabs), was controlled by changing the current to the laser diode and altering the coupling of the laser diode into the fiber probe. Power levels at the sample were typically maintained below 600 µW.
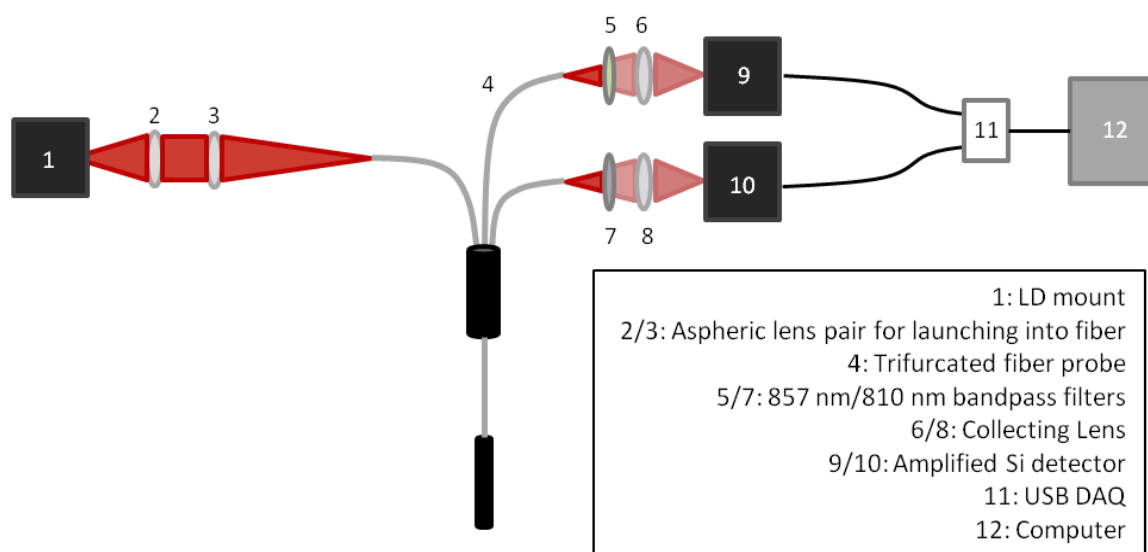
Figure 19. Cartoon illustrating the basic setup of the portable optical system (figure not drawn to scale).

Dye fluorescence was focused into each of two detectors by a second mounted aspheric lens (Thorlabs, 7.5 mm FL, A375TM-B). For ratiometric measurements, bandpass filters maximizing the percent change across the physiological pH range, determined *via* spectroscopic measurements, were employed prior to the collection lens. The optimal bandpass filter set was an 857 nm / 30 nm FWHM filter (Semrock, FF01-857/30-25, BrightLine® single-band bandpass filter, 25 mm) and a 810 nm / 10 nm

FWHM filter (FBH810-10, 25 mm, Thorlabs). All filters had excellent rejection- and pass-band characteristics with greater than 98% transmission at the specified center wavelength and less than 0.0000363% transmission across the blocking regions important for the selected laser diodes. To maximize collected fluorescence, the 800 nm longpass filter used in the spectroscopy system discussed above was substituted for one of the bandpass filters.

The output of each of the detectors was connected *via* BNC cable to a USB data acquisition system (USB-6009, 10 V maximum voltage, National Instruments). Voltage data from both channels were collected and visualized through a customized LabVIEW program (LabVIEW 2012, National Instruments). Raw data was written to a text file for subsequent off-line data analysis in MATLAB. A stand-alone application was built from the LabVIEW project for use on computers without LabVIEW software.

4.2.4 In Vivo Experiments

All animal experiments were carried out at the University of Missouri following IACUC approval. Sprague-Dawley rats were administered isoflurane in conjunction with oxygen, which served as the anesthetic throughout the procedure. Catheters were placed in the jugular vein for injection of the dye-loaded ghosts or free dye and the carotid artery for removal of blood samples. Hair in the vicinity of the optical probe location was completely removed through shaving and subsequent application of Nair. The optical probe was then secured in the proper location – in contact with the thigh tissue – for data collection throughout the experiment. Excitation power at the end of the optical

probe was kept at approximately 500 µW, and experiments were conducted for a maximum of three hours.

4.3 Results and Discussion

4.3.1 Iteration 1, pH-Sensitive NIR Dye

Due to the myriad benefits of the NIR spectral range for *in vivo* applications, a pH-sensitive NIR dye based upon a cyanine dye was developed for incorporation into RBCs. The chemical structure of the first synthesized NIR dye, hereby termed *NIR dye I*, is shown in Figure 20. Cyanine dyes are characterized by a pair of nitrogen atoms separated by a polymethine chain, the length of which alters spectral properties [142]. By increasing the length of the polymethine chain, the absorption and emission of the dye can be extended into the NIR region. The nitrogen atoms are typically incorporated within heterocyclic aromatic rings, as demonstrated in the structure of *NIR dye I*. *NIR dye I* at 0.41 µM displayed excellent pH sensitivity as free dye in a 2:1 solution of 165 mM NaCl:PBS. As shown in Figure 21, the dye spectra display both intensity changes and spectral shifts as a function of pH. For low pH values, the higher energy peak at 830 nm dominates with little to no contribution from the lower energy peak at 880 nm. As pH increases, the 880 nm peak increases as the 830 nm peak decreases. The ratio of the intensities at 830 nm and 880 nm as a function of pH results in a calibration curve (Figure 21c) with a 67.17% change in signal over the range of pH 6.5 to 7.3. Although the absorption and emission properties of *NIR dye I* were optimal for *in vivo* applications, the dye had a significant drawback – a predisposition for self-association leading to aggregation. Both visual affirmation of dye inhomogeneity in

solution and spectral effects served as manifestations of *NIR dye I* aggregation, a

common problem associated with cyanine-based dyes.
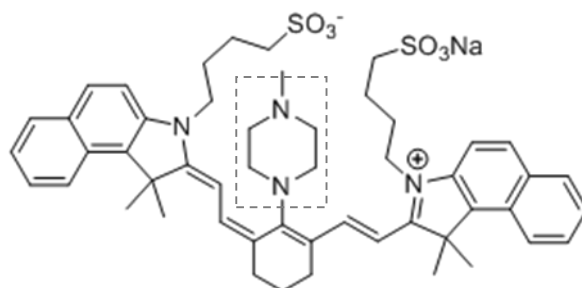
Figure 20. Chemical structure of *NIR dye I* developed for the *in vivo* realization of the dye-loaded RBC concept. pH sensitivity of the molecule is imparted by the methylpiperazine (indicated with green dashed line).
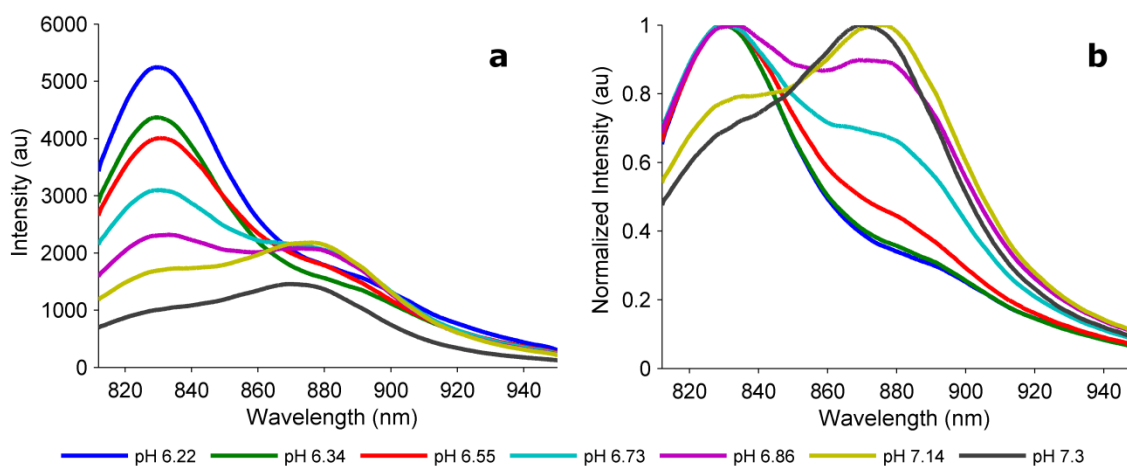
Figure 21. (a) Raw and (b) normalized spectra of free *NIR dye I* [0.41 µm] in a 2:1 solution of NaCl:PBS show the pH sensitivity of the dye. (c) Ratio of intensities at 830 nm and 880 nm shows a 67.17% change in signal over the physiologically-relevant pH range of 6.5 to 7.3.
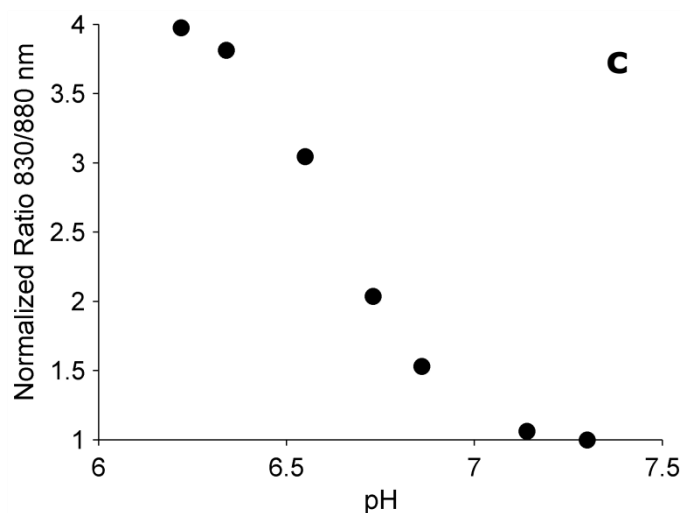
Figure 21 Continued.

Spectral characteristics of *NIR dye I* are similar to the cyanine dyes presented by Yarmoluk *et al.* [143] that had been developed for the detection of bovine serum albumin (BSA). In the presence of BSA, the spectral signal of the dye blue shifts and increases; importantly, fluorescence increased directly with BSA concentration. In this case, the tendency for aggregation and subsequent changes due to the presence of proteins were advantageous, as the changes served as indicators for protein concentration. Aggregation of these dyes in solution is caused by strong, attractive van der Waals forces between the dye molecules. Cyanine dye aggregates are known to exhibit different absorption and emission spectra than the monomeric form of the dye [7, 143-145]. For the work presented here, the emission band of dye aggregates is bathchromically shifted compared with the monomeric form of the dye. The fluorescence intensity of aggregates in solution is low and tends to increase upon exposure to proteins, the interaction of which is believed to disrupt the aggregates.

65

The protein binding characteristics of *NIR dye I* were tested *via* addition of BSA to a solution of the dye in PBS to maintain pH. For this experiment, approximately 42 µM BSA was added to approximately 8 µM *NIR dye I* with stirring under constant excitation. As shown in Figure 22a and b, a number of representative spectra were chosen from a time-course experiment. Free dye in PBS displayed a single peak with a maximum at approximately 870 nm, presumably due to the presence of dye aggregates. Immediately following BSA addition, the dye spectrum displayed the onset of a blue shift, with an addition of a blue shoulder at 3.4 min. The dual peaks likely indicate the presence of both monomer dye molecules and aggregates. Over time, the monomeric fluorescence peak (*i.e.*, the blue-shifted peak at approximately 835 nm) increased and narrowed while the aggregate peak disappeared. The integrated intensity increased approximately 11-fold due to the addition of BSA (Figure 22c).
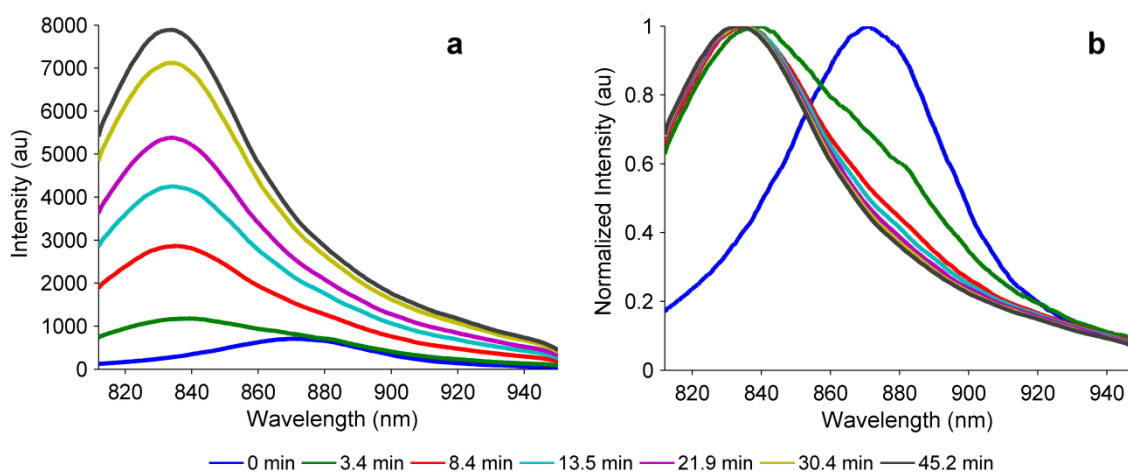
Figure 22. (a) Raw and (b) normalized spectra of *NIR dye I* display the fluorescence increase and the approximately 40 nm blue shift due to addition of 41.67 µM BSA to 8.24 µM *NIR dye I* in PBS. (c) Normalized integrated intensities show an 11-fold fluorescence increase.
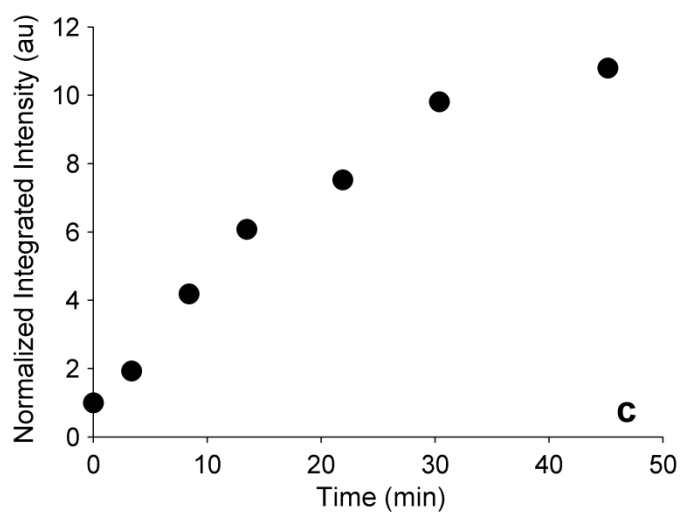
Figure 22 Continued.

Fluorescence increases were also observed when adding equivalent volumes of either membranes (*i.e.*, white membrane sacks following removal of all intracellular components *via* lysing) or Hb (Figure 23). At the 30 min mark, integrated fluorescence displayed approximately 1.3-fold and 6.3-fold increases following addition of Hb and membranes, respectively. Although the signal increase had significantly slowed when the experiment was stopped at 30 min, data collection following an additional 30 min of incubation time showed that the signal saturated the detector at 10.46 V, indicating that the signal continued to increase at a slow rate.
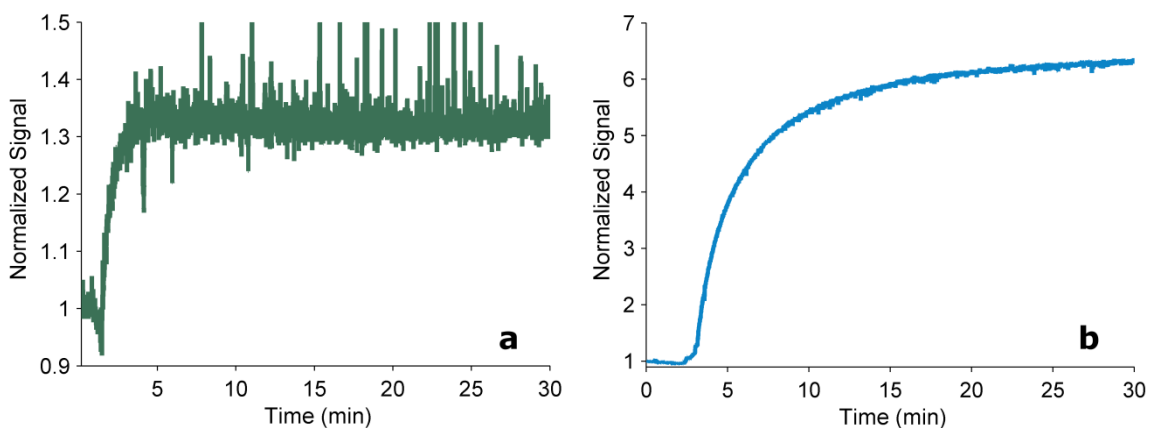
Figure 23. Change in *NIR dye I* [24.7 μM] fluorescence signal upon addition of (a) Hb and (b) membranes.

As one would expect the dye to interact with Hb once introduced into the RBCs *via* the loading procedure, the pH sensitivity of the *NIR dye I*:Hb complex was investigated similarly to that of the free dye. *NIR dye I* and Hb were allowed to incubate overnight to fully allow for the interaction to occur and reach steady state. As such, changes during the experiment should be due to changes in local pH rather than due to introduction of protein and disruption of aggregates. As expected from prior results with BSA, significant spectral changes were observed for the case of the *NIR dye I*:Hb complex (*e.g.*, significant reduction in the longer wavelength peak). However, as shown in Figure 24, there are muted changes in both intensity and spectral shape as a function of pH. Although the calibration curve shows a pH-dependent trend (Figure 24c), the reduced pH-dependent changes in the longer wavelength peak negatively affect the pH sensitivity in that the total change in the normalized ratio between wavelengths 830 nm and 880 nm is approximately 21% across the range of pH 6.5 to 7.2. Due to significant

aggregation effects, dye loading within RBCs was unsuccessful, as the loaded cells

could not be verifiably separated from aggregated dye.
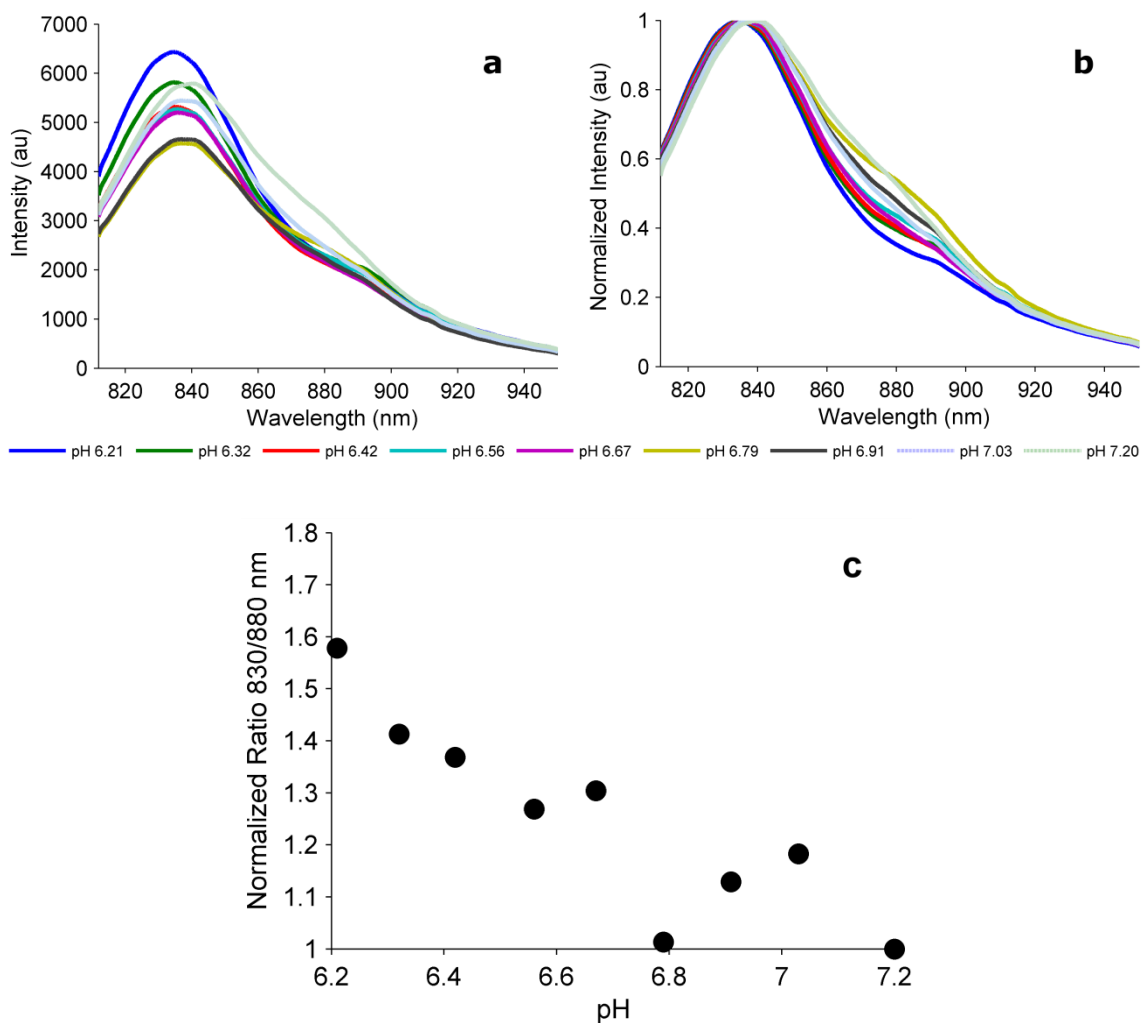
Figure 24. (a) Raw and (b) normalized spectra of the *NIR dye I:*Hb complex in a 2:1 solution of NaCl:PBS show the pH sensitivity of the dye. (c) Ratio of intensities at 830 nm and 880 nm shows a 21% change in signal between the physiologically-relevant range of pH 6.5 to 7.2, a muted response compared with the pH sensitivity of free *NIR dye I.*

*NIR dye I* was shown to be solvatochromic, or sensitive to the polarity of the local environment. Upon increasing the ratio of ethanol to water (*i.e.*, decreasing polarity), measured fluorescence of *NIR dye I* at 12.3 μM increased with a concomitant shift in peak wavelength and loss of the longer wavelength peak (Figure 25). This behavior is likely due to the presence of aggregates in polar solutions (*i.e.*, water) [143]. Similar with the behavior of *NIR dye I* in the presence of proteins, the longer wavelength peak or shoulder (visible in the 0% and 20% ethanol samples) is attributable to dye aggregates, while the shorter wavelength peak represents monomeric dye. The dye demonstrated a hypsochromic shift, or blue shift, with increasing solvent polarity. The integrated intensity increased more than 100-fold from 0% to 90% EtOH. In a similar experiment, the blue color of the *NIR dye I* solution deepened significantly upon increasing ethanol concentration, as shown in Figure 26. The ethanol-to-water ratio experiment was repeated with the portable optical system. Due to the sensitivity of the detector, the fluorescence signal across a lower range of ethanol concentrations (*i.e.*, 0-25%) was collected. To ensure signal changes were in fact due to changes in fluorescence, the signals from the same ratios of ethanol to water samples without dye were also collected, which verified that the effect was in fact due to increased fluorescence. Figure 27 verifies the effect of increasing ethanol concentration on the fluorescence of *NIR dye I* at 9.3 μM that had previously been observed spectroscopically. At an ethanol concentration of 25%, the signal increased more than 32-fold over the fluorescence of *NIR dye I* in pure water (*i.e.*, 0% ethanol). These effects are consistent with those demonstrated by Berezin *et al.* [146]. Upon testing a number of

70

NIR dyes, the investigators demonstrated hypsochromic shifts of 8 – 30 nm in the

spectrum with increasing solvent polarity. Furthermore, it was shown that the dyes

exhibited higher fluorescence in methanol, ethanol, acetone, and DMSO than in water.
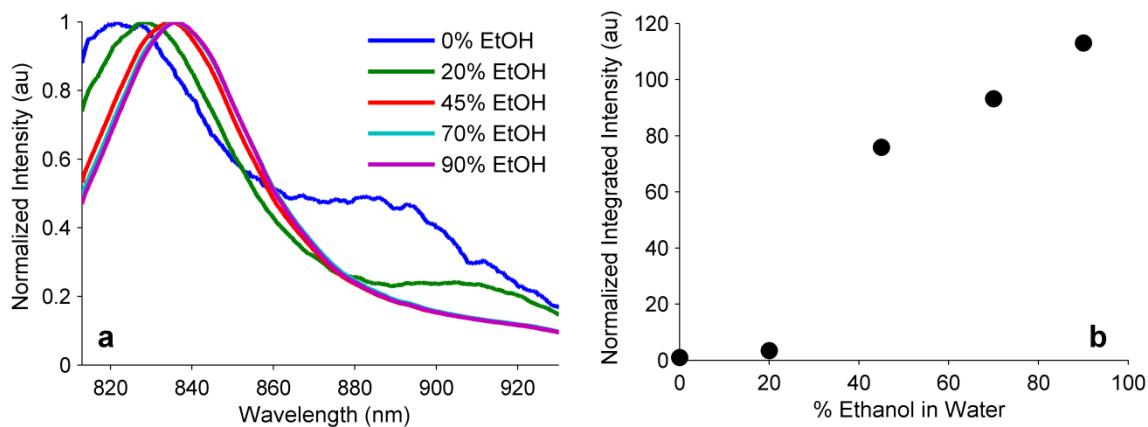
Figure 25. (a) Normalized fluorescence spectra display the shift in spectrum as a function of ethanol concentration. (b) Greater than 100-fold increase in integrated fluorescence resulting from an increased ratio of ethanol to water.
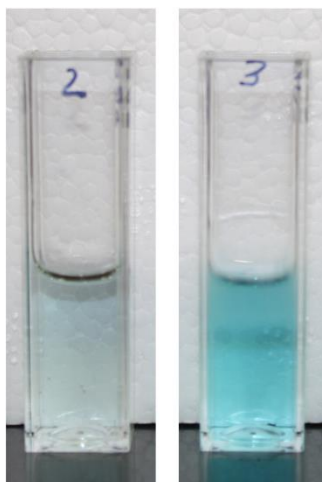
Figure 26. Deepening in color of *NIR dye I* [12.3 µM] sample is due to an increase in the ethanol to water ratio (*i.e.*, samples 2 and 3 represent 0% and 50% ethanol).

71
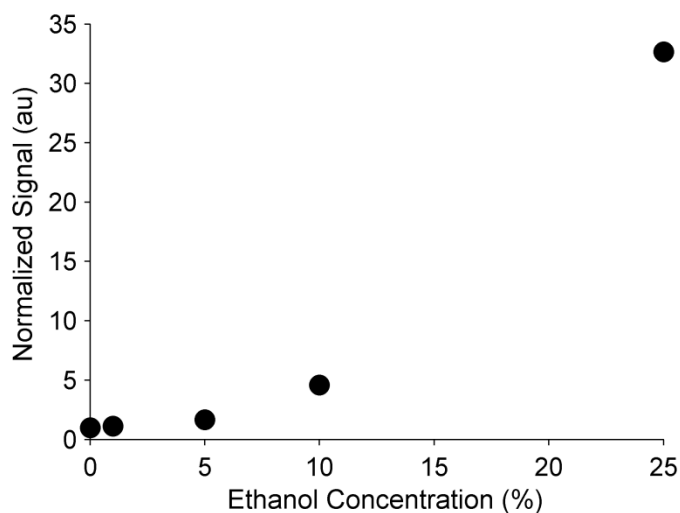
Figure 27. Increasing ethanol concentration results in a greater than 32-fold increase in *NIR dye I* [9.34 µM] fluorescence.

4.3.2 Iteration 2, pH-Sensitive NIR Dye

To circumvent the problems associated with *NIR dye I*, a second pH-sensitive

NIR dye, hereby termed *NIR dye II*, was synthesized. *NIR dye II* (Figure 28) is based on

a poly-sulfonated IR-820, which was appended with a methyl piperazine (indicated with

green dashed line) – the pH sensitive portion of the molecule. The presence of the

sulfonate groups discourages stacking of the aromatic rings, decreasing the propensity of

NIR dye II to aggregate in solution. As expected, *NIR dye II* was more stable than *NIR*

dye I; for example, *NIR dye II* remained suspended in buffer. An absorption spectrum of

NIR dye II is shown in Figure 29.
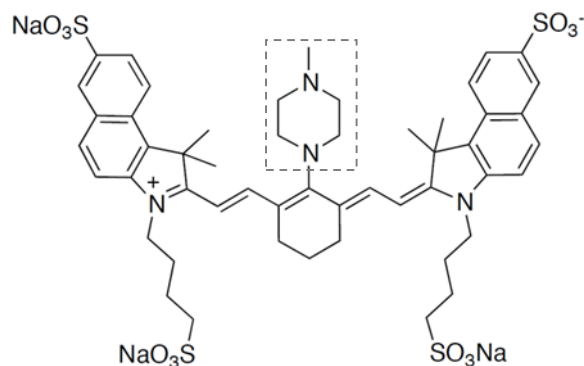
Figure 28. Chemical structure of *NIR dye II* highlights the addition of sulfonate groups compared with *NIR dye I* to reduce dye aggregation.
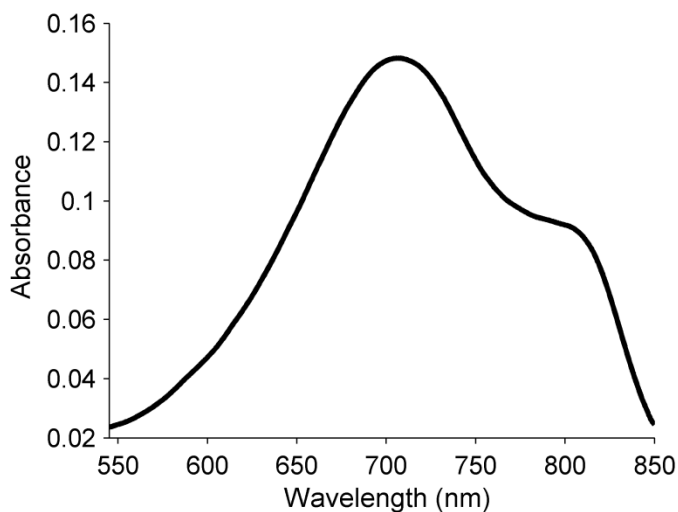
Figure 29. Absorbance spectrum of *NIR dye II* [5 µM] in PBS.

The pH sensitivity of *NIR dye II* was assessed with both the bench-top spectroscopy system and portable fiber-based system at two excitation wavelengths: (1) results from 670 nm excitation are shown in Figure 30 and Figure 32a; (2) results from 785 nm excitation are shown in Figure 31 and Figure 32b. All samples consisted of dye diluted in PBS; pH adjustments were made with 1-2 µL aliquots of 100 mM NaOH and

HCl. When excited at 670 nm (within the shorter-wavelength peak of the absorbance spectrum, Figure 29), there is a slight blue shift of the fluorescence peak at approximately 830 nm and an increase in fluorescence of *NIR dye II* at 2 µM as the pH of the local environment is increased. When excited at 785 nm (within the longer-wavelength shoulder of the absorbance spectrum, Figure 29), *NIR dye II* at 2.2 µM displays a slight blue shift with increasing pH similar to the shift exhibited upon 670 nm excitation. However, 785 nm excitation results in a decrease in the fluorescence peak upon increasing pH, counter to that shown for 670 nm excitation. The change in pH sensitivity based upon excitation wavelength results from the pH sensitivity of the dye absorbance. Upon increasing the pH of the sample, absorbance increases for the shorter-wavelength peak and decreases for the longer-wavelength shoulder.
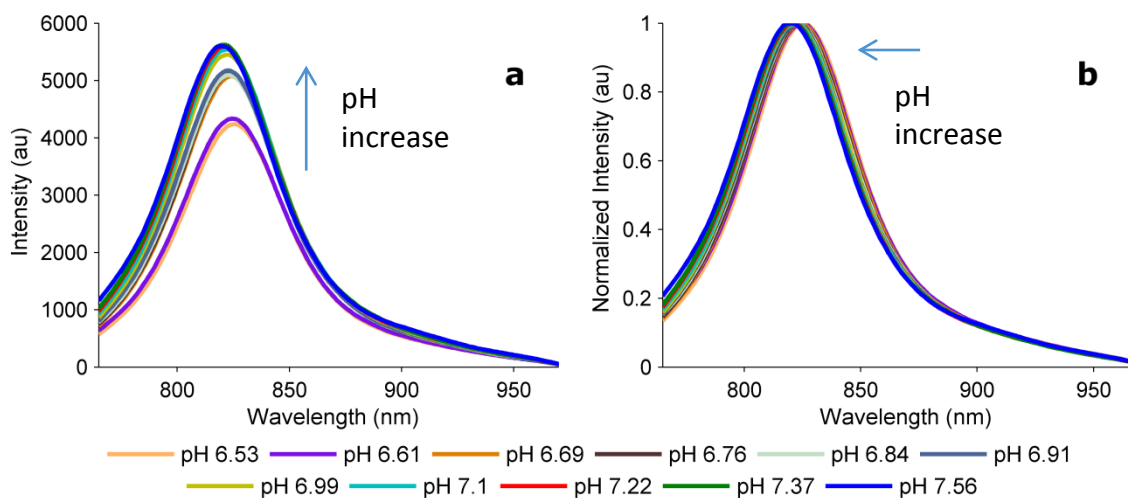
Figure 30. pH sensitivity of 2 µM *NIR dye II* in PBS as measured with a 670 nm excitation source and bench-top spectroscopy system. Representative (a) raw and (b) normalized spectra as a function of pH.

Figure 31. pH sensitivity of 2.2 μM *NIR dye II* in PBS as measured with a 785 nm excitation source and bench-top spectroscopy system. (a) Raw and (b) normalized spectra as a function of pH.

For data analysis and comparison with the portable system, the spectral bands corresponding to the selected filters of the portable system were used for a ratiometric measurement of pH changes. In this case, the bands were a 10 nm FWHM bandpass filter at 810 nm and a 30 nm FWHM bandpass filter at 857 nm. The ratios of the two bands at different pH levels were used to develop calibration curves for each excitation wavelength. As shown in Figure 32, the dye exhibits increases of 16.34% and 29.42% for 670 nm and 785 nm excitation, respectively, across the physiologically-relevant range of approximately pH 6.85 to 7.5.
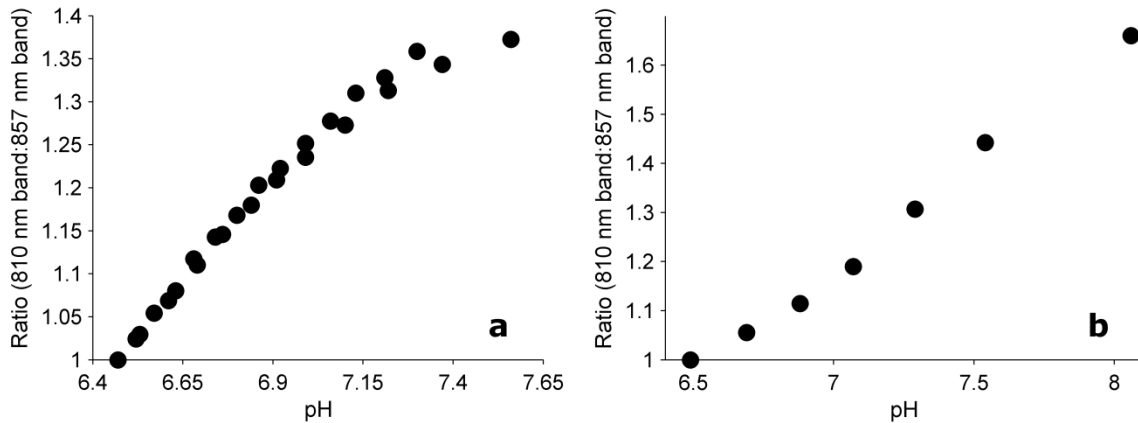
Figure 32. Calibration curves for (a) 670 nm excitation and (b) 785 nm excitation show increases in the ratio of 16.34% and 29.42% across pH 6.85 to 7.5, respectively.

For analysis with the portable system, pH measurements and voltage measurements corresponding to both bands were collected simultaneously. As shown by the time-course data in Figure 33b and Figure 34b, pH and the ratio of the two spectral bands track well. When the ratio is plotted as a function of pH, the resulting calibration curves (Figure 33a and Figure 34a) for the two excitation wavelengths strongly resemble those obtained using spectroscopic measurements (Figure 32). The calibration curves show increases of 14.86% and 31.67% between pH 6.85 and 7.5 for 670 nm and 785 nm excitations, respectively. Although a strong pH-dependent trend is present, the total change in signal over the physiologically-relevant range (*i.e.*, pH 6.85 to 7.5) is small – less than approximately 30% for both excitations. Thus, small pH changes achievable *in vivo* by CO_2 inhalation (decrease pH) or sodium bicarbonate injection (increase pH) may be undetectable with *NIR dye II*.

76
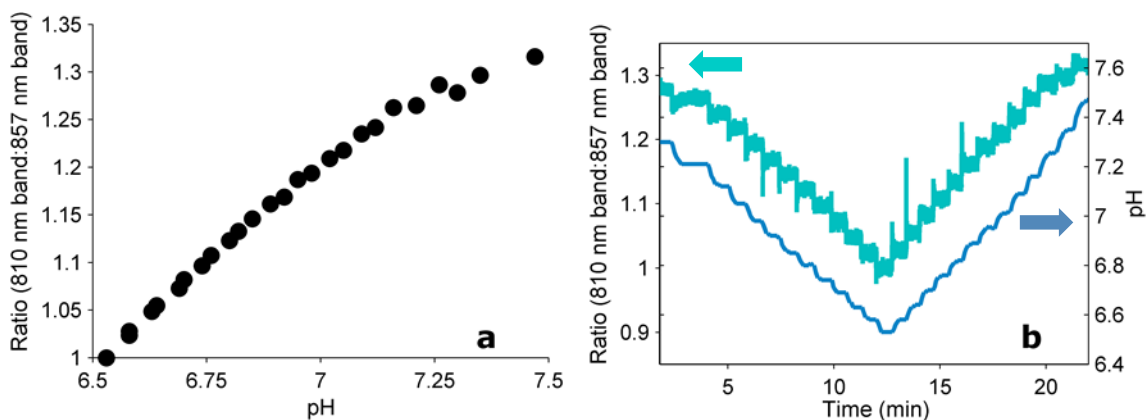
Figure 33. pH sensitivity of 2 µM *NIR dye II* in PBS as measured with a 670 nm excitation source and portable, fiber-based optical system. (a) Calibration curve shows an increase in the ratio of 14.86% across approximately pH 6.85 to 7.5. (b) Time-course measurements of pH and ratio show that the two variables track each other well.
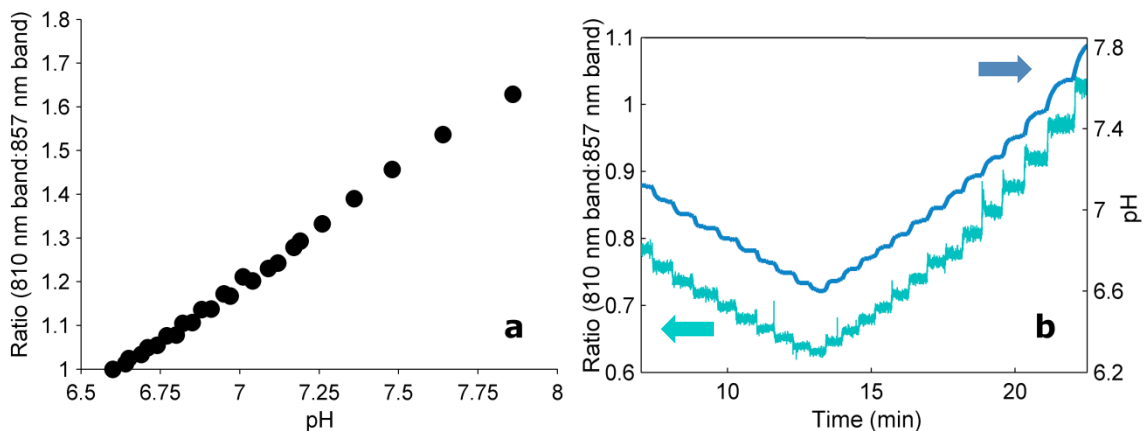
Figure 34. pH sensitivity of 2 µM NIR dye II in PBS as measured with a 785 nm excitation source and portable, fiber-based optical system. (a) Calibration curve shows an increase in the ratio of 31.67% across pH 6.85 to 7.5. (b) Time-course measurements of pH and ratio show that the two variables track each other well.

Aside from the measured spectral changes, the color of *NIR dye II* sample

changes as a function of pH, as easily seen for a representative high concentration

sample (Figure 35). At high pH levels, the sample has a strong blue hue (Figure 35a), which is lost upon lowering the pH (Figure 35b).
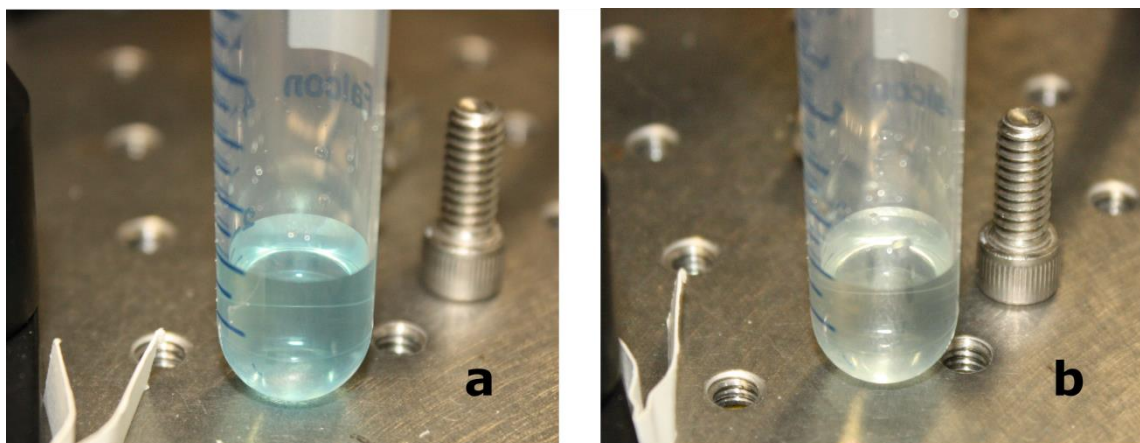
Figure 35. The effect of pH on *NIR dye II* can be observed *via* the difference in color of a 20 μM *NIR dye II* sample at (a) high and (b) low pH levels.

To test the pH sensitivity of *NIR dye II* in an environment closer to that expected in the *in vivo* realization of the system, the dye was loaded into bovine RBCs with a final lysis solution concentration of 20 μM free dye using the method described previously. Spectral measurements (785 nm excitation) were recorded as pH of the local environment was adjusted from pH 8 to 6.46. As shown in Figure 36, the dye fluorescence exhibits a slight blue shift and decrease as the pH increases. The ratio of the 810 nm band to 857 nm band shows a similar shape to that of the free dye in PBS. However, over the physiological range of pH 6.82 to 7.51, the dye-loaded cells show an increase in ratio of only 13.24%, a muted response compared with free dye. This difference may be due to some residual aggregation effects, as seen with the Hb binding

pH curve for *NIR dye I*. Thus, the change in signal over the physiological range is small and further verifies that it may be impossible to detect in the more complicated *in vivo* environment.

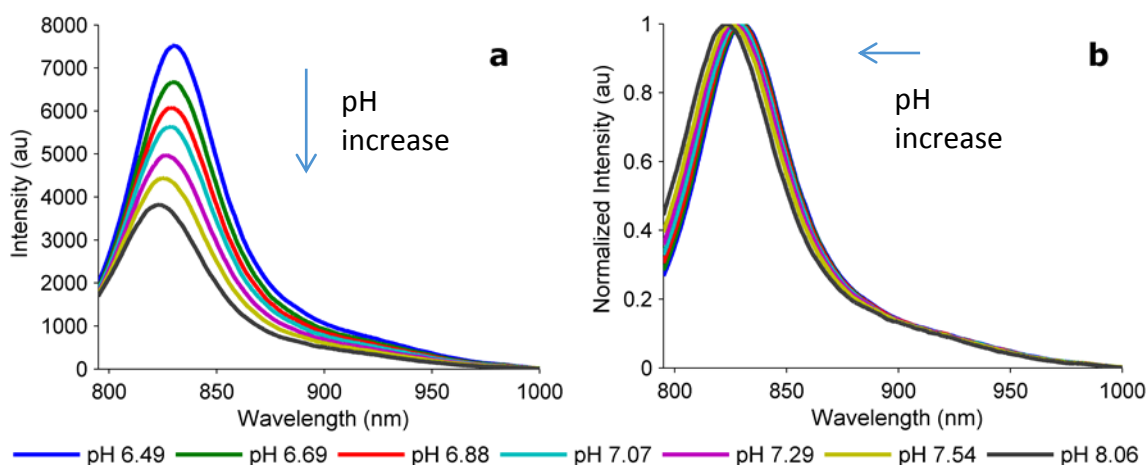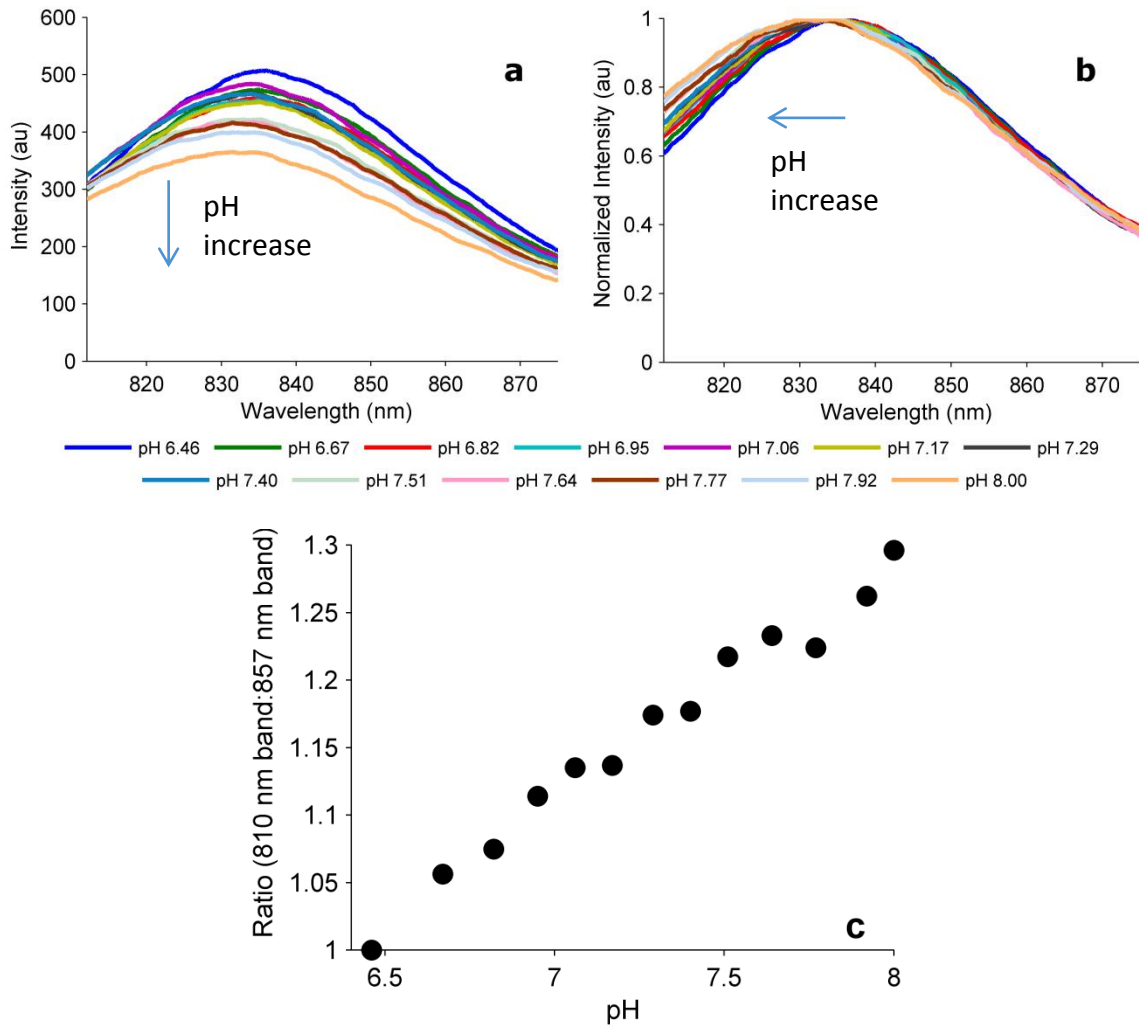**Figure 36.** pH sensitivity of *NIR dye II*-loaded bovine cells as measured with a 785 nm excitation source and bench-top spectroscopy system. (a) Raw and (b) normalized spectra show fluorescence decrease and blue shift with increasing pH. (c) Calibration curve shows an increase in the ratio of 13.24% over the physiological range of pH 6.82 to 7.51.

4.3.3 In Vivo Implementation of NIR Dye II

As mentioned previously, the synthesized NIR dyes do not possess sufficiently high pH sensitivity for reliable *in vivo* monitoring in the current embodiment of the system. Furthermore, preliminary results using inhalation of CO_2 and injection of sodium bicarbonate did not result in any measurable changes in signal. Thus, the ability to visualize both free and loaded *NIR dye II* within an animal with the in-house built portable fiber-probe system was investigated.

A calibration curve of signal voltage as a function of dye concentration within the blood volume of the animal was produced following bolus injections of free *NIR dye II*. Bolus injections of 375, 150, 75, and 25 µL sample volumes of 400 µM dye were injected into the jugular vein of the rat while optically monitoring the vascularized leg tissue above the femoral vein. Assuming a 15 mL blood volume, these dye volumes resulted in concentrations within the vasculature between 0.67 and 10 µM. The calibration curve (Figure 37b) can be fit to a linear trendline with R^2 greater than 0.99. Combining the free dye data across five animals, a second calibration curve can be produced, as shown in Figure 38. This curve shows more variability, as expected across multiple animals, but follows a similar trend to that shown in the single-animal curve. The data follow a trendline with an R^2 value of approximately 0.95. The variability can be attributed to dye clearance and other physiological differences among the animals. As shown in Figure 37a, the measured signal begins to rapidly increase upon injection, reaching a maximum level approximately 5 min post-injection. After approximately 1 min at the peak level, the signal begins to slowly decay, likely resulting from removal of

the free dye *via* filtration of the kidneys and sequestration in the bladder. The decay

kinetics follow a custom equation — $f(x) = a \cdot exp(-b \cdot x) + c$ — with R^2 values for

the fits greater than 0.99. For three trials, the average time constant of the decay mode

for free dye was 18.51±2.40 min.
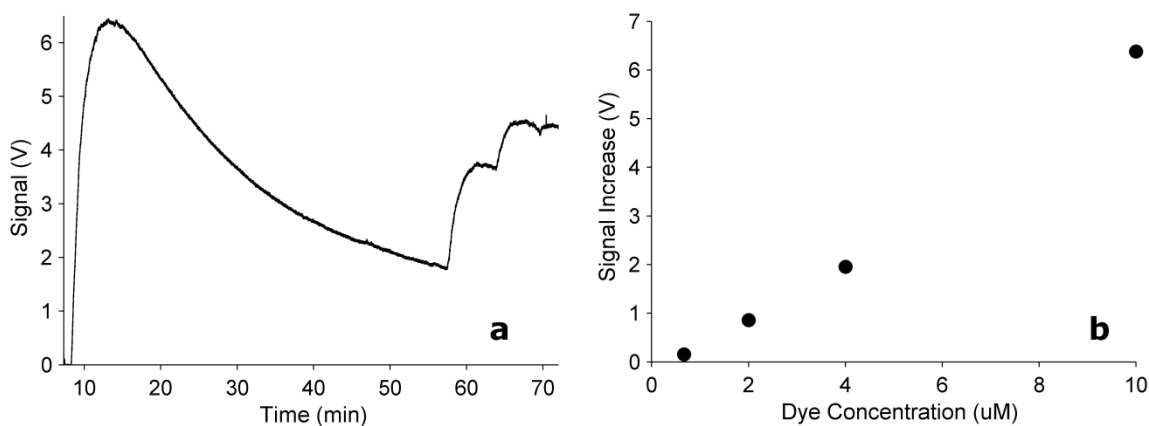
Figure 37. Bolus injections of free *NIR dye II* lead to rapid increases (approximately 5 min to peak value) in measured signal followed by a slower decrease in signal, likely due to dye removal from the bloodstream. The data can be fit with a linear trendline ($y = 0.6762x - 0.4801$) with R^2 greater than 0.99.

Using the dilution loading technique discussed previously, washed, packed horse

RBCs were loaded with 132.7 µM *NIR dye II*. Following the procedure, the loaded

ghosts were washed three times and pelleted as preparation for injection into the rat.

During this preparation, it was noted that some loaded ghost samples appeared darker

than others. In an attempt to elucidate an explanation for the discrepancies, the loaded

ghosts were centrifuged in small diameter tubes to separate different sections within the

samples.
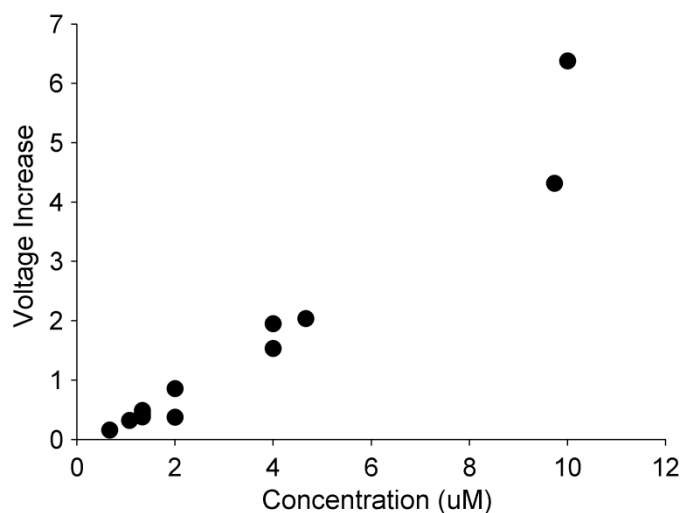
Figure 38. Voltage increase as a function of dye concentration within the blood for data taken across five different animals. The data can be fit with a linear trendline (y = 0.5749x – 0.4149) with $R^2 \approx 0.95$.

As shown in Figure 39, three types of samples were prepared using an identical loading procedure over the course of a week for *in vivo* studies. The differences observed among the prepared samples point to a significant difficulty with the current loading process. Using experience and microscopy, the different layers – between 4 and 5, depending on the sample – were identified, as shown in Figure 39c. All prepared samples had a large layer of supernatant (*i.e.*, residual Hb and free dye) and a thin, diffuse layer composed of ruptured membranes (most obvious in Figure 39c) that are no longer associated with Hb or dye (*i.e.*, they appear colorless). As shown in Figure 39c, some samples contained a dark blue layer immediately below the white layer. This dark layer, which is only present in some of the samples, is likely formed from dye aggregates that are associated with membranes or other cell components. As confirmation, cells or cell-like material were not visible in microscopy images.

82
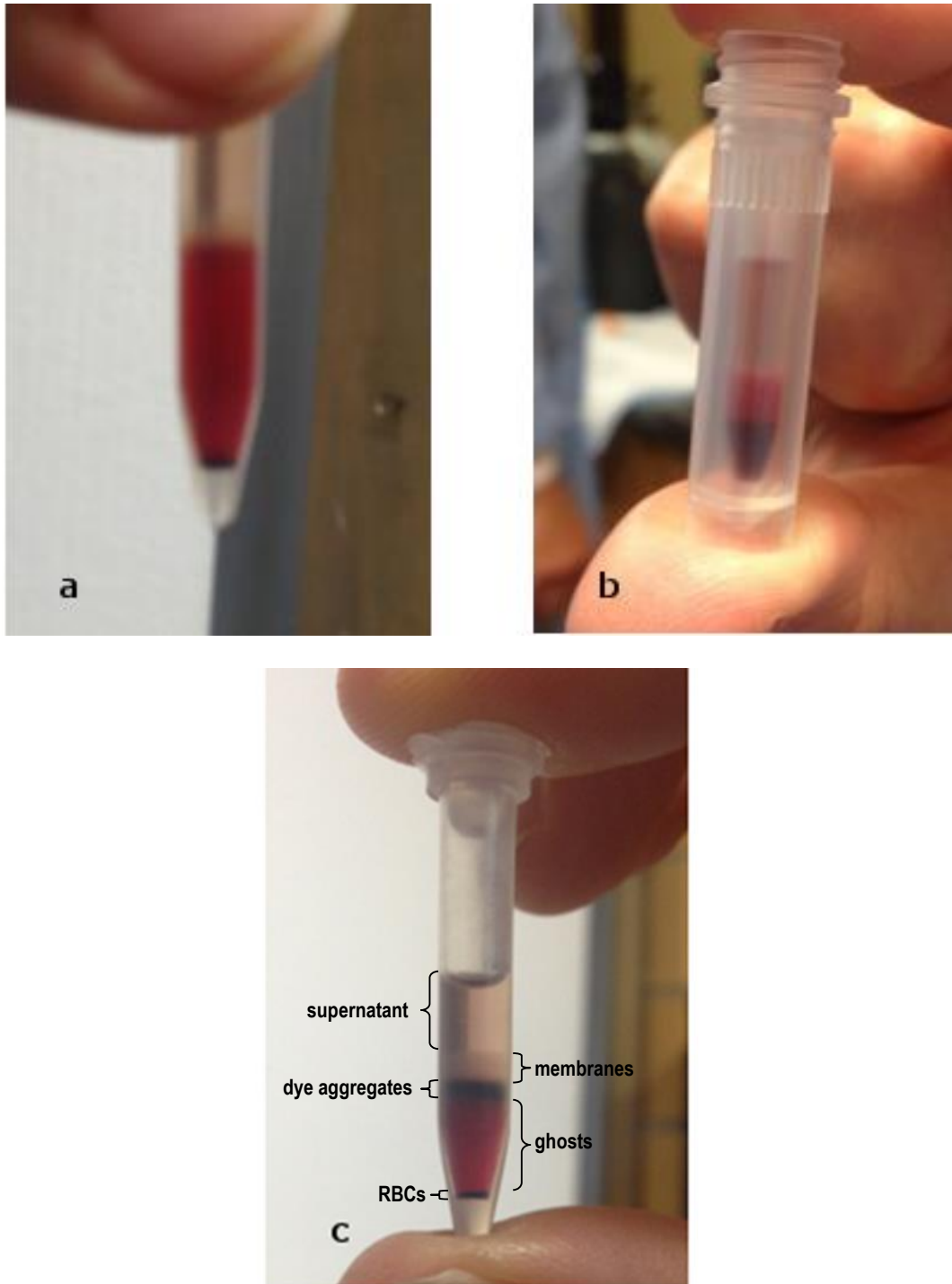
Figure 39. Examples of three different samples of *NIR dye II*-loaded ghosts obtained using an identical loading procedure. The differences observed among the samples points to problems inherent to the loading procedure. Samples shown in (a) and (b) contain 4 layers while the sample in (c) contains 5 distinct layers.

The next layer, visible in all samples, is a light red layer, which is believed to be the loaded ghosts. As expected by the procedure, these cells contain only a portion (*i.e.*, 10%) of their Hb, which results in lighter cells as compared with the control RBCs. As shown in Figure 40 and Figure 41, microscopy confirmed the presence of cells within the light red layer. Due to the long excitation wavelength required, standard fluorescence microscopes cannot excite and collect the emission from *NIR dye II*. As such, a derivative of the dye with shorter wavelength excitation and emission was loaded within horse ghosts following the same procedure. Approximately 20% of the processed ghosts were loaded with the dye derivative. Alternatively, *NIR dye II* was loaded within bovine ghosts and imaged using an inverted microscope (FV1000, Olympus America) fitted with an IR800 filter cube. Emission was coupled to a CCD camera for imaging, and data was collected with Micro-Manager Software [147]. An example overlay of bright-field and fluorescence images (Figure 41) shows that approximately 35% of the cells were loaded with dye. Out of focus fluorescence is due to loaded ghosts at other focal planes as well as moving ghosts that were not fully adhered to the cover slide.
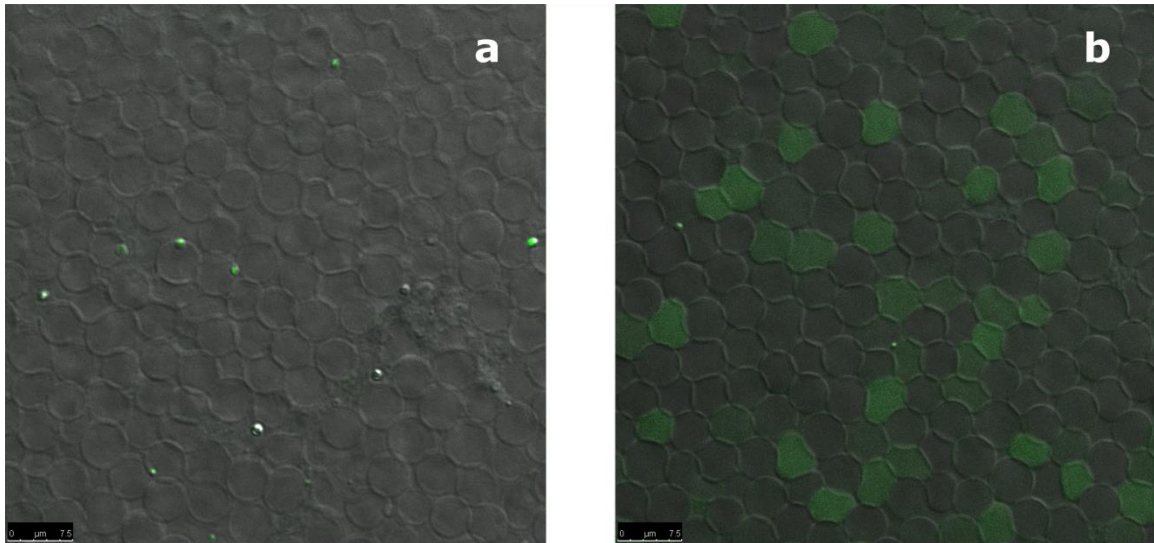
Figure 40. Overlay of DIC and fluorescence micrographs of (a) *NIR dye II*-loaded horse ghosts and (b) the shorter wavelength dye derivative-loaded horse ghosts. Use of a shorter wavelength dye allows for visualization of fluorescence from dye-loaded ghosts. Approximately 20% of the ghosts have been successfully loaded with dye.
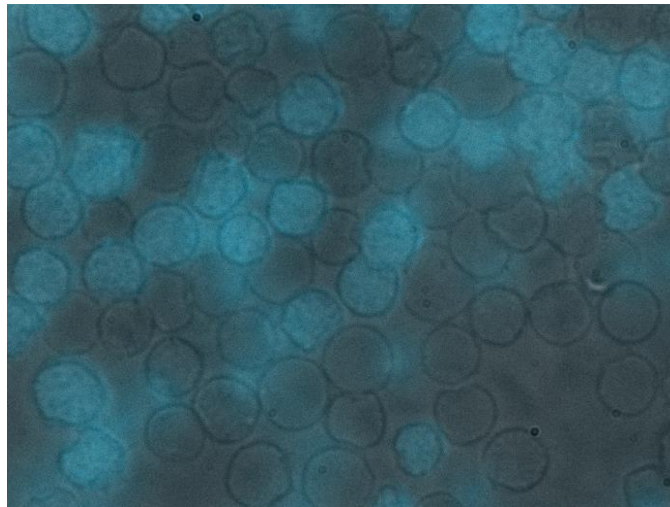
Figure 41. Overlay of bright-field and fluorescence micrographs of *NIR dye II*-loaded bovine ghosts show that approximately 35% of the ghosts were successfully loaded with dye.

The bottom layer, most significant in Figure 39b, is likely RBCs that did not lyse during the loading procedure, and therefore, these cells contain normal amounts of Hb and weigh more than the loaded ghosts, dye aggregates, and ruptured membranes. It should be noted that injection of this bottom layer as well as control horse RBCs did not result in any change of the optical signal. However, both the light red layer and dark blue layer resulted in an increase in the measured optical signal. The red region was carefully isolated from the remaining layers using a thin needle and syringe and diluted 50% with PBS in preparation for injection. Once a steady baseline signal was achieved, the red layer was injected into the jugular vein of the sedated rat. As shown in Figure 42, the measured signal increased upon injection of the sample, reaching a maximum level in less than 10 min. The signal then decreased following a curve described by the sum of a single exponential and constant (*i.e.*, the same fit as for free dye). The graphs in Figure 42a and b are sample curves obtained by injection of 200 μL and 830 μL, respectively, volumes of the light red portion of two different loaded ghost samples. For three trials using different samples, the average time constant of the decay mode for *NIR dye II-*loaded ghosts was 28.65±18.28 min. Results of the time constants from both free dye and loaded ghosts are summarized in Table 3.
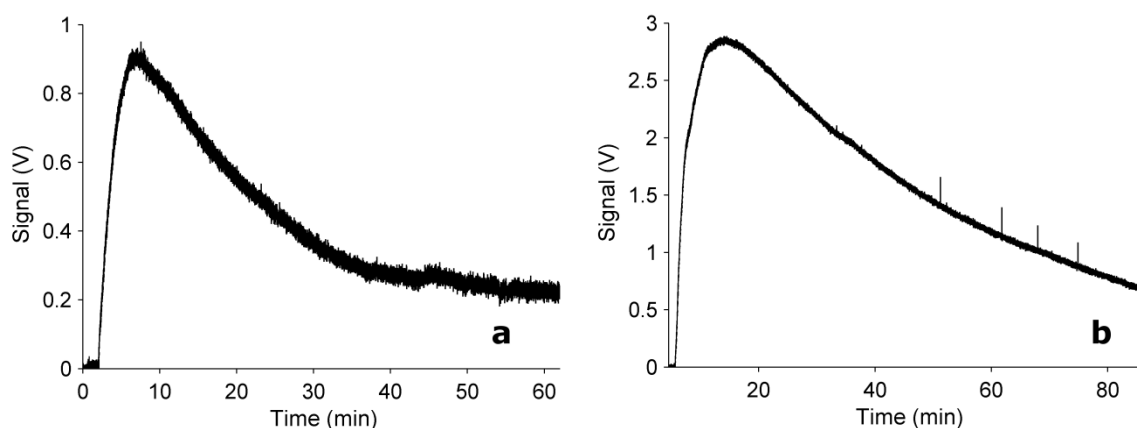
Figure 42. Bolus injections of *NIR dye II* loaded within horse RBCs using a dilution technique. (a) and (b) are representative of two different samples within different rats.

Table 3. Time constants for signal decay of free dye and dye-loaded ghosts following injection into a rat.

	Time Constant (min)		
Free dye	19.07		
	20.58	Avg:	18.51 min
	15.88	St. Dev:	2.40 min
Red Region	14.86		
	49.38	Avg:	28.65 min
	21.70	St. Dev:	18.28 min

Although there is not a statistical difference between the time constants of the free dye and loaded ghost samples, this preliminary data indicates that there may be some difference in the removal rates of the samples that may be optimized and verified upon further work. There are several theories that may explain the rapid removal of the ghost samples from the animal. First, loading horse RBCs, even unmodified, into a rat may result in unexpected problems, as horse RBCs possess different surface properties and may be rapidly removed. Baskurt *et al.* compared the aggregation tendencies of rat

87

and horse RBCs by studying their sedimentation rates [148]. Horse RBCs showed 10-fold and 18-fold increases in aggregation compared with rat RBCs at stasis and under shear stress, respectively. Rat RBCs were shown to exhibit a higher surface charge than horse RBCs. Finally, SDS-PAGE analysis showed differences in the distribution of carbohydrate-rich proteins and the absence of a band related to a particular membrane protein in horse RBCs. Lawrence *et al.* have shown that RBCs modified *via* chemical alteration of the membrane or coating with an antibody were rapidly removed from the circulatory system [149]. In normal subjects, the clearance times for chemically-modified and antibody-coated RBCs were 15.8 and 57.6 min, respectively. These times are in line with the data collected using *NIR dye II*-loaded ghosts.

A second problem that may be contributing to the signal decay may result from the procedure used to load the dye within the ghosts. It has been shown that cells that have had a majority of their Hb and other cellular components removed are rapidly removed from the body by the reticuloendothelial system [93]. As such, it may be necessary for the long-term goals of this project to load the fluorescent dye within the RBCs using a technique that maintains near-normal levels of Hb, which will likely result in longer circulation times *in vivo*. Through optimization of the procedure, it may be possible to produce loaded cells with near-normal lifespans once reintroduced [93].

Preliminary results, as shown in Figure 43, for loading glycylglycine-FITC

conjugate using the preswelling technique (*i.e.*, one of two common high Hb techniques

used to load within RBCs) are promising that dye may be loaded into RBCs while

maintaining their Hb at near-normal levels. However, as expected from the strong

absorbance of Hb as well as increased scattering at wavelengths in the visible region of

the spectrum, the fluorescence spectra of free and loaded glycylglycine-FITC conjugate

are significantly different (Figure 43a). The locations of the strong absorbance bands of

Hb are indicated on the fluorescence spectrum by the shaded blocks. The dips in the

FITC fluorescence correspond well with the absorption peaks of oxygenated Hb. Lysing

the cells *via* addition of water reduces the scattering of the samples and allows the

encapsulated glycylglycine-FITC conjugate to diffuse into the entire sample volume.

Upon lysis, the measured fluorescence increases greater than 8-fold. Conversely, the

signal increase due to dilution alone, verified by adding an equivalent volume of 165

mM NaCl rather than water, is less than 1.5-fold. This further verifies the destructive

effects of blood (*i.e.*, Hb absorbance and scattering) on the fluorescence of dyes that emit

in the visible wavelength range, confirming the need to move to the NIR.
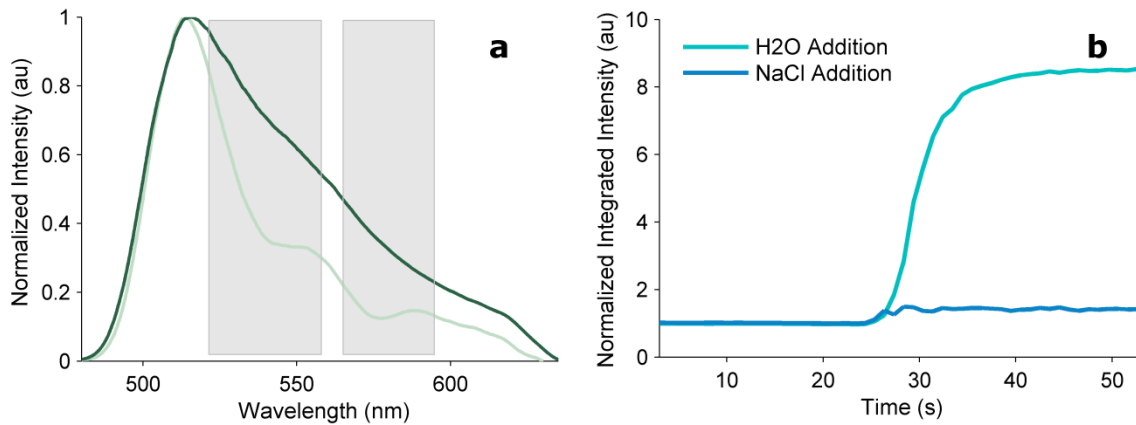
Figure 43. (a) Difference between the fluorescence spectra of a solution of free glycylglycine-FITC conjugate (dark green) and glycylglycine-FITC conjugate loaded within high Hb bovine ghosts (light green). Shaded areas represent the two absorption peaks of the oxygenated Hb spectrum. (b) Greater than 8x increase in signal upon lysing the loaded cells (light blue) with water, which releases the glycylglycine-FITC conjugate loaded within the cells. Less than 1.5x signal increase results from an equivalent dilution with 165 mM NaCl, which does not lyse the cells.

The animal specific and animal nonspecific calibration curves shown in Figure 37 and Figure 38, respectively, were used to determine the equivalent concentration of dye within the animal given the measured voltage increases for the loaded ghost injections of 200 µL and 830 µL. As summarized in Table 4, the measured voltage increases are equivalent to approximately 2.05 µM and 2.29 µM (200 µL injection leading to 0.9038 V increase) and 4.93 and 5.69 µM (830 µL injection leading to 2.8552 V increase) dye concentrations in the rat vasculature. If we consider the packed cell volume (*i.e.*, half of the total injected volume) to be dye at the concentration loaded within the ghosts (*i.e.*, 132.7 µM), the maximum achievable dye concentration in the blood due to the 200 µL and 800 µL injections would be 0.88 µM and 3.67 µM, respectively. These concentrations are lower than would be expected from the

90

calibration curves given the voltage increases achieved with loaded ghosts. Given that

only approximately 20 – 30% of the ghosts were successfully loaded with dye supports

the position that assuming 100% dye volume in the ghost sample is a far larger volume

than injected (*i.e.*, this assumption assumes perfect packing with no space between cells,

the membranes comprise no volume, and all cells loaded perfectly). Closer estimates of

the equivalent free dye concentration within the rat would be an order of magnitude

lower. This discrepancy in the measured signal indicates that the loaded ghosts were

different than free dye and that loading within the ghosts may result in an enhancement

of the signal.

Table 4. Effective concentrations of loaded ghosts within rat compared with maximum concentration achievable assuming free dye.

	Effective concentration using animal-specific calibration curve	*Effective concentration using animal-nonspecific calibration curve*	*Concentration assuming packed volume (½ total) to be 132.7 μM dye*
200 μL injection, 132.7 μM	2.05 μM	2.29 μM	0.88 μM
830 μL injection, 132.7 μM	4.93 μM	5.69 μM	3.67 μM

The fluorescence properties of *NIR dye II* were also sensitive to changes in both

temperature and concentration, which is highlighted in Figure 44. *NIR dye II* samples

ranging from 1 μM to 20 μM were prepared and temperatures lowered to approximately

4 °C. Spectral data was collected as the samples warmed to room temperature. As shown

by the representative low concentration (5 µM; Figure 44a and b) and high concentration (20 µM; Figure 44c and d) samples, fluorescence is minimized for all concentrations at low temperature. Quenching is more significant at higher concentrations, as the increase in total integrated fluorescence is 20.35% and 422.9% for the 5 µM and 20 µM samples, respectively. Furthermore, at low temperatures, the high concentration samples exhibit a slight blue shift of the 830 nm peak and introduction of a longer wavelength peak at 910 nm. As temperature increases, the longer wavelength peak decreases, supporting the hypothesis that these spectral effects result from low temperature aggregation of the dye molecules. This also supports the presence of the dye aggregate layer observed in some *NIR dye II*-loaded ghost samples. An image of the samples ranging from 20 µM (leftmost) to 1 µM (rightmost) are shown in Figure 45 at (a) approximately 4 °C and (b) room temperature. Lower concentration samples (*i.e.*, 1 or 2 µM) remain clear regardless of temperature. However, higher concentration samples (*i.e.*, 5 to 20 µM) are clear at approximately 4 °C and develop a blue tint, which is concentration dependent, with increased temperature. Thus, temperature effects are more significant for high concentration *NIR dye II* samples, pointing to dye aggregation as the culprit.
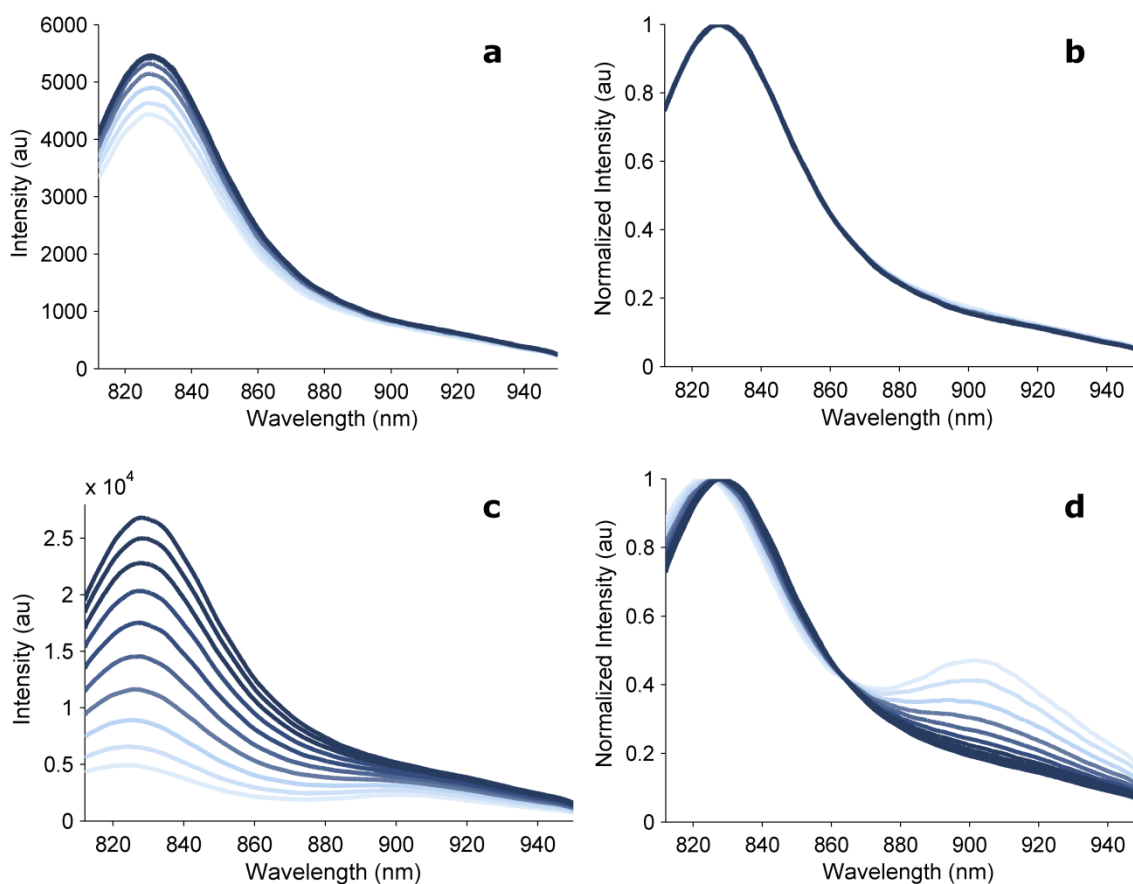
Figure 44. (a) Raw and (b) normalized fluorescence spectra of 5 μM *NIR dye II* as a function of temperature show a 20.35% increase in integrated signal with increased temperature from 4 °C to room temperature. (c) Raw and (d) normalized fluorescence spectra of 20 μM *NIR dye II* as a function of temperature show significant spectral changes and a 422.9% increase in integrated signal with increased temperature. Note: line colors darken with temperature.
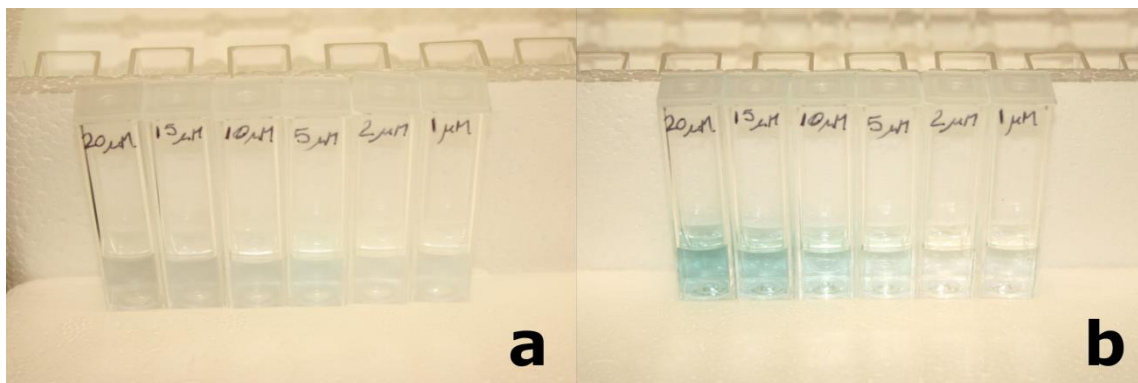
Figure 45. *NIR dye II* samples are displayed from high to low concentration (left to right) at (a) 4 °C and (b) room temperature. Blue color of the high concentration (*i.e.*, 5 µM and higher) samples develops as temperature increases.

4.4 Conclusions

The NIR region of the electromagnetic spectrum is ideal for *in vivo* applications, as this region provides the lowest levels of absorption (*i.e.*, due to Hb and water) and scattering. As such, penetration depth within tissue is higher compared with dyes that emit in the visible region of the spectrum. Although absorbing and emitting in the correct portion of the spectrum, the NIR dyes synthesized as a part of this work had a number of unintended difficulties. *NIR dye I* was very sensitive to both solvent polarity and presence of protein. Due to a strong tendency to aggregate, this dye was not applicable for loading within RBCs. *NIR dye II* was modified to discourage aggregation and proved to be much more stable in solution. However, the pH sensitivity of the dye over a physiologically-relevant range was too low for reliable use *in vivo*, precluding the ability to optically monitor pH within the animal. Nonetheless, the enhanced sensitivity of the optical system and increased collection of fluorescence due to the NIR wavelength

region allowed for relatively large increases in signal to be measured upon injection of both free and loaded *NIR dye II*. Both free and loaded dye reached maximum signal levels approximately 5 min post-injection, after which both signals decayed following the sum of a single exponential and constant. Encapsulation within the ghosts resulted in enhanced signal levels following injection compared with the expected signal increase due to free dye. Thus, although encapsulation did not result in significantly longer circulation times *in vivo*, the enhancement in signal observed for injected ghosts verified that these samples were, in fact, different than free dye. Employing autologous RBCs, rather than cross-species RBCs, will avoid issues related to host response and likely result in prolonged circulation time of dye-loaded cells *in vivo*.

5. CONCLUSIONS

5.1 ZnO Nano/microstructures as Environmental Sensors

In this work, ZnO nano- and microstructures across three size regimes (*i.e.*, 0-D, 1-D, and 2-D) were assessed for photobleaching rates under continuous and periodic excitation. The rate of photobleaching was shown to be a function of the surface area to volume ratio with higher ratios leading to increased photobleaching. This finding indicates that reactivity of the nano/microstructures relates to the surface states, which comprise a higher ratio of states for very small particles with high surface area to volume ratios. ZnO nanoparticles, which exhibited high sensitivity to changes in the environment, also exhibited high sensitivity to humidity – a promising result for future work towards a generalized ZnO nanoparticle sensor platform. The nanoparticles displayed a linear response with sensitivities of 0.65% change in signal per % RH (normalized sensitivity of 0.008417 RH^{-1}) and 0.75% change in signal per % RH (normalized sensitivity of 0.01898 RH^{-1}) in nitrogen and air, respectively.

In future work, ZnO nanoparticles may be applied to more clinically-relevant gases, such as CO or NO_2. NO_2 has been implicated as a contributor to air pollution, a recognized health problem. Proper monitoring of the gas with an inexpensive sensor such as one built on a ZnO platform is an important step in solving this global crisis and reducing the associated health problems.

5.2 RBC-Based Monitoring of Blood Analytes

We have shown that carrier RBCs, which have been traditionally applied towards drug delivery, can be loaded with analyte-sensitive intracellular dyes. Using simple optical techniques, these dyes then report on changes in extracellular analyte levels – the first demonstration of these carrier cells towards long-term blood analyte monitoring.

RBCs loaded with a glycylglycine-FITC conjugate using the dilution technique were shown to reversibly monitor extracellular pH changes. These ghosts have low Hb levels, which has important implications for the emission region of the dye. The emission of FITC between 500 and 600 nm overlaps with strong Hb absorption; furthermore, scattering is significant in this region of the spectrum. The drawback of this method, however, is that these cells will likely be rapidly removed from the circulation due to their low levels of Hb and other intracellular components. Preliminary results using a loading procedure that maintains near-normal levels of Hb suffered from significant decreases in FITC emission due to scattering and absorbance, as highlighted by the large spectral changes.

For the *in vivo* realization of this sensing platform, it is necessary to move into the NIR region, where absorbance and scattering of tissue are minimized. Two NIR emitting dyes were prepared and tested for their pH sensitivity. *NIR dye I* displayed significant aggregation effects in solution due to self-association of the molecules. Furthermore, its spectrum shifted based on polarity, and the fluorescence was much higher in ethanol than in water. The fluorescence also increased upon binding with proteins, likely due to disruption of the aggregates. Finally, pH sensitivity of protein-

bound dye was shown to be significantly less than that of free dye. *NIR dye II* had additional sulfonate groups to reduce aggregation. However, the dye was shown to be temperature sensitive, owing to aggregation at low temperatures.

NIR dye II as a free and loaded dye showed pH changes of approximately 15 – 30% and 13%, respectively. These changes were too small to reliably track the small pH changes manageable by adjustments using sodium bicarbonate and CO_2 *in vivo*. Nevertheless, the signal from dye-loaded ghosts was easily monitored with a fiber optic probe-based system. Although the circulation times of free and loaded dye were not statistically significantly different, the signal levels from loaded dye were higher than expected for free dye. The enhancement effect may be due to binding of the dye with protein, as seen with *NIR dye I*.

The circulation time of dye-loaded RBCs *in vivo* may be lengthened through a number of measures. First, it may be beneficial to load autologous or homologous RBCs rather than cross-species RBCs. The first step may be tracking of control horse RBCs following injection into a rat. Determining the circulation time of these cells may give insight into the maximum time that dye-loaded horse RBCs may be expected to survive in a rat. Given the significant differences between horse and rat RBCs, this circulation time may be lower than initially predicted. Second, the use of a gentler loading method (*e.g.*, dialysis or preswelling) that maintains near-normal levels of Hb and other cellular components may aid in maintaining near-normal lifespans of RBCs following injection. These methods rely on limiting the volume into which the RBCs are placed for the lysis procedure; the methods also require a smaller volume of analyte-sensitive dye to obtain

equivalent loaded concentrations. Alternatively, a different labeling mechanism, such as

one recently published that relies on modification of RBC progenitor cells, may be used

for preparation of RBCs for long-term monitoring [150]. The modification process did

not damage the membranes, and *in vivo* survival studies showed little difference in the

circulation times of control and modified RBCs in a mouse. The synthesis of a two-band

ratiometric, highly pH- or glucose-sensitive NIR dye is necessary for verifying the use of

this system for *in vivo* blood analyte monitoring. Although monitoring pH is clinically

relevant for many patients, long-term, minimally-invasive glucose monitoring is

paramount given the already high and still growing incidence of diabetes.

REFERENCES

1.   J. R. Lakowicz, *Principles of Fluorescence Spectroscopy* (Springer, New York, 2006).

2.   L. M. Kukreja and P. Misra, "Photoluminesce processes in ZnO thin films and quantum structures" in *ZnO Nanocrystals and Allied Materials,* M. S. R. Rao and T. Okada, eds. (Springer, Dordrecht, 2013).

3.   L. Y. Zhang, L. W. Yin, C. X. Wang, N. Lun, Y. X. Qi and D. Xiang, "Origin of visible photoluminescence of ZnO quantum dots: defect-dependent and size-dependent," Journal of Physical Chemistry C **114**(21), 9651-9658 (2010).

4.   S. Tongay, J. Suh, C. Ataca, W. Fan, A. Luce, J. S. Kang, J. Liu, C. Ko, R. Raghunathanan and J. Zhou, "Defects activated photoluminescence in two-dimensional semiconductors: interplay between bound, charged, and free excitons," Scientific Reports **3**, 2657 (2013).

5.   A. Hulanicki, S. Glab and F. Ingman, "Chemical sensors: definitions and classification," Pure and Applied Chemistry **63**(9), 1247-1250 (1991).

6.   A. P. Demchenko, *Introduction to Fluorescence Sensing* (Springer Netherlands, Dordrecht, 2009).

7.   G. Behera, P. Behera and B. K. Mishra, "Cyanine dyes: self aggregation and behaviour in surfactants a review," Journal of Surface Science and Technology **23**(1/2), 1-31 (2007).

8.   C. Reichardt, "Solvatochromic dyes as solvent polarity indicators," Chemical Reviews **94**(8), 2319-2358 (1994).

9.   U. Ozgur, Y. I. Alivov, C. Liu, A. Teke, M. A. Reshchikov, S. Dogan, V. Avrutin, S. J. Cho and H. Morkoc, "A comprehensive review of ZnO materials and devices," Journal of Applied Physics **98**(4), pp. 041301-1-041301-103 (2005).

10.   A. B. Djurišić and Y. H. Leung, "Optical properties of ZnO nanostructures," Small **2**(8-9), 944-961 (2006).

11.   P. Rai, W. K. Kwak and Y. T. Yu, "Solvothermal synthesis of ZnO nanostructures and their morphology-dependent gas-sensing properties," ACS Applied Materials & Interfaces **5**(8), 3026-3032 (2013).

12. X. Wang, C. Yu, J. Wu and Y. Zhang, "Template-free hydrothermal synthesis of ZnO microrods for gas sensor application," Ionics **19**(2), 355-360 (2013).

13. B. Shouli, C. Liangyuan, L. Dianqing, Y. Wensheng, Y. Pengcheng, L. Zhiyong, C. Aifan and C. C. Liu, "Different morphologies of ZnO nanorods and their sensing property," Sensors and Actuators B: Chemical **146**(1), 129-137 (2010).

14. C. J. Chang, S. T. Hung, C. K. Lin, C. Y. Chen and E. H. Kuo, "Selective growth of ZnO nanorods for gas sensors using ink-jet printing and hydrothermal processes," Thin Solid Films **519**(5), 1693-1698 (2010).

15. P. S. Cho, K. W. Kim and J. H. Lee, "NO2 sensing characteristics of ZnO nanorods prepared by hydrothermal method," Journal of Electroceramics **17**(2-4), 975-978 (2006).

16. E. Oh, H. Y. Choi, S. H. Jung, S. Cho, J. C. Kim, K. H. Lee, S. W. Kang, J. Kim, J. Y. Yun and S. H. Jeong, "High-performance NO2 gas sensor based on ZnO nanorod grown by ultrasonic irradiation," Sensors and Actuators B: Chemical **141**(1), 239-243 (2009).

17. M. W. Ahn, K. S. Park, J. H. Heo, J. G. Park, D. W. Kim, K. J. Choi, J. H. Lee and S. H. Hong, "Gas sensing properties of defect-controlled ZnO-nanowire gas sensor," Applied Physics Letters **93**(26), pp. 263103-1-263103-3 (2008).

18. L. J. Bie, X. N. Yan, J. Yin, Y. Q. Duan and Z. H. Yuan, "Nanopillar ZnO gas sensor for hydrogen and ethanol," Sensors and Actuators B: Chemical **126**(2), 604-608 (2007).

19. T. J. Hsueh, C. L. Hsu, S. J. Chang and I. C. Chen, "Laterally grown ZnO nanowire ethanol gas sensors," Sensors and Actuators B: Chemical **126**(2), 473-477 (2007).

20. Q. Wan, Q. H. Li, Y. J. Chen, T. H. Wang, X. L. He, J. P. Li and C. L. Lin, "Fabrication and ethanol sensing characteristics of ZnO nanowire gas sensors," Applied Physics Letters **84**(18), 3654-3656 (2004).

21. X. F. Chu, D. L. Jiang, A. B. Djurisic and H. L. Yu, "Gas-sensing properties of thick film based on ZnO nano-tetrapods," Chemical Physics Letters **401**(4-6), 426-429 (2005).

22. G. Sberveglieri, C. Baratto, E. Comini, G. Faglia, A. Ferroni, A. Ponzoni and A. Vomiero, "Synthesis and characterization of semiconducting nanowires for gas sensing," Sensors and Actuators B: Chemical **121**(1), 208-213 (2007).

23. B. S. Kang, Y. W. Heo, L. C. Tien, D. P. Norton, F. Ren, B. P. Gila and S. J. Pearton, "Hydrogen and ozone gas sensing using multiple ZnO nanorods," Applied Physics A: Materials Science & Processing **80**(5), 1029-1032 (2005).

24. T. Y. Wei, P. H. Yeh, S. Y. Lu and Z. Lin-Wang, "Gigantic enhancement in sensitivity using Schottky contacted nanowire nanosensor," Journal of the American Chemical Society **131**(48), 17690-17695 (2009).

25. J. X. Wang, X. W. Sun, Y. Yang, H. Huang, Y. C. Lee, O. K. Tan and L. Vayssieres, "Hydrothermally grown oriented ZnO nanorod arrays for gas sensing applications," Nanotechnology **17**(19), 4995-4998 (2006).

26. Y. S. Zhang, K. Yu, D. S. Jiang, Z. Q. Zhu, H. R. Geng and L. Q. Luo, "Zinc oxide nanorod and nanowire for humidity sensor," Applied Surface Science **242**(1-2), 212-217 (2005).

27. A. van Dijken, E. A. Meulenkamp, D. Vanmaekelbergh and A. Meijerink, "The kinetics of the radiative and nonradiative processes in nanocrystalline ZnO particles upon photoexcitation," Journal of Physical Chemistry B **104**(8), 1715-1723 (2000).

28. A. van Dijken, E. A. Meulenkamp, D. Vanmaekelbergh and A. Meijerink, "Influence of adsorbed oxygen on the emission properties of nanocrystalline ZnO particles," Journal of Physical Chemistry B **104**(18), 4355-4360 (2000).

29. K. Vanheusden, W. L. Warren, C. H. Seager, D. R. Tallant, J. A. Voigt and B. E. Gnade, "Mechanisms behind green photoluminescence in ZnO phosphor powders," Journal of Applied Physics **79**(10), 7983-7990 (1996).

30. D. S. Bohle and C. J. Spina, "The relationship of oxygen binding and peroxide sites and the fluorescent properties of zinc oxide semiconductor nanocrystals," Journal of the American Chemical Society **129**(41), 12380-12381 (2007).

31. D. Valerini, A. Creti, A. P. Caricato, M. Lomascolo, R. Rella and M. Martino, "Optical gas sensing through nanostructured ZnO films with different morphologies," Sensors and Actuators B: Chemical **145**(1), 167-173 (2010).

32. D. Padilla-Rueda, J. M. Vadillo and J. J. Laserna, "Room temperature pulsed laser deposited ZnO thin films as photoluminescence gas sensors," Applied Surface Science **259**, 806-810 (2012).

33. S. Lettieri, A. Bismuto, P. Maddalena, C. Baratto, E. Comini, G. Faglia, G. Sberveglieri and L. Zanotti, "Gas sensitive light emission properties of tin oxide and zinc oxide nanobelts," Journal of Non-Crystalline Solids **352**(9-20), 1457-1460 (2006).

34.   E. Comini, C. Baratto, G. Faglia, M. Ferroni and G. Sberveglieri, "Single crystal ZnO nanowires as optical and conductometric chemical sensor," Journal of Physics D: Applied Physics **40**(23), 7255-7259 (2007).

35.   A. Creti, D. Valerini, A. Taurino, F. Quaranta, M. Lomascolo and R. Rella, "Photoluminescence quenching processes by NO2 adsorption in ZnO nanostructured films," Journal of Applied Physics **111**(7), pp. 073520-1-073520-9 (2012).

36.   A. Bismuto, S. Lettieri, P. Maddalena, C. Baratto, E. Comini, G. Faglia, G. Sberveglieri and L. Zanotti, "Room-temperature gas sensing based on visible photoluminescence properties of metal oxide nanobelts," Journal of Optics A: Pure and Applied Optics **8**(7), pp. S585-S588 (2006).

37.   C. Baratto, S. Todros, G. Faglia, E. Comini, G. Sberveglieri, S. Lettieri, L. Santamaria and P. Maddalena, "Luminescence response of ZnO nanowires to gas adsorption," Sensors and Actuators B: Chemical **140**(2), 461-466 (2009).

38.   M. Konstantaki, A. Klini, D. Anglos and S. Pissadakis, "An ethanol vapor detection probe based on a ZnO nanorod coated optical fiber long period grating," Optics Express **20**(8), 8472-8484 (2012).

39.   R. Aneesh and S. K. Khijwania, "Zinc oxide nanoparticle based optical fiber humidity sensor having linear response throughout a large dynamic range," Applied Optics **50**(27), 5310-5314 (2011).

40.   Y. Liu, Y. Zhang, H. Lei, J. Song, H. Chen and B. Li, "Growth of well-arrayed ZnO nanorods on thinned silica fiber and application for humidity sensing," Optics Express **20**(17), 19404-19411 (2012).

41.   World Health Organization, "Ambient (outdoor) air quality and health" in *Fact Sheet No 313* (World Health Organization, 2014).

42.   G. F. Fine, L. M. Cavanagh, A. Afonja and R. Binions, "Metal oxide semi-conductor gas sensors in environmental monitoring," Sensors **10**(6), 5469-5502 (2010).

43.   D. G. Fullerton, N. Bruce and S. B. Gordon, "Indoor air pollution from biomass fuel smoke is a major health concern in the developing world," Transactions of The Royal Society of Tropical Medicine and Hygiene **102**(9), 843-851 (2008).

44.   M. Haase, H. Weller and A. Henglein, "Photochemistry and radiation chemistry of colloidal semiconductors. 23. Electron storage on zinc oxide particles and size quantization," The Journal of Physical Chemistry **92**(2), 482-487 (1988).

45.   R. Majithia, S. Ritter and K. E. Meissner, "Heterogeneous nucleation for synthesis of sub-20 nm ZnO nanopods and their application to optical humidity sensing," Analytica Chimica Acta **812**, 206-214 (2014).

46.   R. Majithia, J. Speich and K. Meissner, "Mechanism of generation of ZnO microstructures by microwave-assisted hydrothermal approach," Materials **6**(6), 2497-2507 (2013).

47.   M. Ghosh, R. S. Ningthoujam, R. K. Vatsa, D. Das, V. Nataraju, S. C. Gadkari, S. K. Gupta and D. Bahadur, "Role of ambient air on photoluminescence and electrical conductivity of assembly of ZnO nanoparticles," Journal of Applied Physics **110**(5), pp. 054309-1-054309-7 (2011).

48.   J. Eriksson, V. Khranovskyy, F. Söderlind, P.-O. Käll, R. Yakimova and A. L. Spetz, "ZnO nanoparticles or ZnO films: a comparison of the gas sensing capabilities," Sensors and Actuators B: Chemical **137**(1), 94-102 (2009).

49.   R. J. McNichols and G. L. Coté, "Optical glucose sensing in biological fluids: an overview," Journal of Biomedical Optics **5**(1), 5-16 (2000).

50.   E. P. Trulock III, "Arterial blood gases" in *Clinical Methods: The History, Physical, and Laboratory Examinations,* H. K. Walker, W. D. Hall and J. W. Hurst, eds. (Butterworths, Boston, 1990), Chap. 49.

51.   M. S. D. Agus, J. L. Alexander and P. A. Mantell, "Continuous non-invasive end-tidal CO2 monitoring in pediatric inpatients with diabetic ketoacidosis," Pediatric Diabetes **7**(4), 196-200 (2006).

52.   R. B. Easley, T. R. Johnson and J. D. Tobias, "Continuous pH monitoring using the Paratrend® 7 inserted into a peripheral vein in a patient with shock and congenital lactic acidosis," Clinical Pediatrics **41**(5), 351-355 (2002).

53.   M. W. Savage, K. K. Dhatariya, A. Kilvert, G. Rayman, J. A. E. Rees, C. H. Courtney, L. Hilton, P. H. Dyer and M. S. Hamersley, "Joint British Diabetes Societies guideline for the management of diabetic ketoacidosis," Diabetic Medicine **28**(5), 508-515 (2011).

54.   G. E. Umpierrez, M. B. Murphy and A. E. Kitabchi, "Diabetic ketoacidosis and hyperglycemic hyperosmolar syndrome," Diabetes Spectrum **15**(1), 28-36 (2002).

55.   J. D. Tobias, "Transcutaneous carbon dioxide monitoring in infants and children," Pediatric Anesthesia **19**(5), 434-444 (2009).

56.	M. E. McBride, J. W. Berkenbosch and J. D. Tobias, "Transcutaneous carbon dioxide monitoring during diabetic ketoacidosis in children and adolescents," Pediatric Anesthesia **14**(2), 167-171 (2004).

57.	E. Garcia, T. Abramo, P. Okada, D. Guzman, J. Reisch and R. Wiebe, "Capnometry for noninvasive continuous monitoring of metabolic status in pediatric diabetic ketoacidosis," Critical Care Medicine **31**(10), 2539-2543 (2003).

58.	S. L. Murphy, J. Xu and K. D. Kochanek, "Deaths: final data for 2010," National Vital Statistics Reports **61**(4), 1-118 (2013).

59.	J. P. Leu and J. Zonszein, "Diagnostic criteria and classification of diabetes" in *Principles of Diabetes Mellitus,* L. Poretsky, ed. (Springer, New York, 2010), Chap. 7.

60.	International Diabetes Federation, *IDF Diabetes Atlas, 6th edn.* (International Diabetes Federation, Brussels, Belgium, 2013).

61.	S. Chamany and B. P. Tabaei, "Epidemiology" in *Principles of Diabetes Mellitus,* L. Poretsky, ed. (Springer, New York, 2010), Chap. 8.

62.	Y. Ohkubo, H. Kishikawa, E. Araki, T. Miyata, S. Isami, S. Motoyoshi, Y. Kojima, N. Furuyoshi and M. Shichiri, "Intensive insulin therapy prevents the progression of diabetic microvascular complications in Japanese patients with non-insulin-dependent diabetes mellitus: a randomized prospective 6-year study," Diabetes Research and Clinical Practice **28**(2), 103-117 (1995).

63.	The Diabetes Control and Complications Trial Research Group, "The effect of intensive treatment of diabetes on the development and progression of long-term complications in insulin-dependent diabetes mellitus," New England Journal of Medicine **329**(14), 977-986 (1993).

64.	UK Prospective Diabetes Study (UKPDS) Group, "Intensive blood-glucose control with sulphonylureas or insulin compared with conventional treatment and risk of complications in patients with type 2 diabetes (UKPDS 33)," The Lancet **352**(9131), 837-853 (1998).

65.	L. C. Clark and C. Lyons, "Electrode systems for continuous monitoring in cardiovascular surgery," Annals of the New York Academy of Sciences **102**(1), 29-45 (1962).

66.	J. Wang, "Electrochemical glucose biosensors," Chemical Reviews **108**(2), 814-825 (2008).

67.   G. Wang, X. He, L. Wang, A. Gu, Y. Huang, B. Fang, B. Geng and X. Zhang, "Non-enzymatic electrochemical sensing of glucose," Microchimica Acta **180**(3-4), 161-186 (2013).

68.   S. Park, H. Boo and T. D. Chung, "Electrochemical non-enzymatic glucose sensors," Analytica Chimica Acta **556**(1), 46-57 (2006).

69.   C. Chen, Q. Xie, D. Yang, H. Xiao, Y. Fu, Y. Tan and S. Yao, "Recent advances in electrochemical glucose biosensors: a review," RSC Advances **3**(14), 4473-4491 (2013).

70.   M. M. Rahman, A. Ahammad, J. H. Jin, S. J. Ahn and J. J. Lee, "A comprehensive review of glucose biosensors based on nanostructured metal-oxides," Sensors **10**(5), 4855-4886 (2010).

71.   J. M. Harris, C. Reyes and G. P. Lopez, "Common causes of glucose oxidase instability in in vivo biosensing: a brief review," Journal of Diabetes Science and Technology **7**(4), 1030-1038 (2013).

72.   J. Wagner, C. Malchoff and G. Abbott, "Invasiveness as a barrier to self-monitoring of blood glucose in diabetes," Diabetes Technology & Therapeutics **7**(4), 612-619 (2005).

73.   G. Y. Gandhi, M. Kovalaske, Y. Kudva, K. Walsh, M. B. Elamin, M. Beers, C. Coyle, M. Goalen, M. S. Murad and P. J. Erwin, "Efficacy of continuous glucose monitoring in improving glycemic control and reducing hypoglycemia: a systematic review and meta-analysis of randomized trials," Journal of Diabetes Science and Technology **5**(4), 952-965 (2011).

74.   N. Poolsup, N. Suksomboon and A. Kyaw, "Systematic review and meta-analysis of the effectiveness of continuous glucose monitoring (CGM) on glucose control in diabetes," Diabetology and Metabolic Syndrome **5**(1), 1-14 (2013).

75.   E. S. Huang, M. O'Grady, A. Basu, A. Winn, P. John, J. Lee, D. Meltzer, C. Kollman, L. Laffel, W. Tamborlane, S. Weinzimer and T. Wysocki, "The cost-effectiveness of continuous glucose monitoring in type 1 diabetes," Diabetes Care **33**(6), 1269-1274 (2010).

76.   R. Gifford, "Continuous glucose monitoring: 40 Years, what we′ve learned and what′s next," ChemPhysChem **14**(10), 2032-2044 (2013).

77.   Y. Onuki, U. Bhardwaj, F. Papadimitrakopoulos and D. J. Burgess, "A review of the biocompatibility of implantable devices: current challenges to overcome foreign body response," Journal of Diabetes Science and Technology **2**(6), 1003-1015 (2008).

78.   A. Koh, S. P. Nichols and M. H. Schoenfisch, "Glucose sensor membranes for mitigating the foreign body response," Journal of Diabetes Science and Technology **5**(5), 1052-1059 (2011).

79.   C. Yoshikawa, S. Hattori, T. Honda, C. F. Huang and H. Kobayashi, "Non-biofouling property of well-defined concentrated poly(2-hydroxyethyl methacrylate) brush," Materials Letters **83**, 140-143 (2012).

80.   R. Gifford, M. M. Batchelor, Y. Lee, G. Gokulrangan, M. E. Meyerhoff and G. S. Wilson, "Mediation of in vivo glucose sensor inflammatory response via nitric oxide release," Journal of Biomedical Materials Research Part A **75A**(4), 755-766 (2005).

81.   Dexcom, "Dexcom G4 Platinum User's Guide" (2012).

82.   Medtronic, "Getting started with continuous glucose monitoring: Paradigm REAL-Time Revel Minimed" (2014).

83.   Medtronic, "Getting started with Guardian REAL-Time continuous glucose monitoring" (2014).

84.   G. S. Wilson and Y. Zhang, "Introduction to the glucose sensing problem" in *In Vivo Glucose Sensing,* D. D. Cunningham and J. A. Stenken, eds. (John Wiley & Sons, Inc., Hoboken, 2009), Chap. 1.

85.   K. Aslan, J. R. Lakowicz and C. D. Geddes, "Tunable plasmonic glucose sensing based on the dissociation of Con A-aggregated dextran-coated gold colloids," Analytica Chimica Acta **517**(1-2), 139-144 (2004).

86.   V. L. Alexeev, S. Das, D. N. Finegold and S. A. Asher, "Photonic crystal glucose-sensing material for noninvasive monitoring of glucose in tear fluid," Clinical Chemistry **50**(12), 2353-2360 (2004).

87.   B. H. Malik, C. W. Pirnstill and G. L. Cote, "Dual-wavelength polarimetric glucose sensing in the presence of birefringence and motion artifact using anterior chamber of the eye phantoms," Journal of Biomedical Optics **18**(1), pp. 017007-1-017007-9 (2013).

88.   A. M. K. Enejder, T. G. Scecina, J. Oh, M. Hunter, S. Sasic, G. L. Horowitz, M. S. Feld and W. C. Shih, "Raman spectroscopy for noninvasive glucose measurements," Journal of Biomedical Optics **10**(3), pp. 031114-0311149 (2005).

89. M. R. Robinson, R. P. Eaton, D. M. Haaland, G. W. Koepp, E. V. Thomas, B. R. Stallard and P. L. Robinson, "Noninvasive glucose monitoring in diabetic patients: a preliminary evaluation," Clinical Chemistry **38**(9), 1618-1622 (1992).

90. Puget Sound Blood Center, "Donating Platelets", http://www.psbc.org/programs/platelets.htm (2014).

91. M. R. Clark, "Senescence of red blood cells: progress and problems," Physiological Reviews **68**(2), 503-554 (1988).

92. J. V. Frangioni, "In vivo near-infrared fluorescence imaging," Current Opinion in Chemical Biology **7**(5), 626-634 (2003).

93. M. Hamidi and H. Tajerzadeh, "Carrier erythrocytes: an overview," Drug Delivery **10**(1), 9-20 (2003).

94. N. V. B. Marsden and S. G. Ostling, "Accumulation of dextran in human red cells after haemolysis," Nature **184**(Suppl 10), 723-724 (1959).

95. U. Zimmerman, "Jahresbericht der kernforschungsanlage Julich GmbH," Nuclear Research Center, Julich, 55-58 (1973).

96. G. M. Ihler, R. H. Glew and F. W. Schnure, "Enzyme loading of erythrocytes," Proceedings of the National Academy of Sciences of the United States of America **70**(9), 2663-2666 (1973).

97. M. Hamidi, A. Zarrin, M. Foroozesh and S. Mohammadi-Samani, "Applications of carrier erythrocytes in delivery of biopharmaceuticals," Journal of Controlled Release **118**(2), 145-160 (2007).

98. C. Gutiérrez Millán, M. L. Sayalero Marinero, A. Zarzuelo Castañeda and J. M. Lanao, "Drug, enzyme and peptide delivery using erythrocytes as carriers," Journal of Controlled Release **95**(1), 27-49 (2004).

99. L. Rossi, S. Serafini, F. Pierigé, A. Antonelli, A. Cerasi, A. Fraternale, L. Chiarantini and M. Magnani, "Erythrocyte-based drug delivery," Expert Opinion on Drug Delivery **2**(2), 311-322 (2005).

100. A. Gothoskar, "Resealed erythrocytes: a review," Pharmaceutical Technology **28**(3), 140-155 (2004).

101. G. M. Ihler, "Erythrocyte carriers," Pharmacology & Therapeutics **20**(2), 151-169 (1983).

102. R. Hirlekar, P. Patel, N. Dand and V. Kadam, "Drug loaded erythrocytes: as novel drug delivery system," Current Pharmaceutical Design **14**(1), 63-70 (2008).

103. C. G. Millan, M. L. S. Marinero, A. Z. Castaneda and J. M. Lanao, "Drug, enzyme and peptide delivery using erythrocytes as carriers," Journal of Controlled Release **95**(1), 27-49 (2004).

104. Y. M. Kwon, H. S. Chung, C. Moon, J. Yockman, Y. J. Park, S. D. Gitlin, A. E. David and V. C. Yang, "L-Asparaginase encapsulated intact erythrocytes for treatment of acute lymphoblastic leukemia (ALL)," Journal of Controlled Release **139**(3), 182-189 (2009).

105. H. He, J. Ye, Y. Wang, Q. Liu, H. S. Chung, Y. M. Kwon, M. C. Shin, K. Lee and V. C. Yang, "Cell-penetrating peptides meditated encapsulation of protein therapeutics into intact red blood cells and its application," Journal of Controlled Release **176**, 123-132 (2014).

106. R. Flower, E. Peiretti, M. Magnani, L. Rossi, S. Serafini, Z. Gryczynski and I. Gryczynski, "Observation of erythrocyte dynamics in the retinal capillaries and choriocapillaris using ICG-loaded erythrocyte ghost cells," Investigative Ophthalmology & Visual Science **49**(12), 5510-5516 (2008).

107. M. H. Steinberg, J. Edward J. Benz, A. H. Adewoye and B. L. Ebert, "Pathobiology of the human erythrocyte and its hemoglobins" in *Hematology: Basic Principles and Practice*, R. Hoffman, E. J. Benz Jr., L. E. Silberstein, H. Heslop, J. Weitz and J. Anastasi, eds. (Churchill Livingstone, Chatsworth, NSW, AUS, 2013), Chap. 31.

108. G. Lim H. W, M. Wortis and R. Mukhopadhyay, "Red blood cell shapes and shape transformations: Newtonian mechanics of a composite membrane: Sections 2.1–2.4" in *Soft Matter*, G. Gompper and M. Schick, eds. (Wiley-VCH Verlag GmbH & Co. KGaA, Weinheim, Germany, 2009).

109. C. C. W. Hsia, "Respiratory function of hemoglobin," New England Journal of Medicine **338**(4), 239-248 (1998).

110. P. M. Rodi, V. M. Trucco and A. M. Gennaro, "Factors determining detergent resistance of erythrocyte membranes," Biophysical Chemistry **135**(1–3), 14-18 (2008).

111. N. Mohandas and P. G. Gallagher, "Red cell membrane: past, present, and future," Blood **112**(10), 3939-3948 (2008).

112. K. Yazdanbakhsh, C. Lomas-Francis and M. E. Reid, "Blood groups and diseases associated with inherited abnormalities of the red blood cell membrane," Transfusion Medicine Reviews **14**(4), 364-374 (2000).

113. G. M. Ihler and H. C. W. Tsang, "Hypotonic hemolysis methods for entrapment of agents in resealed erythrocytes," Methods in Enzymology **149**, 221-229 (1987).

114. J. R. DeLoach, "Carrier erythrocytes," Medicinal Research Reviews **6**(4), 487-504 (1986).

115. G. Schwoch and H. Passow, "Preparation and properties of human erythrocyte ghosts," Molecular and Cellular Biochemistry **2**(2), 197-218 (1973).

116. P. Seeman, "Transient holes in the erythrocyte membrane during hypotonic hemolysis and stable holes in the membrane after lysis by saponin and lysolecithin," The Journal of Cell Biology **32**(1), 55-70 (1967).

117. F. Pierigè, S. Serafini, L. Rossi and M. Magnani, "Cell-based drug delivery," Advanced Drug Delivery Reviews **60**(2), 286-295 (2008).

118. M. Magnani, L. Rossi, A. Fraternale, M. Bianchi, A. Antonelli, R. Crinelli and L. Chiarantini, "Erythrocyte-mediated delivery of drugs, peptides, and modified oligonucleotides," Gene Therapy **9**(11), 749-751 (2002).

119. R. A. Schlegel, K. Lumley-Sapanski and P. Williamson, "Single cell analysis of factors increasing the survival of resealed erythrocytes in the circulation of mice" in *The Use of Resealed Erythrocytes as Carriers and Bioreactors*, M. Magnani and J. R. DeLoach, eds. (Plenum Press, New York, 1992).

120. B. E. Bax, M. D. Bain, P. J. Talbot, E. J. Parker-Williams and R. A. Chalmers, "Survival of human carrier erythrocytes in vivo," Clinical Science **96**(2), 171-178 (1999).

121. R. Azoui, J. L. Cuche, J. F. Renaud, M. Safar and G. Dagher, "A dopamine transporter in human erythrocytes: modulation by insulin," Experimental Physiology **81**(3), 421-434 (1996).

122. O. Fröhlich and R. B. Gunn, "Erythrocyte anion transport: the kinetics of a single-site obligatory exchange system," Biochimica et Biophysica Acta - Reviews on Biomembranes **864**(2), 169-194 (1986).

123. P. K. Khera, C. H. Joiner, A. Carruthers, C. J. Lindsell, E. P. Smith, R. S. Franco, Y. R. Holmes and R. M. Cohen, "Evidence for interindividual heterogeneity in the glucose gradient across the human red blood cell membrane and its relationship to hemoglobin glycation," Diabetes **57**(9), 2445-2452 (2008).

124. A. Carruthers, "Facilitated diffusion of glucose," Physiological Reviews **70**(4), 1135-1176 (1990).

125. P. G. LeFevre, "Evidence of active transfer of certain non-electrolytes across the human red cell membrane," The Journal of General Physiology **31**(6), 505-527 (1948).

126. A. Montel-Hagen, L. Blanc, M. Boyer-Clavel, C. Jacquet, M. Vidal, M. Sitbon and N. Taylor, "The Glut1 and Glut4 glucose transporters are differentially expressed during perinatal and postnatal erythropoiesis," Blood **112**(12), 4729-4738 (2008).

127. A. Klip and A. Marette, "Regulation of glucose transporters by insulin and exercise: cellular effects and implications for diabetes," Comprehensive Physiology, 451–494 (2011).

128. T. Bistritzer, L. Roeder, L. Hanukoglu and P. Levin, "Non-insulin dependent diabetic patients have increased glucose uptake in red blood cells," Hormone and Metabolic Research **23**(2), 70-73 (1991).

129. X. Hu, F. Peng, H. Zhou, Z. Zhang, W. Cheng and H. Feng, "The abnormality of glucose transporter in the erythrocyte membrane of Chinese type 2 diabetic patients," Biochimica et Biophysica Acta - Biomembranes **1466**(1), 306-314 (2000).

130. M. Porter-Turner, J. Skidmore, M. Khokher, B. Singh and C. Rea, "Relationship between erythrocyte GLUT1 function and membrane glycation in type 2 diabetes," British Journal of Biomedical Science **68**(4), 203-207 (2010).

131. M. Somogyi, "Distribution of blood sugar between corpuscles and plasma in diabetic and in alimentary hyperglycemia," Archives of Internal Medicine **42**(6), 931-938 (1928).

132. P. K. Gasbjerg, P. A. Knauf and J. Brahm, "Kinetics of bicarbonate transport in human red blood cell membranes at body temperature," The Journal of General Physiology **108**(6), 565-575 (1996).

133. H. Bodemann and H. Passow, "Factors controlling the resealing of the membrane of human erythrocyte ghosts after hypotonic hemolysis," The Journal of Membrane Biology **8**(1), 1-26 (1972).

134. M. Monici, "Cell and tissue autofluorescence research and diagnostic applications" in *Biotechnology Annual Review,* M.R. El-Gewely, ed. (Elsevier, 2005).

135. P. So, K. Kim, L. Hsu, P. Kaplan, T. Hacewicz, C. Dong, U. Greuter, N. Schlumpf and C. Buehler, "Two-photon microscopy of tissues" in *Handbook of Biomedical Fluorescence*, M. A. Mycek and B. W. Pogue, eds. (Marcel Dekker, Inc, New York, 2003).

136. R. R. Anderson and J. A. Parrish, "The optics of human skin," The Journal of Investigative Dermatology **77**(1), 13-19 (1981).

137. G. Strangman, D. A. Boas and J. P. Sutton, "Non-invasive neuroimaging using near-infrared light," Biological Psychiatry **52**(7), 679-693 (2002).

138. L. V. Wang and H. I. Wu, *Biomedical Optics: Principles and Imaging* (John Wiley & Sons, Inc., Hoboken, 2009).

139. A. N. Bashkatov, E. A. Genina, V. I. Kochubey and V. V. Tuchin, "Optical properties of human skin, subcutaneous and mucous tissues in the wavelength range from 400 to 2000 nm," Journal of Physics D: Applied Physics **38**(15), 2543-2555 (2005).

140. H. Tajerzadeh and M. Hamidi, "Evaluation of hypotonic preswelling method for encapsulation of enalaprilat in intact human erythrocytes," Drug Development and Industrial Pharmacy **26**(12), 1247-1257 (2000).

141. E. Pitt, C. M. Johnson, D. A. Lewis, D. A. Jenner and R. E. Offord, "Encapsulation of drugs in intact erythrocytes: an intravenous delivery system," Biochemical Pharmacology **32**(22), 3359-3368 (1983).

142. B. A. Armitage, "Cyanine dye–DNA interactions: intercalation, groove binding, and aggregation" in *DNA Binders and Related Subjects*, M. J. Waring and J. B. Chaires, eds. (Springer Berlin Heidelberg, 2005), Chap. 3.

143. S. M. Yarmoluk, D. V. Kryvorotenko, A. O. Balanda, M. Y. Losytskyy and V. B. Kovalska, "Proteins and cyanine dyes. Part III. Synthesis and spectroscopic studies of benzothiazolo-4-[1,2,6-trimethylpyridinium] monomethine cyanine dyes for fluorescent detection of bovine serum albumin in solutions," Dyes and Pigments **51**(1), 41-49 (2001).

144. A. Mishra, R. K. Behera, P. K. Behera, B. K. Mishra and G. B. Behera, "Cyanines during the 1990s: a review," Chemical Reviews **100**(6), 1973-2012 (2000).

145. T. Ogul'chansky, S. Yarmoluk, V. Yashchuk and M. Lossytskyi, "The spectral response on DNA interaction with some monomethyne cyanine dyes" in *Spectroscopy of Biological Molecules: New Directions*, J. Greve, G. J. Puppels C. Otto, eds. (Springer Netherlands, 1999), Chap. 138.

146. M. Y. Berezin, H. Lee, W. Akers and S. Achilefu, "Near infrared dyes as lifetime solvatochromic probes for micropolarity measurements of biological systems," Biophysical Journal **93**(8), 2892-2899 (2007).

147. A. Edelstein, N. Amodaj, K. Hoover, R. Vale and N. Stuurman, "Computer control of microscopes using µManager," Current Protocols in Molecular Biology, pp. 14.20.1-14.20.17 (2010).

148. O. K. Baskurt, R. A. Farley and H. J. Meiselman, "Erythrocyte aggregation tendency and cellular properties in horse, human, and rat: a comparative study," American Journal of Physiology: Heart and Circulatory Physiology **273**(6), pp. H2604-H2612 (1997).

149. S. Lawrence, J. Charlesworth, B. Pussell, L. V. Campbell and M. Kotowicz, "Factors influencing reticulophagocytic function in insulin-treated diabetes," Diabetes **33**(9), 813-818 (1984).

150. J. Shi, L. Kundrat, N. Pishesha, A. Bilate, C. Theile, T. Maruyama, S. K. Dougan, H. L. Ploegh and H. F. Lodish, "Engineered red blood cells as carriers for systemic delivery of a wide array of functional probes," Proceedings of the National Academy of Sciences **111**(28), 10131-10136 (2014).